International Journal of Physical Sciences

Volume 8 Number 21 9 June, 2013
ISSN 1992-1950

Academic Journals

ABOUT IJPS

The **International Journal of Physical Sciences (IJPS)** is published weekly (one volume per year) by Academic Journals.

International Journal of Physical Sciences (IJPS) is an open access journal that publishes high-quality solicited and unsolicited articles, in English, in all Physics and chemistry including artificial intelligence, neural processing, nuclear and particle physics, geophysics, physics in medicine and biology, plasma physics, semiconductor science and technology, wireless and optical communications, materials science, energy and fuels, environmental science and technology, combinatorial chemistry, natural products, molecular therapeutics, geochemistry, cement and concrete research, metallurgy, crystallography and computer-aided materials design. All articles published in IJPS are peer-reviewed.

Submission of Manuscript

Submit manuscripts as e-mail attachment to the Editorial Office at: ijps@academicjournals.org. A manuscript number will be mailed to the corresponding author shortly after submission.

For all other correspondence that cannot be sent by e-mail, please contact the editorial office (at ijps@academicjournals.org).

The International Journal of Physical Sciences will only accept manuscripts submitted as e-mail attachments.

Please read the **Instructions for Authors** before submitting your manuscript. The manuscript files should be given the last name of the first author.

Editors

Editorial Board

Instructions for Author

Electronic submission of manuscripts is strongly encouraged, provided that the text, tables, and figures are included in a single Microsoft Word file (preferably in Arial font).

The **cover letter** should include the corresponding author's full address and telephone/fax numbers and should be in an e-mail message sent to the Editor, with the file, whose name should begin with the first author's surname, as an attachment.

Article Types

Three types of manuscripts may be submitted:

Regular articles: These should describe new and carefully confirmed findings, and experimental procedures should be given in sufficient detail for others to verify the work. The length of a full paper should be the minimum required to describe and interpret the work clearly.

Short Communications: A Short Communication is suitable for recording the results of complete small investigations or giving details of new models or hypotheses, innovative methods, techniques or apparatus. The style of main sections need not conform to that of full-length papers. Short communications are 2 to 4 printed pages (about 6 to 12 manuscript pages) in length.

Reviews: Submissions of reviews and perspectives covering topics of current interest are welcome and encouraged. Reviews should be concise and no longer than 4-6 printed pages (about 12 to 18 manuscript pages). Reviews are also peer-reviewed.

Review Process

All manuscripts are reviewed by an editor and members of the Editorial Board or qualified outside reviewers. Authors cannot nominate reviewers. Only reviewers randomly selected from our database with specialization in the subject area will be contacted to evaluate the manuscripts. The process will be blind review.

Decisions will be made as rapidly as possible, and the journal strives to return reviewers' comments to authors as fast as possible. The editorial board will re-review manuscripts that are accepted pending revision. It is the goal of the IJPS to publish manuscripts within weeks after submission.

Regular articles

All portions of the manuscript must be typed double-spaced and all pages numbered starting from the title page.

The Title should be a brief phrase describing the contents of the paper. The Title Page should include the authors' full names and affiliations, the name of the corresponding author along with phone, fax and E-mail information. Present addresses of authors should appear as a footnote.

The Abstract should be informative and completely self-explanatory, briefly present the topic, state the scope of the experiments, indicate significant data, and point out major findings and conclusions. The Abstract should be 100 to 200 words in length.. Complete sentences, active verbs, and the third person should be used, and the abstract should be written in the past tense. Standard nomenclature should be used and abbreviations should be avoided. No literature should be cited.

Following the abstract, about 3 to 10 key words that will provide indexing references should be listed.

A list of non-standard **Abbreviations** should be added. In general, non-standard abbreviations should be used only when the full term is very long and used often. Each abbreviation should be spelled out and introduced in parentheses the first time it is used in the text. Only recommended SI units should be used. Authors should use the solidus presentation (mg/ml). Standard abbreviations (such as ATP and DNA) need not be defined.

The Introduction should provide a clear statement of the problem, the relevant literature on the subject, and the proposed approach or solution. It should be understandable to colleagues from a broad range of scientific disciplines.

Materials and methods should be complete enough to allow experiments to be reproduced. However, only truly new procedures should be described in detail; previously published procedures should be cited, and important modifications of published procedures should be mentioned briefly. Capitalize trade names and include the manufacturer's name and address. Subheadings should be used. Methods in general use need not be described in detail.

Results should be presented with clarity and precision. The results should be written in the past tense when describing findings in the authors' experiments. Previously published findings should be written in the present tense. Results should be explained, but largely without referring to the literature. Discussion, speculation and detailed interpretation of data should not be included in the Results but should be put into the Discussion section.

The Discussion should interpret the findings in view of the results obtained in this and in past studies on this topic. State the conclusions in a few sentences at the end of the paper. The Results and Discussion sections can include subheadings, and when appropriate, both sections can be combined.

The Acknowledgments of people, grants, funds, etc should be brief.

Tables should be kept to a minimum and be designed to be as simple as possible. Tables are to be typed double-spaced throughout, including headings and footnotes. Each table should be on a separate page, numbered consecutively in Arabic numerals and supplied with a heading and a legend. Tables should be self-explanatory without reference to the text. The details of the methods used in the experiments should preferably be described in the legend instead of in the text. The same data should not be presented in both table and graph form or repeated in the text.

Figure legends should be typed in numerical order on a separate sheet. Graphics should be prepared using applications capable of generating high resolution GIF, TIFF, JPEG or Powerpoint before pasting in the Microsoft Word manuscript file. Tables should be prepared in Microsoft Word. Use Arabic numerals to designate figures and upper case letters for their parts (Figure 1). Begin each legend with a title and include sufficient description so that the figure is understandable without reading the text of the manuscript. Information given in legends should not be repeated in the text.

References: In the text, a reference identified by means of an author‘s name should be followed by the date of the reference in parentheses. When there are more than two authors, only the first author‘s name should be mentioned, followed by ’et al‘. In the event that an author cited has had two or more works published during the same year, the reference, both in the text and in the reference list, should be identified by a lower case letter like ’a‘ and ’b‘ after the date to distinguish the works.

Examples:

Abayomi (2000), Agindotan et al. (2003), (Kelebeni, 1983), (Usman and Smith, 1992), (Chege, 1998; 1987a,b; Tijani, 1993,1995), (Kumasi et al., 2001)

References should be listed at the end of the paper in alphabetical order. Articles in preparation or articles submitted for publication, unpublished observations, personal communications, etc. should not be included in the reference list but should only be mentioned in the article text (e.g., A. Kingori, University of Nairobi, Kenya, personal communication). Journal names are abbreviated according to Chemical Abstracts. Authors are fully responsible for the accuracy of the references.

Examples:

Ogunseitan OA (1998). Protein method for investigating mercuric reductase gene expression in aquatic environments. Appl. Environ. Microbiol. 64:695-702.

Gueye M, Ndoye I, Dianda M, Danso SKA, Dreyfus B (1997). Active N2 fixation in several Faidherbia albida provenances. Ar. Soil Res. Rehabil. 11:63-70.

Charnley AK (1992). Mechanisms of fungal pathogenesis in insects with particular reference to locusts. In: Lomer CJ, Prior C (eds) Biological Controls of Locusts and Grasshoppers: Proceedings of an international workshop held at Cotonou, Benin. Oxford: CAB International, pp 181-190.

Mundree SG, Farrant JM (2000). Some physiological and molecular insights into the mechanisms of desiccation tolerance in the resurrection plant Xerophyta viscasa Baker. In Cherry et al. (eds) Plant tolerance to abiotic stresses in Agriculture: Role of Genetic Engineering, Kluwer Academic Publishers, Netherlands, pp 201-222.

Short Communications

Short Communications are limited to a maximum of two figures and one table. They should present a complete study that is more limited in scope than is found in full-length papers. The items of manuscript preparation listed above apply to Short Communications with the following differences: (1) Abstracts are limited to 100 words; (2) instead of a separate Materials and Methods section, experimental procedures may be incorporated into Figure Legends and Table footnotes; (3) Results and Discussion should be combined into a single section.

Proofs and Reprints: Electronic proofs will be sent (e-mail attachment) to the corresponding author as a PDF file. Page proofs are considered to be the final version of the manuscript. With the exception of typographical or minor clerical errors, no changes will be made in the manuscript at the proof stage.

International Journal of Physical Sciences

Table of Contents: Volume 8 Number 21 9 June, 2013

ARTICLES

ARTICLES

academicJournals

Vol. 8(21), pp. 1121-1127, 9 June, 2013
DOI: 10.5897/IJPS2013.3926
ISSN 1992-1950 © 2013 Academic Journals
http://www.academicjournals.org/IJPS

International Journal of Physical Sciences

Full Length Research Paper

Synthesis, structural and dielectric properties of zinc sulfide nanoparticles

Sagadevan Suresh

Crystal Growth Centre, Anna University, Chennai-600 025, India.

Accepted 30 May, 2013

Zinc sulfide (ZnS) nanoparticles were synthesized by the wet chemical method. The crystal structure and grain size of the particles were determined, using X-ray diffraction (XRD). The optical properties were studied by the Ultraviolet-Visible (UV-Vis) absorption spectrum. The dielectric properties of ZnS nanoparticles were examined using a HIOKI 3532-50 LCR HITESTER over the frequency range of 50 Hz – 5 MHz at different temperatures. The variation of the dielectric constant and dielectric loss were studied. The dielectric constants of the ZnS nanoparticles are high at low frequencies, and decrease rapidly when the frequency is increased. Further, electronic properties like valence electron plasma energy, Penn gap, Fermi energy and electronic polarizability of the ZnS nanoparticles, were estimated.

Key words: Nanoparticles, zinc sulfide (ZnS), x-ray diffraction (XRD), ultraviolet (UV) analysis, dielectric constant and dielectric loss.

INTRODUCTION

In recent years, many efforts have been devoted to the synthesis and study of the physicochemical characterization of nanometer-scale semiconductors. Nanoparticle synthesis has opened up alternative paths in the design of materials with new properties. The interest in semiconductor nanoparticles is justified by the fact that their fundamental physical and chemical properties can be very different from those of the bulk materials. The II - VI nanostructures with their distinct properties have become potential candidates for applications in electronics and optoelectronics. Nanosized particles of semi conducting compounds in particular display grain size dependent optoelectronic properties, due to the size quantization effects (Bangal et al., 2005). The photo emission wavelengths, the band gap and lattice parameter are strongly dependent on the grain size rendering the tailarabilty of these properties as functions of grain size possible. Such unique tunability cannot be achieved in bulk semiconductors. The biggest hurdle in nanotechnology seems to be production of uniform sized nanoparticles and the control of grain size in a few nanometer ranges with considerable reproducibility.

There has been considerable interest recently in semiconductors of nanometer dimensions due to the quantum size effect they exhibit (Pathak et al., 2012, 2013). Nanocrystalline semiconductors have electronic properties intermediate between those of molecular entities and macro crystalline solids, and are at present the subject of intense research (Weller, 1993; Henglein 1989; Dounghong et al., 1982). ZnS nanostructures have gained a lot of attention that can be attributed to the properties arising from their size in the nanometer range (Gupta et al., 1997). Nanobelts (Jiang et al., 2003; Meng et al., 2003), nanowires (Zhu et al., 2003; Verna et al., 1995), nanocables, nanorods, nanocable- aligned tetra pods, nanoparticles (Sugimoto et al., 1998) and

*Corresponding author. E-mail: sureshsagadevan@yahoo.co.in.

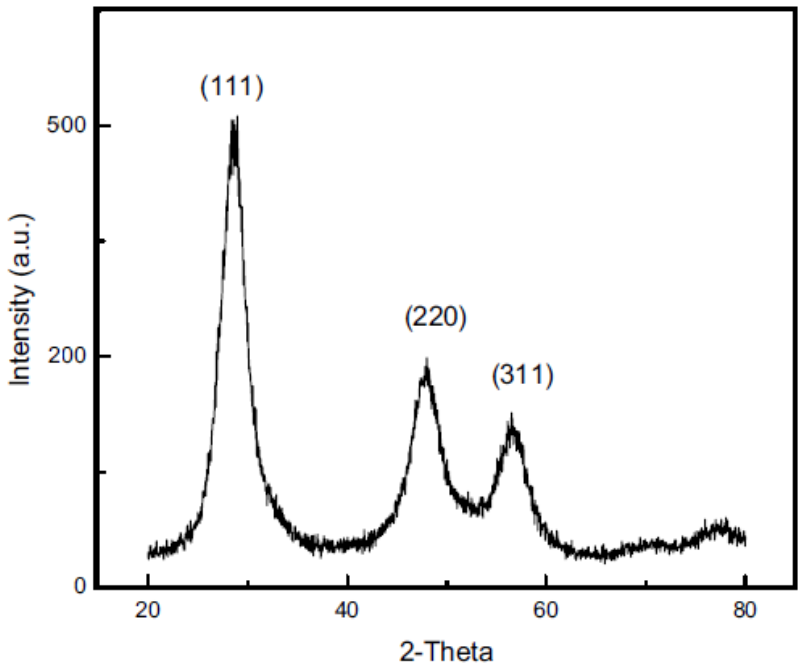

Figure 1. The XRD pattern of the ZnS nanoparticles

nanotubes were synthesized. These modify electronic, mechanical, luminescent and optical properties, and are used in nanoelectronics, photonics and as tools in biomedical applications. This paper deals with the preparation of ZnS nanoparticles using the wet chemical method. The prepared nanoparticles were characterized structurally and optically, using the powder XRD and the UV-Vis absorption spectrum. The dielectric studies have been carried out in the frequency range of 50Hz to 5MHz at different temperatures. Some of the electronic properties like plasma energy, Penn gap, Fermi energy and electronic polarizability of the ZnS nanoparticles were also determined.

EXPERIMENTAL PROCEDURE

ZnS nanoparticles were synthesized by the wet chemical method, using zinc chloride and sodium sulfide as the starting materials and were kept stirred using magnetic stirrer. The white precipitate of the ZnS nanoparticles is formed slowly in the solution. The nanoparticles were collected by centrifugation for 30 min. The obtained precipitate was then filtered and dried at 110°C for 2 h. The prepared ZnS was washed and dried. After drying, nanoparticles were grinded to obtain a fine powder for characterization. The XRD patterns of the synthesized samples were obtained using CuK_α radiation (λ = 1.5481nm), the 2θ range used was from 10 to 70° at a scanning rate of 0.02 deg/sec. The optical absorption spectrum of the ZnS nanoparticles has been taken by using the VARIAN CARY MODEL 5000 spectrophotometer in the wavelength range of 300 to 700 nm. The dielectric constant and the dielectric loss of the pellets of ZnS nanoparticles in disk form were studied using a HIOKI 3532-50 LCR HITESTER in the frequency range of 50 Hz to 5 MHz.

RESULTS AND DISCUSSION

XRD studies

The structural properties of the prepared nanoparticles were studied using X-ray diffraction. Figure 1 shows the XRD pattern of the ZnS nanoparticles.The XRD pattern exhibits prominent broad peaks at 2θ values of 28.90°, 48° and 56.50°. This shows that the ZnS nanoparticles have a zinc blended structure, and the peaks correspond to diffraction at (111), (220) and (311) planes, respectively (Mahamuni et al., 1993). The broad peak indicates the nanocrystalline behavior of the particles. The synthesized nanoparticles have good crystallinity, and the average particle size obtained using the diffraction pattern was 2.6 nm. These values are in good agreement with the reported value of the particle size 2.8 nm.

Optical absorption studies

Figure 2 shows the variation of the optical absorbance with the wavelength of the as-prepared ZnS nanoparticles. The optical absorption coefficient has been calculated in the wavelength range of 300 to 700 nm. The absorption edge has been obtained at a shorter wavelength. The optical absorption edge of the ZnS nanoparticles at 320 nm (3.80 eV), is slightly blue shifted from that of the bulk ZnS (340 nm, E_g = 3.65 eV). This nearness of the absorption peak to the bulk ZnS crystals is attributed to the near-band-edge free exactions (Mingwen et al., 2000). The broadening of the absorption

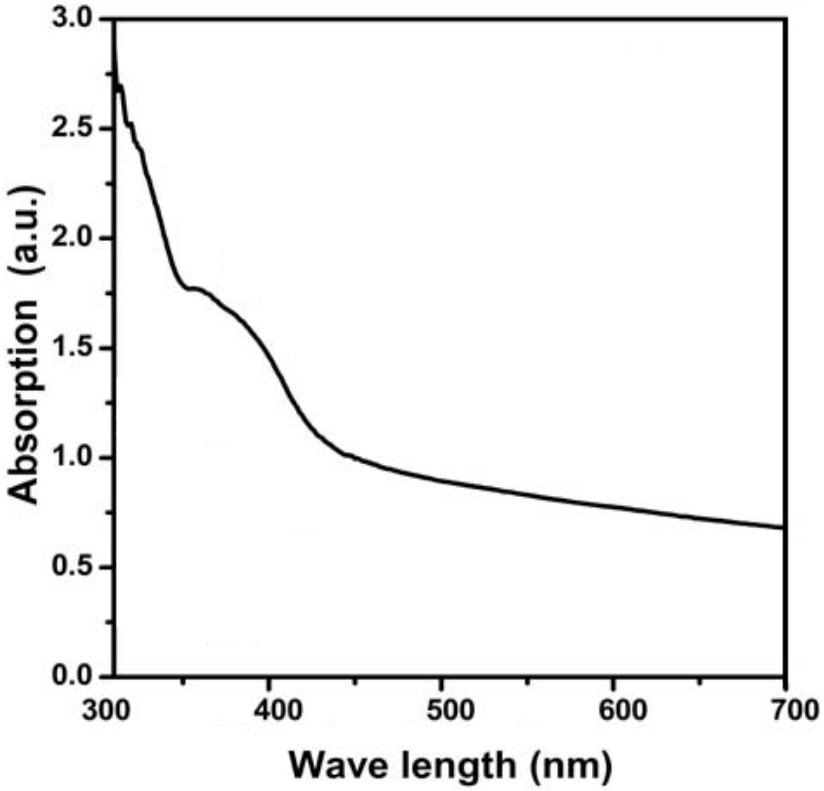

Figure 2. Optical absorption spectrum of ZnS nanoparticles.

spectrum could be due to the quantum confinement of the nanoparticles. From the absorption peak the optical energy bandgap of the ZnS nanoparticles has been calculated using the formula:

$$E_{gn} = h\nu = hc/\lambda \quad (1)$$

Where E_g, is the bandgap, *h,* is Planck's constant, *c*, is the velocity of light, and λ is the maximum absorption of the ZnS nanoparticles. The value of the bandgap is found to be 3.80 eV. The absorption band edge was shifted to 480 nm and the corresponding bandgap is 3.80 eV, which is higher compared to the bulk ZnS bandgap (3.65 eV). The measured transmittance (T) was used to calculate the absorption coefficient (α) using the relation,

$$\alpha = \frac{2.3026\log\left(\frac{1}{T}\right)}{t} \quad (2)$$

where *T* is the transmittance and *t* is the thickness of the crystal. Optical band gap (E_g) was evaluated from the absorption spectrum and optical absorption coefficient (α) near the absorption edge is given by,

$$\alpha h\nu = A\left(h\nu - E_g\right)^{1/2} \quad (3)$$

where E_g is the optical band gap of the crystal and *A* is a constant. The Tauc's plot of $(\alpha h\nu)^2$ against the photon energy ($h\nu$) at room temperature (Figure 3) shows a linear behaviour, (*α*-absorption coefficient and *h*-Planck's constant) which can be considered as an evidence of the indirect transition. Hence, assuming indirect transition between valence band and conduction band, the bandgap (E_g) is estimated by extrapolation of the linear portion of the curve to the point $(\alpha h\nu)^2 = 0$ .Using this method, the band gap of the ZnS nanoparticles was found to be 3.80 eV.

Dielectric properties of ZnS nanoparticles

Dielectric studies shows the effects of temperature and frequency on the conduction phenomenon in nano-structured materials. Dielectric behavior can effectively be used to study the electrical properties of the grain boundaries. The dielectric properties of materials are mainly due to contributions from the electronic, ionic, dipolar and space charge polarizations. Among these, the most important contribution to the polycrystalline materials

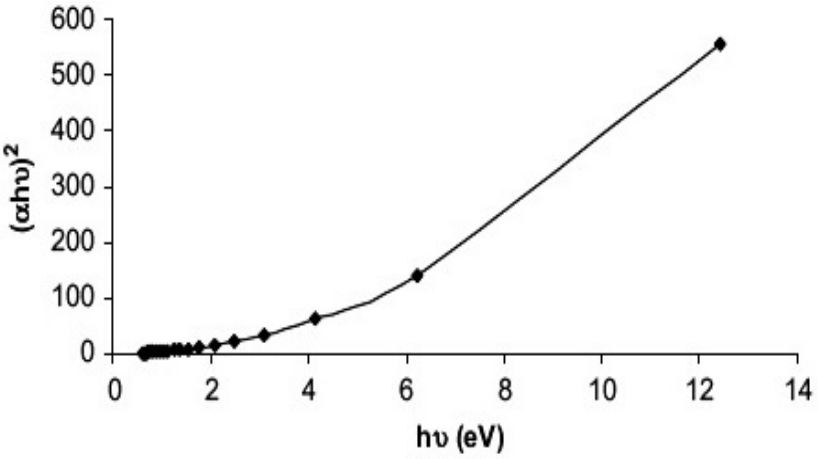

Figure 3. Plot of a vs. photon energy for ZnS nanoparticles.

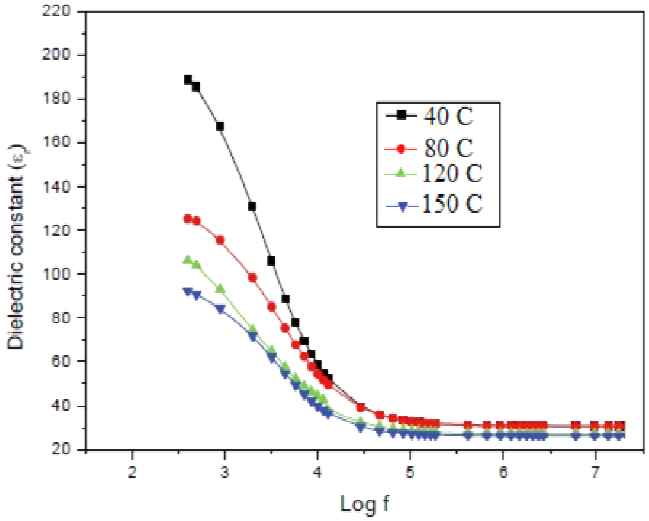

Figure 4. Dielectric constant of ZnS nanoparticles, as a function of frequencyat different temperatures.

in bulk form is from the electronic polarization, present in the optical range of frequencies. The next contribution is from ionic polarization, which arises due to the relative displacement of the positive and negative ions. Dipolar or orientation polarization arises from molecules having a permanent electric dipole moment that can change its orientation when an electric field is applied. Space charge polarization arises from molecules having a permanent electric dipole moment that can change its orientation when an electric field is applied. The dielectric parameters, like the dielectric constant (ε_r) and dielectric loss (tanδ) are the basic electrical properties of the ZnS nanoparticles. The measurement of the dielectric constant and loss as a function of frequency and different temperatures reveals the electrical processes that take place in ZnS nanoparticles and these parameters have been measured. The variations of the dielectric constant and dielectric loss of the ZnS nanoparticles at frequencies of 50 Hz to 5 MHz and at different temperatures of 40 to 150℃ are displayed in Figures 4 and 5. The dielectric constant is evaluated using the relation:

$$\varepsilon_r = \frac{Cd}{\varepsilon_0 A} \quad (4)$$

where *d* is the thickness of the sample and *A*, is the area of the sample. The results suggest that the dielectric constant and dielectric loss strongly depend on the frequency of the a.c. signal and the different temperatures of the ZnS nanoparticles. The dielectric

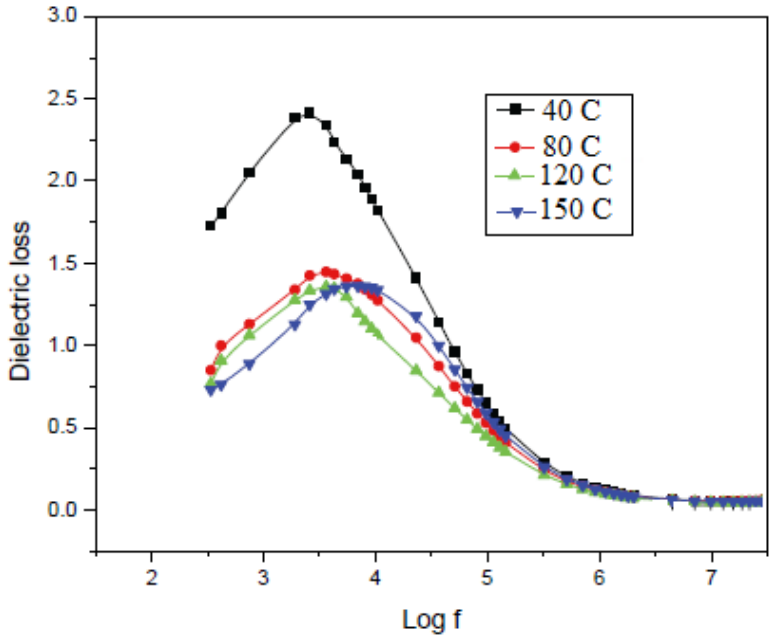

Figure 5. Dielectric loss of ZnS nanoparticles, as a function of frequencyat different temperatures.

constant has higher values in the lower-frequency (50 Hz) and then it decreases up to the high frequency (5 MHz). The dielectric constant of ZnS nanoparticles is high at lower frequencies due to the contribution of the electronic, ionic, dipolar and space charge polarizations, which depend on the frequencies (Xue and Kitamura, 2002). Space charge polarization is generally active at lower frequencies and indicates the purity and perfection of the nanoparticles. Its influence is strong at higher temperature and is noticeable in the low frequency range (Smyth, 1956).

Most of the atoms in the nanocrystalline materials reside in the grain boundaries, which become electrically active as a result of charge trapping. The dipole moment can easily follow the changes in the electric field, especially at low frequencies. Hence, the contributions to the dielectric constant increase through space charge and rotation polarizations, which occur mainly in the interfaces. Therefore, the dielectric constant of nanostructures materials should be larger than that of the conventional materials (Meera et al., 2010). One of the reasons for the large dielectric constant of nanocrystalline materials at sufficiently high temperature is the increased space charge polarization due to the structure of their grain boundary interfaces. Also, at sufficiently high temperature the dielectric loss is dominated by the reason for the sharp increase of the dielectric constant at low frequencies and at lower temperatures. As the temperature increases, the space charge and ion jump polarization decrease, resulting in a decrease in the dielectric constant.

In dielectric materials, dielectric losses usually occur due to the absorption current. The orientation of the molecules along the direction of the applied electric field in polar dielectrics requires a part of the electric energy to overcome the forces of internal friction. Another part of the electric energy is utilized for rotations of the dipolar molecules and other kinds of molecular transfer from one position to another, which also involve energy losses. In nanophase materials, the grain boundaries have an amorphous or glassy structure. All the in homogenities, defects, space charge formation etc. together produce an absorption current, which results in dielectric losses. Due to the presence of the dangling bonds on the surface layers, the nanoparticles will be highly reactive, and there is a chance of adsorption of gases like oxygen or nitrogen. These adsorbed gases can also cause an increase in the dielectric loss. In nanophase materials, in homogeneities like defects and space charge formation in the inter phase layers produce an absorption current resulting in a dielectric loss. Figure 5 shows the variation of the dielectric loss with respect to the logarithm of frequency at different temperatures of 40, 80, 120 and 150°C. Dielectric loss also shows a trend similar to the one shown by the dielectric constant. The decrease in the dielectric loss with the increase in frequency for all the temperatures suggests that the dielectric loss is strongly dependent on the frequency of the applied field. The high values of dielectric loss at low frequencies could be related to the charge lattice defect of the space charge polarization (Xue and Kitamura, 2002).

In the proposed relation only one parameter, such as the high frequency dielectric constant is required as the input, to evaluate the electronic properties, like valence

Table 1. Electronic properties of the ZnS nanoparticles

Parameter	Value
Plasma energy ($\hbar\omega_p$)	16.69eV
Penn gap (E_p)	3.56 eV
Fermi energy (E_F)	12.46eV
Electronic polarizability (using Penn analysis)	5.39 × 10^{-24} cm^3
Electronic polarizability (using Clausius-Mossotti relation)	5.40 × 10^{-24} cm^3
Electronic polarizability (using bandgap)	4.91 × 10^{-24} cm^3

electron plasma energy, average energy gap or Penn gap, Fermi energy and electronic polarizability of the ZnS nanoparticles. The theoretical calculations show that the high frequency dielectric constant is explicitly dependent on the valence electron Plasmon energy, an average energy gap referred to as the Penn gap and Fermi energy. The Penn gap is determined by fitting the dielectric constant with the Plasmon energy (Ravindra et al., 1981). The valence electron plasma energy, $\hbar\omega_p$, is calculated using the relation (Kumar and Sastry, 2005),

$$\hbar\omega_P = 28.8\left(\frac{Z\rho}{M}\right)^{1/2} \quad (5)$$

According to the Penn model (Penn, 1962), the average energy gap for the ZnS nanoparticles is given by:

$$E_P = \frac{\hbar\omega_P}{(\varepsilon_\infty - 1)^{1/2}} \quad (6)$$

where $\hbar\omega_P$ is the valence electron plasmon energy and the Fermi energy (Ravindra et al., 1981) given by:

$$E_F = 0.2948(\hbar\omega_P)^{4/3} \quad (7)$$

Then we obtained the electronic polarizability α, using a relation (Ravindra and Srivastava, 1980; Penn, 1962),

$$\alpha = \left[\frac{(\hbar\omega_P)^2 S_0}{(\hbar\omega_P)^2 S_0 + 3E_P^2}\right] \times \frac{M}{\rho} \times 0.396 \times 10^{-24}\, cm^3 \quad (8)$$

Where S_0 is a constant given by

$$S_0 = 1 - \left[\frac{E_P}{4E_F}\right] + \frac{1}{3}\left[\frac{E_P}{4E_F}\right]^2 \quad (9)$$

The value of α obtained from equation (6) closely matches with that obtained using the Clausius-Mossotti relation,

$$\alpha = \frac{3}{4}\frac{M}{\pi N_a \rho}\left[\frac{\varepsilon_\infty - 1}{\varepsilon_\infty + 2}\right] \quad (10)$$

Considering that the polarizability is highly sensitive to the bandgap (Reddy et al., 1995), the following empirical relationship is also used to calculate α,

$$\alpha = \left[1 - \frac{\sqrt{E_g}}{4.06}\right] \times \frac{M}{\rho} \times 0.396 \times 10^{-24}\, cm^3 \quad (11)$$

Where E_g is the bandgap value determined through the UV absorption spectrum. The high frequency dielectric constant of a material is a very important parameter for calculating its physical or electronic properties. All the above parameters as estimated are shown in Table 1.

Conclusion

Nanoparticles of ZnS are synthesized using the wet chemical method. The crystal structure and grain size of the particles are determined using XRD studies, and the particle size of the ZnS nanoparticle is found to be 2.6 nm. From the optical absorption spectrum, the blue shift of 320 nm with respect to its bulk counterpart is contributed by the quantum confinement effect. The value of the bandgap is found to be 3.80 eV. The dielectric constant and dielectric loss of the ZnS nanoparticles are measured in the frequency range of 50 Hz to 5 MHz at different temperatures. The dielectric studies reveal that both the dielectric constant and dielectric loss decrease with an increase in the frequency. The dielectric characterization shows the low value of the dielectric constant at higher frequencies. The dielectric constant of the ZnS nanoparticles is found to be much higher than that of the bulk ZnS. Some of the electronic properties like the plasma energy, Penn gap, Fermi energy and electronic polarizability of the ZnS nanoparticles have been calculated.

REFERENCES

Bangal M, Ashtaputre S, Marathe S, Ethiraj A, Hebalkar N, Gosavi SW, Urban J, Kulkarni SK (2005). Semiconductor Nanoparticles. Hyperfine Interact. 160:81-94.

Dounghong D, Ramsden J, Gratzel M (1982). Dynamics of interfacial electron-transfer processes in colloidal semiconductor systems. J. Am. Chem. Soc.104:2977-2985.

Gupta S, McClure JS, Singh VP (1997). Phosphor Efficiency and Deposition Temperature in ZnS: Mn A.C. Thin Film Electroluminescence Display Devices. Thin Solid Films. 33:299.

Henglein A (1989). Small-particle research: physicochemical properties of extremely small colloidal metal and semiconductor particles. Chem. Rev. 89:1861-1873.

Jiang Y, Meng XM, Liu J, Xie ZY, Lee CS, Lee ST (2003). Hydrogen-Assisted Thermal Evaporation Synthesis of ZnS Nanoribbons on a Large Scale. Adv. Mater. 15:323-327.

Kumar V, Sastry BSR (2005). Heat of formation of ternary chalcopyrite semiconductors. J. Phys. Chem. Solids. 66:99-102.

Mahamuni S, Khosravi AA, Kundu M, Kshirsagar A, Bedekar A, Avasare DB, Singh P, Kulkarni SK (1993). Thiophenol-capped ZnS quantum dots. J. Appl. Phys. 73:5237-5241.

Meera J, Sumithra V, Seethu R, Prajeshkumar JM (2010). Dielectric Properties of Nanocrystalline ZnS. Acad. Rev. 1:93-100.

Meng XM, Jiang Y, Liu J, Lee CS, Bello I, Lee ST (2003). Gallium nitride nanowires doped with silicon. Appl. Phys. Lett. 83:4241-4244.

Mingwen W, Lingdong S, Xuefeng F, Chunsheng L, Chunhua Y (2000). Synthesis and optical properties of ZnS:Cu(II) nanoparticles. Solid State Comm. 115:493-496.

Pathak CS, Mandal MK, Agarwala V (2013). Optical properties of undoped and cobalt doped ZnS nanophosphor. Mater. Sci. Semicond. Process. 16:467-471.

Pathak CS, Mandal MK, Agarwala V (2013). Synthesis and Characterization of Zinc Sulphide Nanoparticles Prepared by Mechanochemical Route. Super lattices Microst. 58:135-143.

Pathak CS, Mishra DD, Agarwala V, Mandal MK (2012). Blue Light Emission from Barium Doped Zinc Sulphide Nanoparticles" Ceramics Int. 38:5497-5500.

Pathak CS, Mishra DD, V. Agarwala V, Mandal MK (2013). Optical Properties of ZnS Nanoparticles Prepared by High Energy Ball Milling. Mater. Sci. Semicond. Process. 16:525-529.

Penn DR (1962). Wave-Number-Dependent Dielectric Function of Semiconductors.Phys. Rev. 128:2093-2097.

Ravindra NM, Bharadwaj RP, Sunil Kumar K, Srivastava VK (1981). Model based studies of some optical and electronic properties of narrow and wide gap materials. Infrared Phys. 21:369-381.

Ravindra NM, Srivastava VK (1980). Properties of liquid lead monosulfiede, lead selenide and lead telluride. Infrared Phys. 20:399-418.

Reddy RR, NazeerAhammed Y, Ravi Kumar M (1995). Variation of magnetic susceptibility with electronic polarizability in compound semiconductors and alkali halides. J. Phys. Chem. Solids. 56:825-829.

Smyth CP (1956). Dielectric Behavior and Structure. Acta. Cryst. 9:838-839.

Sugimoto T, Chen S, Muramatsu A (1998). Synthesis of uniform particles of CdS, ZnS, PbS and CuS from concentrated solutions of the metal chelates. Colloids Surf. 135:207-226.

Verna AK, Ranchfuss TB, Wilson SR (1995). Donor Solvent Mediated Reactions of Elemental Zinc and Sulfur, sans Explosion. Inorg. Chem. 34:3072-3078.

Weller H (1993). Quantized Semiconductor Particles: A novel state of matter for materials science**.** Adv. Mater. 5:88-95.

Xue D, Kitamura K (2002). Dielectric characterization of the defect concentration in lithium niobate single crystals. Solid State Commun.122:537-541.

Zhu YC, Bando Y, Uemura Y (2003). ZnS-Zn nanocables and ZnS nanotubes. Chem. Commun. 7:836-837.

academicJournals

Vol. 8(21), pp. 1190-1192, 9 June, 2013
DOI: 10.5897/IJPS12.625
ISSN 1992-1950 © 2013 Academic Journals
http://www.academicjournals.org/IJPS

International Journal of Physical Sciences

Short Communication

Mass, energy and momentum of photon in medium

Adnan Salih

Department of Physics, College of Science for Women, Baghdad University, Iraq.

Accepted 13 May, 2013

When photon travels in a medium where the velocity is lower than the speed of light, the photon possesses both the kinetic (E_k) and the potential (E_p) energy. We proved that the energy of photon ($E = nE_k$), where (n) is the refractive index, and the effective mass of photon in medium ($m' = nm$), where (m) is the effective mass of photon in vacuum. Also we proved that the momentum of photon ($p = E/c$) inside medium.

Key word: Mass, momentum, energy.

INTRODUCTION

Suppose that a photon, having momentum ħk in vacuum, enters a transparent medium with index of refraction n > 1. What is the photon's new momentum? Remarkably, there is still no definite answer. In 1908, the German Hermann Minkowski derived one possible, yet surprising answer. The photon momentum should actually increase and take the value nħk. In effect, Minkowski started from Einstein's earlier suggestion that a photon's energy is given by E = hu. Assuming a velocity c/n and p = h/λ, one observes that p = nħk. One year later, the German physicist Max Abraham proposed a different answer. Abraham argued that the photon inside the medium would have a lower velocity and lower momentum. Abraham's momentum is p = ħk/n (Campbell et al., 2005).

For nearly 100 years physicists and mathematicians have been debating the correct form of the energy momentum tensor required to describe the behavior of light at the interface between two dielectric materials of different refractive indices. The two main 'competing' theories during this time have been those proposed by Minkowski (1908) and Abraham (1909). The dilemma is whether the momentum of a photon in a medium at the single-photon level, either to multiplying or dividing the free-space value (h/λ) by the refractive index (n). In dispersive media, the situation is a bit more complicated in that we need to discriminate between phase and group indices (Milonni and Boyd, 2005; Loudon et al., 2005; Garrison and Chiao, 2004). The debate that this work started has continued till the present day, punctuated by the occasional publication of 'decisive' experimental demonstrations supporting one or other of these values (Phil. Trans. R. Soc, 2010), Stephen Barnett of the University of Strathclyde in the UK has concluded that both formulations are in fact correct, with the difference essentially boiling down to whether one considers the wave or particle nature of light (Barnett and Stephen, 2010).

A 2010 study suggested that both equations are correct, with the Abraham version being the kinetic momentum and the Minkowski version being the canonical momentum, and claims to explain the contradicting experimental results using this interpretation (Barnett and Stephen, 2010).

The experiment of Ashkin and Dziedzic showed that the action of light on the surface of a liquid was also consistent with the Minkowski momentum, although this interpretation is far from unambiguous (Gordon, 1973). The experiments of Walker et al. (1975) provide evidence that is no less convincing in favour of the Abraham form. These early experiments and the conclusions derived from them are discussed at greater length in Brevik

Email: dradnan_salih@yahoo.com.

(1979) and Pfeifer et al. (2007).

Until now there are no articles that discussed the relation between the energy, and mass of photon with refractive index and while the momentum of photon depends on the energy and mass. So why the refractive index effect is on the momentum, but there are not effects on the energy and mass of photon in the medium as indicated in current publications.

The aim of this work is to study the effect of the refractive index on energy, and effective mass of photon in medium.

ENERGY OF PHOTON IN MEDIUM

When photon travels in the transparent medium, the energy of photon can be divided into the kinetic and the potential energy of photon. It is complying with the principle of energy conservation in transparent medium. The same photon traveling in the water medium has higher kinetic energy than in the diamond medium and vice versa for the potential energy.

When the photon is traveling at the speed of light where the M and E vectors of photon are perpendicular, the photon possesses full kinetic (E_k) energy, and when a photon is brought to rest, the total energy of photon is transformed to the potential energy (E_p). This is also called the rest energy of mass. Completely stopped, all energy is transferred to matter in agreement with the experimental evidence of Hau and coworkers (Lene Hau', 2007).

The energy of photon can be further sub-divided into two portions. There are the kinetic and potential energy of photon. The energy equation of photon is described below:

$$E_t = E_k + E_p \quad (1)$$

$$E_k = pv \quad (2)$$

$$Ep = \tau \Phi \quad (3)$$

$$E = pv + \tau \Phi \quad (4)$$

Where p = momentum of photon, v = traveling speed of photon, τ = torque, angular force between electric and magnetic component, ϕ = deform angle of M and E components

$$E = h\nu\, v/c + h\nu\,(n-1)/n \quad (5)$$

Where $\tau = 2\,h\,\nu / \pi$, and $\Phi = \pi/2(1-1/n)$ (www.greatians.com/physics).

From Equation (5), The kinetic energy of photon is:

$$E_k = h\nu/n \quad (6)$$

And the potential energy is:

$$E_p = h\nu\,(n-1)/n \quad (7)$$

From Equation (6) and equation (7)

$$E_p = E_k\,(n-1) \quad (8)$$

From Equations (1 and 8):

$$E_t = n\,E_k \quad (9)$$

let a (1064 nm) photon with energy ($1.8*10^{-19}$ J) enter into medium with refractive idex (1.5), according to eqution (6, 8):

$E_k = 1.8*10^{-19}/1.5 = 1.2*10^{-19}$J
$E_p = 1.2*10^{-19}(1.5-1) = 0.6*10^{-19}$ J
$E_t = 1.2*10^{-19} + 0.6*10^{-19} = 1.8*10^{-19}$ J

These results prove that Equations (6, 8 and 9) are correct.

MASS OF PHOTON IN MEDIUM

Let (m) is the effective mass of photon in vaccum, and (m') is the effective mass in medium.
From Equation (9),

$$mc^2 = n\,m'v^2 \quad (10)$$

Where $E = mc^2$ in vaccum, and $E_k = m'v^2$ inside medium
Dividing equation (10) by c^2;

$$m = nm'/n^2 \quad (11)$$

$$m' = nm \quad (12)$$

$$E_k = nmv^2 \quad (13)$$

According to example,

$E = mc^2$
$1.8*10^{-19} = m*9*10^{16}$
$m = 0.2*10^{-35}$ Kg

From Equations (13 and 8)

$E_k = 1.5*0.2*10^{-35}*4*10^{16}$
$E_k = 1.2*10^{-19}$ J
$E_p = 1.2*10^{-19}*(1.5-1)$
$E_p = 0.6*10^{-19}$ J
$E_t = 1.2*10^{-19} + 0.6*10^{-19}$
$E_t = 1.8*10^{-19}$ J

These results prove that Equations (12 and 13) are correct.

MOMENTUM OF THE PHOTON IN MEDIUM

When photon travels in a medium where the velocity is lower than the speed of light, the photon possesses both the kinetic and the potential energy. The momentum of the photon depends on the kinetic energy only. Therefore,

$$P = E_k/v \quad (14)$$

According to Equation (6);

$$P = h\nu/nV \quad (15)$$

$$P = h\nu/C \quad (16)$$

Equation (16) represent the momentum of photon in medium which is equal to the momentum of photon in vaccum (P = E/C)

Minkowski described the momentum of light as a wave,

$$P = h/\lambda$$
$$P = h\nu/V \quad (17)$$

$$P = nE/c \quad (18)$$

In Equation (18), E is the total energy in medium, the momentum depends on kinetic energy, therefore,

$$E_k = E_t - E_p$$
$$E_k = h\nu - h\nu(n-1)/n \quad (19)$$

By using Equation (19) in (18),

$$P = n(h\nu - h\nu(n-1)/n)/c \quad (20)$$

$$P = h\nu/C \quad (21)$$

The result in Equation (21) is the same as in Equation (16)

According to the results in Equations (16 and 21) the momentum of photon in medium is equal to the momentum outside of medium.

Now if we suppose that the light is a partical according to Abraham, then;

$$P = m'v \quad (22)$$

From equation (12)

$$P = nmv \quad (23)$$

$$P = mC \quad (24)$$

$$P = h\nu/C \quad (25)$$

Abraham described the momentum of light as a particle;

$$P = mv = Ec^2/cn = h\nu/nc \quad (26)$$

By using Equation (12) in (26)

$$P = n\,h\nu/nc$$
$$P = h\nu/C \quad (27)$$

According to the results in Equations (25 and 27) the momentum of photon in medium is equal to the momentum outside of medium.

CONCLUSIONS

A simple analysis was done to prove that:

1- The total energy of photon inside medium is $E = n E_k$,
2- The effective mass of photon inside medium $m' = nm$,
3- The momentum of photon inside medium $P = /C$.

REFERENCES

Abraham M (1909). Zur Elektrodynamik bewegter Krper. Rend. Circ. Mat. Palermo. 28:1-28. (doi:10.1007/BF03018208.

Barnett S (2010-02-07). "Resolution of the Abraham-Minkowski Dilemma". Phys. Rev. Lett. 104(7):070401.

Brevik I (1979). Experiments in phenomenological electrodynamics and the electromagnetic energy–momentum tensor. Phys. Rep. 52:133-201. (doi:10.1016/0370-1573(79)90074-7.

Campbell GK, Leanhardt AE, Mun J, Boyd M, Streed EW, Ketterle W, Pritchard DE (2005). Photon recoil momentum in dispersive media. Phys. Rev. Lett. 9:170403. (doi:10.1103/PhysRevLett.94.170403).

Garrison JC, Chiao RY (2004). Canonical and kinetic forms of the electromagnetic momentum in an *ad hoc* quantization scheme for a dispersive dielectric. Phys. Rev. A 70:053826, (doi:10.1103/PhysRevA.70.053826)

Gordon JP (1973). Radiation forces and momenta in dielectric media. Phys. Rev. A. 8:14-21. (doi:10.1103/PhysRevA.8.14.

Lene Hau' (2007). http:\\ www.harvard.edu\ gazette\2007\02.08\99-hau.html'.

Loudon R, Barnett SM, Baxter C (2005). Radiation pressure and momentum transfer in dielectrics: the photon drag effect. Phys. Rev. 71:063802. (doi:10.1103/PhysRevA.71.063802.

Milonni PW, Boyd RW (2005). Recoil and photon momentum in a dielectric. Laser Phys. 15:1432-1438.

Minkowski H, Nachr G, Wiss G (1908). Die Grundgleichungen für die elektromagnetischen Vorgänge in bewegten Körpern. Nachr. Königl. Ges. Wiss. Göttingen, pp. 53–111.

Pfeifer RNC, Nieminen TA, Heckenberg NR, Rubinsztein-Dunlop H (2007). Colloquium: Momentum of an electromagnetic wave in dielectric media. Rev. Mod. Phys. 79:1197-1216. (doi:10.1103/RevModPhys.79.1197). Phil. Trans. R. Soc. A. 368:1914 927-939 (2010).

Walker GB, Lahoz DG, Walker G (1975). Measurement of the Abraham force in a barium titanate specimen. Can. J. Phys. 53: 2577–2586.

www.greatians.com/physics/wave/energy%20of%20photon.htm.

academicJournals

Vol. 8(21), pp. 1128-1132, 9 June, 2013
DOI: 10.5897/IJPS12.661
ISSN 1992-1950 © 2013 Academic Journals
http://www.academicjournals.org/IJPS

International Journal of Physical Sciences

Full Length Research Paper

Investigation of carbon monoxide concentration from anthropogenic sources in Lagos, Nigeria

Akinyemi M. L. and Usikalu M. R.*

Department of Physics, Covenant University, P. M. B. 1023, Ota, Ogun State, Nigeria.

Accepted 23 May, 2013

The work investigated the carbon monoxide (CO) concentration from anthropogenic sources in eight, different Local Council Development Authority (LCDA) in Lagos State Nigeria. The CO concentration obtained as a result of movement of cars, trucks, motorcycles, working of generators, commercial and residential activities etc., was measured using the digital carbon monoxide detector (model: DC01001) manufactured by General Tools and Instrument, New York. It was found that trucks emitted highest concentration of CO (289.64 ppm) followed by generator operated on diesel (116.23 ppm) while cooking with firewood emitted the lowest concentration of CO (5.75 ppm). Carbon monoxide concentration from residential and commercial areas, are moderate and considered safe for those in the area. On the other hand CO concentration from trucks is very high based on the US air quality index (AQI) and therefore considered unhealthy for the people. It is obvious from this study that CO concentration is generally associated with the use of fossil fuel which suggest that the less we rely on fossil fuel, the more healthy the environment.

Key words: Carbon monoxide, concentration, anthropogenic, fossil fuel, environment.

INTRODUCTION

There has been growing concern about environmental pollution problem all over the world. The people well-being is solely the mirror of a healthy environment. Air pollution can be defined as the release of substances into the air, some of which can cause problems for humans, plants, and animals. These include dust, gases, smog, acid rain, the greenhouse effect, and depletion in the ozone layer. Each of these problems has serious implications for our health and well-being as well as for the whole environment. The air pollution emanating from the anthropogenic sources has been reported to have damaging effects on the health of the exposed populace (Erhabor et al., 1992; Wanner, 1990) and in cases of extreme events, it can cause increased death rate among the exposed group.

The sources of air pollution can be grouped into 2: sources and man-made (anthropogenic) sources. Natural processes that affect air quality include volcanoes, which produce sulfur, chlorine, and ash particulates. Wildfires produce smoke and carbon monoxide. Cattle and other animals emit methane as part of their digestive process. Many forms of air pollution are man-made. Industrial plants, power plants and vehicles with internal combustion engines produce nitrogen oxides, VOCs, carbon monoxide, sulfur dioxide and particulates. In most mega cities, vehicles are the main source of these pollutants. Stoves, incinerators, and farmers burning their crop waste produce carbon monoxide, carbon dioxide, as well as particulates in rural areas. Other man-made sources include aerosol sprays and leaking refrigerators

*Corresponding author. E-mail: moji.usikalu@covenantuniversity.edu.ng.

as well as fumes from paint, varnish, and other solvents (USEPA, 2009). Pollutants can cause respiratory disease, acute intoxication and adverse reactions in sensitive people. Symptoms such as breathing difficulties, eye irritation, skin rashes and intestinal upsets appear immediately after exposure. Other chronic effects occur only after long exposures. These are often difficult to predict, and are caused by the slow build-up of chemicals in the body or the gradual accumulation that damages the human tissues. One of the major pollutants that humans are exposed to is Carbon monoxide (CO). It is a colorless, odorless, non-irritant and tasteless poisonous gas. It is slightly lighter than air. It is highly toxic to humans and animals at high concentrations. The gas consists of one carbon atom and one oxygen atom connected by a triple bond which consists of two covalent bonds as well as one dative covalent bond. Carbon monoxide is formed when there is not enough oxygen to produce carbon dioxide (CO_2), such as when operating a stove or an internal combustion engine in an enclosed space. In the presence of oxygen, carbon monoxide burns with a blue flame, producing carbon dioxide. Carbon monoxide is produced by the incomplete combustion of solid, liquid or gaseous fuels. Appliances fueled with gas, oil, kerosene, wood or coal used in boilers, engines, oil burners, gas fires, water heaters, solid fuel appliances and open fires may produce CO. All fuel burning appliances have the potential to produce CO in varying concentrations. Biologically, Carbon monoxide poisoning is the most common type of fatal air poisoning in many countries (Walker and Hay, 1999). It combines with hemoglobin to produce carboxyhemoglobin (COHb) which is ineffective for delivering oxygen to bodily tissues termed anoxemia (Fairburn et al., 1992; Omaye, 2002). It is easily absorbed through the lungs (Ernst and Zibrak, 1998). Inhaling even relatively small amounts of the gas by humans can lead to hypoxic injury, neurological damage, and even death.

Different people and populations may have a different carbon monoxide tolerance level (Thom et al., 2000). On average, exposures at 100 ppm or greater is dangerous to human health (Chichkova and Prockop, 2007). Carbon monoxide exposure may lead to a significantly shorter life span due to heart damage (Henry et al., 2006). The carbon monoxide tolerance level for any person is altered by several factors, including activity level, rate of ventilation, a pre-existing cerebral or cardiovascular disease, cardiac output, anemia, sickle cell disease and other hematological disorders (Lipman, 2006). Symptoms such as delirium and hallucinations have led people suffering poisoning to think they have seen ghosts or to believe their house is haunted (Donnay, 2004). Carbon monoxide poisoning in pregnant women may cause severe adverse fetal effects.

Based on the different contamination due to emission from both natural and man-made sources, it is therefore important to have knowledge of the air quality in a particular environment. Air quality is an indication of the healthfulness of the air based on the quantity of polluting gases and particulates (liquid droplets or tiny solid particles suspended in air) it contains. Air is considered safe when it contains no harmful chemicals and only low levels of other chemicals that become harmful in higher concentrations to humans, animals, plants, or the ecosystems (Encarta, 2009). The aim of this work is to investigate the CO concentration in the selected LCDA in Lagos State.

MATERIALS AND METHODS

The CO concentration was detected and measured with the aid of a digital carbon monoxide detector (model: DC01001) manufactured by general tools and Instrument, New York. The equipment is designed for CO detection in the range of 0 and 999 ppm, with 1 ppm resolution and accuracy of ±20% at 0 to 100 ppm; ±15% at 100 to 500 ppm; (at 20 ± 5°C, 50 ± 20% RH). Eight (8) different local council development authority (LCDA) in Lagos, Nigeria were selected for the study. The choice of the location was based on the accessibility, activities peculiar to the location and congestion in the areas. Lagos was chosen because of its status as the economic capital of Nigeria that houses a lot of central business districts. The investigated areas are Ikeja, Festac, Ikoyi, Gbagada, Apapa, Kosofe, Surelere and Isolo which can be grouped into industrial area, commercial and residential areas according to the activities predominant in such vicinity. 5 different measurements were taken for 2 h in each location in 1 LCDA and average values were taken. The CO concentration from cars, trucks, motor cycles, petrol generators, diesel generators and household kitchens and firewood cooking areas were considered in each location the same numbers of point source were considered.

RESULTS AND DISCUSSION

Figure 1 displays the mean values of the CO concentrations emitted as a result of car movements in each LCDA over a period of 2 h. The highest CO concentration was obtained in Kosofe (76.7 ppm) which can be traceable to the fact that there is high vehicular movement in this area since this is where Ojota is located. The lowest CO concentration was obtained in Isolo (32.5 ppm) this may be associated with low vehicular movement in the area during this period. According to the US AQI limit, it is only Isolo that has good healthy concern as related to CO concentration while all other locations considered can be said to have moderate healthy concern to CO concentration. Figure 2 presents the mean values of CO concentrations from motorcycles and generators that are operated with petrol and diesel. The results showed that generators operated with diesel emit more carbon monoxide than those operated with petrol. The highest CO concentration (117.36 ppm) in this group was obtained from generator operated with diesel. It was also observed that though the locations are different there is no significant difference between the CO emitted from the same set of equipment considered elsewhere. There is also no significant difference between the CO values obtained in petrol generators and motorcycles in all the locations considered. This may be because the 2

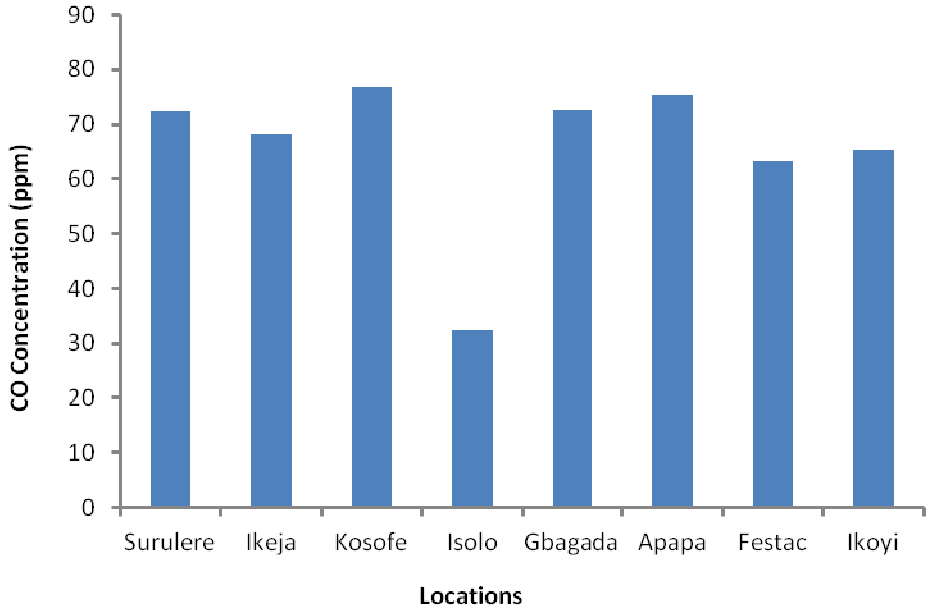

Figure 1. Mean Values of CO concentration from cars.

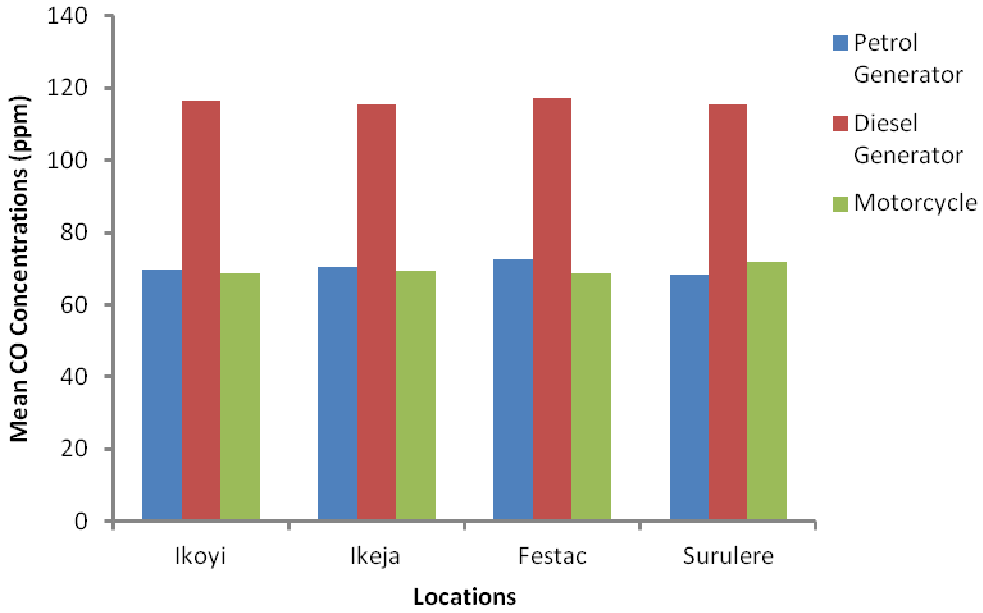

Figure 2. Mean CO Concentrations from Generators (Petrol and Diesel) and Motorcycles

equipments used petrol. Motorcycle and generator operated with petrol can be categorized as moderate healthy concern with CO concentration while those with diesel can be said to be unhealthy for sensitive people based on the US AQI limit.

Figure 3 is a bar chart representing the mean values of carbon monoxide concentration from different sources in the environment. It is observed that carbon monoxide concentration from commercial areas, residential areas and firewood cooking are relatively small compared to equipment operating on fossil fuels (that is, petrol generators, diesel generators, cars, motorcycles and trucks). This study revealed that trucks produce the highest carbon monoxide (289.64 ppm) in comparison to the other sources. The reason may be due to the type of combustion taking place in their engine as well as the fuel used (diesel). It is also observed that all equipment operated on diesel (generator and truck) emit more CO

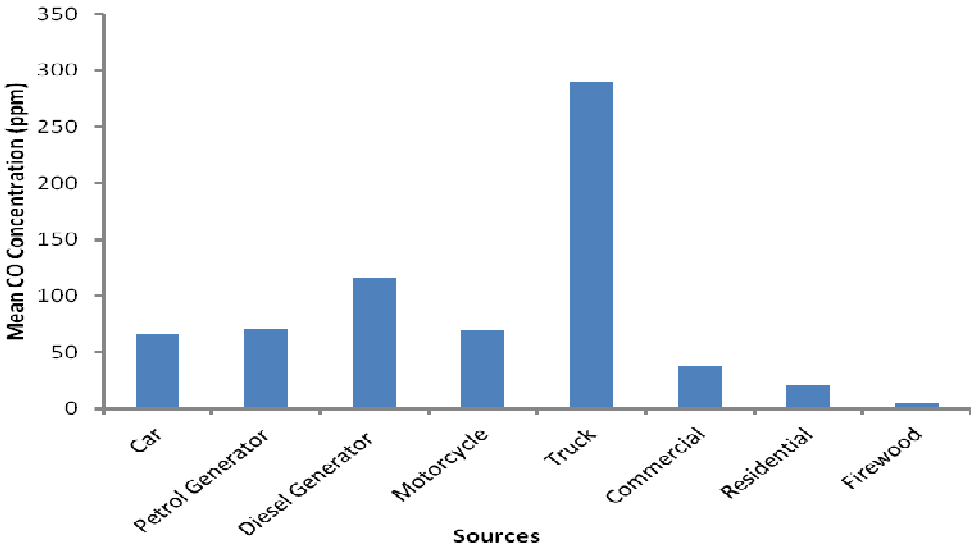

Figure 3. Variation of mean CO concentrations from all sources.

than those operated on petrol which therefore suggest that diesel combustion engine is a higher emitter of carbon monoxide than petrol. The CO concentration from the commercial area (38.17 ppm) is moderate and is within the specified healthy limit, though high when compared with that from domestic sources. This is due to many commercial activities (markets, grinding pepper, smoking, driving, wood burning, welding etc) taking place at that particular time. The source of CO from the residential area is majorly the kitchen using cooker, fridge and some household appliances. It was observed that the CO concentration from this group is within the healthy limit as it is low compared to concentration from commercial area. The CO concentration was also observed to be activity dependent, that is, it depends on what is going on in the area and does not vary with location but with what is released into the atmosphere from the different activities going on in the designated location. The area where firewood is used has the lowest CO concentration (5.75 ppm) than any other sources considered. This is because there is availability of abundant air (oxygen) for complete combustion with firewood thereby eliminating the production of carbon monoxide; a product of incomplete combustion. Chichkova and Prockop (2007) suggested that exposures to CO concentration at 100 ppm or greater are very dangerous to human health. Therefore, concentration of carbon monoxide from diesel engine and truck may be considered unhealthy to human beings and should be avoided.

CONCLUSION AND RECOMMENDATION

It has been established from this study that concentration of carbon monoxide can be obtained from anthropogenic sources. It was revealed that the equipment operated on diesel has highest concentration of carbon monoxide, followed by those operated on petrol. The major source of CO concentration observed from sources considered was from trucks and generators. It is obvious from this study that CO concentration is generally associated with the use of fossil fuel which suggests that the less we rely on fossil fuel, the more healthy the environment. The study also revealed that the more the activities in an area the higher the CO concentration from such location. Based on the results of this study, we are recommending that Government should make policy that restrict the time of movement (whether night or early in the morning) for trucks due to their high level of carbon monoxide concentration.

There is need for the government to encourage the exploitation of other sources of energy that are renewable in place of fossil fuel.

There should be frequent seminars and conferences on carbon monoxide for proper awareness of risks associated with it. It is good if each house (powered by generator) to have carbon detectors that will trigger an alarm when the CO safe limit is exceeded and the generator house should also be well ventilated.

REFERENCES

Chichkova RI, Prockop LD (2007). Carbon monoxide intoxication: an updated review. J. Neurol. Sci. 262 (1-2):122-130.

Donnay A (2004). A True Tale of A Truly Haunted House. Ghostvillage.com. Retrieved 2008-12-16.

Encarta (2009). Encyclopedia.com. <http://www.encyclopedia.com>. Assessed 23 Mar. 2011.

Encyclopedia.com. <http://www.encyclopedia.com>. Assessed 23 Mar. 2011.

Erhabor GE, Oluwole AF, Ojo JO (1992). Pulmonary effects of occupational exposure to cement dust in workers at Portland cement factory in Nigeria. Nig. Med. Practitioner. 24(3):34-37.

Ernst A, Zibrak JD (1998). Carbon monoxide poisoning. New Eng. J. Med. 339 (22):1603-1608.
Fairburn F, Tikuisis P, Kane DM, McLellan TM, Buick SM (1992). Rate of formation of carboxyhemoglobin in exercising humans exposed to carbon monoxide. J. Appl. Physiol. 72(4):1311-1319.
Henry CR, Satran D, Lindgren B, Adkinson C, Nicholson CI and Henry TD (2006).Myocardial Injury and Long-term Mortality Following Moderate to Severe Carbon Monoxide Poisoning. JAMA. 295 (4):398-402. DOI:10.1001/jama.295.4.398.
Lipman GS (2006). Carbon monoxide toxicity at high altitude. Wilderness Environ. Med. 17(2):144-145.
Omaye ST (2002). Metabolic modulation of carbon monoxide toxicity. Toxicology 180 (2):139-50. DOI:10.1016/S0300-483X(02)00387-6.
Thom SR, Raub JA, Mathieu-Nolf M, Hampson NB (2000). Carbon monoxide poisoning-a public health perspective. Toxicology 145(1):1-14. DOI:10.1016/S0300-483X(99)00217-6. PMID 10771127.US AQI http://www.thegoodairlady.com/about_air_quality_index_000284.html
USEPA (United States Environmental Protection Agency). (2009). Data from the National Concentrations Inventory, Version 2.0. Accessed 2009. http://www.epa.gov/ttn/chief/eiinformation.html.
Walker E, Hay A (1999). Carbon monoxide poisoning. BMJ.319:1082-1083.
Wanner HU (1990). Effects of atmospheric pollution on human health. J. Aerosol Sci. 21(1):5389-5396.
Zibrak JD, Ernst A (1998). Carbon monoxide poisoning. The New England J. Med. 339 (22):1603-1608.

academicJournals

Vol. 8(21), pp. 1133-1142, 9 June, 2013
DOI: 10.5897/IJPS2013.3933
ISSN 1992-1950 © 2013 Academic Journals
http://www.academicjournals.org/IJPS

International Journal of Physical Sciences

Full Length Research Paper

Harmonic curvature of the curve-surface pair under Möbius transformation

Filiz Ertem Kaya

Department of Mathematics, Faculty of Science and Arts, Nigde University, Nigde, Turkey.

Accepted 3 June, 2013

The Möbius transformation is known as a part of analysis and mostly studied by the researchers and scientist who made their investigations on analysis. But in this paper it is worked together with differential geometry. It is well known that harmonic curvature H of the curve is found by Hacısalihoglu and also harmonic curvatures $\overline{H}$ and $\overline{H}^*$ of the curve-surface pair that we call the strip as shown as (α, M) is studied by Hacısalihoglu and Ertem Kaya. We observe the image of the harmonic curvatures $\overline{H}$ and $\overline{H}^*$ of the curve-surface pair (α, M) in differential geometry under Möbius transformation in analysis. We find the images of harmonic curvatures $\overline{H}$ and $\overline{H}^*$ of the strip (α, M) by the help of the Möbius transformation. Consequently, in this paper the curvatures and the harmonic curvature H^* of the curve-surface pair under Möbius transformation is studied and H^* is not invariant for Möbius transformation is obtained.

Key words: Curve-surface pair, Möbius transformation, curvature.

INTRODUCTION

In 3-dimensional Euclidean space, a regular curve is described by its curvatures k_1 and k_2 and also a curve - surface pair is described by its curvatures k_n, k_g and t_r. The relations between the curvatures of a curve-surface pair and the curvatures of the curve can be seen in many diferential books and papers. Möbius transformations are the automorphisms of the extended complex plane C_∞:C∪{∞} that is the metamorphic bijections (Ozgür et al., 2005). M: $C_\infty \to C_\infty$ a möbius transformation M has the form

$$M(z) = \frac{az+b}{cz+d}; a,b,c,d \in C \text{ and } \begin{vmatrix} a & b \\ c & d \end{vmatrix} \neq 0 .$$

The set of all Möbius transformations is a group under composition. The Möbius transformation with $c = 0$ form the subgroup of similarities such transformations have the form $S(z) = Az + B; A, B \in C, A \neq 0$. The transformation $J(z) = \frac{1}{z}$ is called an inversion. Every Möbius transformation M of the form $S(z) = Az + B$ is a composition of finitely many similarities and inversions (Ozgür, 2010). In this paper we investigate the harmonic curvatures of the curve-surface pair under Möbius transformations. H^* and H^{**} be the image of the harmonic curvatures of the curve-surface pair and a^*, b^* and c^* be the curvatures of the curve-surface pair under

E-mail: fertem@nigde.edu.tr.

Möbius transformation. We obtain the harmonic curvature of the strip H^* is invariant for S transformation and H^* is not invariant for *J* transformation.

THE CURVE-SURFACE PAİR (STRIP)

Definition 1

Let M and α be a surface in E^3 and a curve in $M \subset E^3$. We define a surface element of M is the part of a tangent plane at the neighbour of the point. The locus of these surface element along the curve α is called a curve-surface pair and is shown as (α, M).

Definition 2

Let $\left\{\vec{t}, \vec{n}, \vec{b}\right\}$ and $\left\{\vec{\xi}, \vec{\eta}, \vec{\zeta}\right\}$ be the curve and curve-surface pair's vector fields. The curve-surface pair's tangent vector field, normal vector field and binormal vector field is given by $\vec{t} = \vec{\xi}$, $\vec{\zeta} = \vec{N}$ ($\vec{N} = \vec{n}$) and $\vec{\eta} = \vec{\zeta} \wedge \vec{\xi}$ (Hacısalihoglu, 1982).

Curvatures of the curve-surface pair and curvatures of the curve

Let $k_n = -b, k_g = c, t_r = a$ and $\left\{\vec{\xi}, \vec{\eta}, \vec{\zeta}\right\}$ be the normal curvature, the geodesic curvature, the geodesic torsion of the strip and the curve-surface pair's vector fields on α (Hacısalihoglu, 1982). Then we have

$$\vec{\xi}' = c\vec{\eta} - b\vec{\zeta}$$
$$\vec{\eta}' = -c\vec{\xi} + a\vec{\zeta}$$
$$\vec{\zeta}' = b\vec{\xi} - a\vec{\eta}.$$

We know that a curve α has two curvatures κ and τ. A curve has a strip and a strip has three curvatures k_n, k_g and t_r. Let k_n, k_g and t_r be the $-b, c$ and a. From last equations we have $\vec{\xi}' = c\vec{\eta} - b\vec{\zeta}$. If we substitude $\vec{\xi} = \vec{t}$ in last equation, we obtain

$$\vec{\xi}' = \kappa\vec{n}$$

And

$$b = -\kappa \sin\varphi$$
$$c = \kappa \cos\varphi$$

(Hacısalihoglu, 1982). From the last two equations we obtain,

$$\kappa^2 = b^2 + c^2.$$

This equation is a relation between the curvature κ of a curve α and normal curvature and geodesic curvature of a curve-surface pair. By using similar operations, we obtain a new equation as follows:

$$\tau = a + \frac{b'c - bc'}{b^2 + c^2}$$

(Ertem Kaya et al., 2010; Hacısalihoglu, 1982).

This equation is a relation between τ (torsion or second curvature of α and curvatures of a curve-surface pair that belongs to the curve α). And also we can write

$$a = \varphi' + \tau.$$

The special case: If φ is constant, then $\varphi' = 0$. So the equation is $a = \tau$. That is, if the angle is constant, then torsion of the curve-surface pair is equal to torsion of the curve.

Definition 3

Let α be a curve in $M \subset E^3$. If the geodesic curvature (torsion) of the curve α is equal to zero, then the curve-surface pair (α, M) is called a curvature curve-surface pair (strip) (Keleş, 1982).

Definition 4

Let $\overline{H}$ and $\overline{H}^*$ be the harmonic curvature of a strip in E^3. Then the harmonic curvature of the strip is the ratio of the torsion to the normal curvature of the strip and also the ratio of the torsion of the strip to the geodesic curvature of the strip, respectively (Ertem Kaya et al., 2010).

HARMONIC CURVATURES OF THE CURVE-SURFACE PAIR

In first case

If we take first curvature of a strip $k_n = -b$, then we obtain harmonic curvature of a strip is as follows;

$$\overline{H} = \frac{t_r}{k_n} = \frac{a}{-b}.$$

In second case

If we take first curvature of a strip $k_g = c$, then we obtain harmonic curvature of a strip is as follows;

$$\overline{H}^* = \frac{t_r}{k_g} = \frac{a}{c}.$$

RELATIONS BETWEEN HARMONIC CURVATURE OF A STRIP AND HARMONIC CURVATURE OF A CURVE

Lets take first curvature of the strip is $k_n = -b$ and torsion of the strip is $t_r = a$. If we write the equations of k_n, t_r and $\overline{H}$ into the harmonic curvature of the strip, then we obtain the equation

$$\overline{H} = \frac{t_r}{k_n} = \frac{a}{-b} = \frac{\varphi' + \tau}{\kappa \sin\varphi}$$
$$\overline{H} = \frac{\varphi'}{\kappa \sin\varphi} + \frac{\tau}{\kappa \sin\varphi}$$
$$\overline{H} = \frac{\varphi'}{\kappa \sin\varphi} + \frac{\tau}{\kappa}\frac{1}{\sin\varphi}$$
$$\overline{H} = \frac{\varphi'}{\kappa \sin\varphi} + H\frac{1}{\sin\varphi}$$
$$\overline{H} = \frac{\varphi'}{\kappa \sin\varphi} + H \csc\varphi.$$

The last equation is the relation between harmonic curvature of the strip and harmonic curvature of a curve in first case (Ertem Kaya, 2010; Ertem Kaya et al., 2010). Now let take first curvature of the strip is $k_g = c$ and torsion of the strip is $t_r = a$. If we write the equations of k_g, t_r and $\overline{H}^*$ into the harmonic curvature of the strip, then we obtain the equation:

$$\overline{H}^* = \frac{t_r}{k_g} = \frac{a}{c} = \frac{\varphi' + \tau}{\kappa \cos\varphi}$$
$$\overline{H}^* = \frac{\varphi'}{\kappa \cos\varphi} + \frac{\tau}{\kappa \cos\varphi}$$
$$\overline{H}^* = \frac{\varphi'}{\kappa \cos\varphi} + \frac{\tau}{\kappa}\frac{1}{\cos\varphi}$$
$$\overline{H}^* = \frac{\varphi'}{\kappa \cos\varphi} + H\frac{1}{\cos\varphi}$$
$$\overline{H}^* = \frac{\varphi'}{\kappa \cos\varphi} + H \sec\varphi.$$

The last equation is the relation between harmonic curvature of the strip and harmonic curvature of a curve in second case (Ertem Kaya, 2010; Ertem Kaya et al., 2010).

SPECİAL CASE

Theorem 1

Let $\overline{H}$ be the harmonic curvature of the strip. If the angle φ between normal vector field of the surface and binormal vector field of the curve is constant, $k_n = -b$ and $t_r = a$ is the first curvature of the strip and the torsion of the strip in E^3, we give the relation between harmonic curvatures of the strip and the curve in first case $\overline{H} = H \csc\varphi$.

Proof 1

In first case we know $\overline{H} = \frac{\varphi'}{\kappa \sin\varphi} + H \csc\varphi$ and ıf the angle φ is constant, then $\varphi' = 0$. So we take

$$\overline{H} = \frac{\varphi'}{\kappa \sin\varphi} + H \csc\varphi$$
$$\overline{H} = \frac{0}{\kappa \sin\varphi} + H \csc\varphi$$
$$\overline{H} = H \csc\varphi.$$

Theorem 2

Let $\overline{H}^*$ be the harmonic curvature of the strip. If the angle φ between normal vector field of the surface and binormal vector field of the curve is constant, $k_g = c$ and

$t_r = a$ is the first curvature of the strip and the torsion of the strip in E^3, we give the relation $\overline{H}^* = H\sec\varphi$ between harmonic curvatures of the strip and the curve in second case.

Proof 2

We know $\overline{H}^* = \frac{\varphi'}{\kappa\cos\varphi} + H\sec\varphi$ and $\varphi' = 0$. So we obtain;

$$\overline{H}^* = \frac{\varphi'}{\kappa\cos\varphi} + H\sec\varphi$$

$$\overline{H}^* = \frac{0}{\kappa\cos\varphi} + H\sec\varphi$$

$$\overline{H}^* = H\sec\varphi.$$

Theorem 3

Let the angle φ between normal vector field of the surface and binormal vector field of the curve be constant and (α, M) be strip in E^3. When the strip (α, M)'s curvatures a, b, c are not constant but harmonic curvature of strip is constant, the strip is called inclined strip $\Leftrightarrow \overline{H}^2 + \overline{H}^{*2} = cst.$ (Ertem Kaya, 2010).

Proof 3

$\Rightarrow$ Let $\overline{H}$ and $\overline{H}^*$ be the harmonic curvatures of (α, M). We should show that $\overline{H}^2 + \overline{H}^{*2}$ must be constant. We know that harmonic curvatures of the strip $\overline{H} = \frac{t_r}{k_n} = \frac{a}{-b}$ and $\overline{H}^* = \frac{t_r}{k_g} = \frac{a}{c}$. If we use these equations, we take

$$\overline{H}^2 + \overline{H}^{*2} = \left(\frac{a}{-b}\right)^2 + \left(\frac{a}{c}\right)^2$$

$$\overline{H}^2 + \overline{H}^{*2} = \left(\frac{\varphi' + \tau}{\kappa\sin\varphi}\right)^2 + \left(\frac{\varphi' + \tau}{\kappa\cos\varphi}\right)^2.$$

In here, φ is constant. So,

$\varphi' = 0$.

Since φ' is equal to zero, we obtain

$$\overline{H}^2 + \overline{H}^{*2} = \left(\frac{\tau}{\kappa}\right)^2 \frac{1}{(\sin\varphi\cos\varphi)^2}.$$

We know $\frac{\tau}{\kappa}$ and φ is constant. So $\overline{H}^2 + \overline{H}^{*2}$ must be constant $\Leftarrow$ Let $\overline{H}^2 + \overline{H}^{*2}$ be constant. In this case is we must prove (α, M) a helix strip. If we observe $\overline{H}^2 + \overline{H}^{*2}$, then we take

$$\overline{H}^2 + \overline{H}^{*2} = \left(\frac{\tau}{\kappa\sin\varphi}\right)^2 + \left(\frac{\tau}{\kappa\cos\varphi}\right)^2$$

$$\overline{H}^2 + \overline{H}^{*2} = \left(\frac{\tau}{\kappa}\right)^2 \frac{1}{(\sin\varphi\cos\varphi)^2}.$$

Since $\overline{H}^2 + \overline{H}^{*2}$ is constant, $\left(\frac{\tau}{\kappa}\right)^2 \frac{1}{(\sin\varphi\cos\varphi)^2}$ must be constant. We know φ is constant. So $\frac{\tau}{\kappa}$ must be constant. This means that the curve α is a helix and the strip (α, M) is a helix strip (Ertem Kaya, 2010; Ertem Kaya et al., 2010).

Theorem 4

Let (α, M) and $\overline{H}, \overline{H}^*$ be a curve-surface pair (strip) and harmonic curvatures of (α, M) in E^3. Let the angle φ between normal vector field of the surface and binormal vector field of the curve is constant. The strip (α, M) is inclined curve-surface pair $\Leftrightarrow \frac{\overline{H}^*}{\overline{H}} = \tan\varphi =$ constant (Ertem Kaya, 2010; Ertem Kaya et al., 2010).

Proof 4

$(\Rightarrow)$ We know $\overline{H} = \frac{H}{\sin\varphi}$ and $\overline{H}^* = \frac{H}{\cos\varphi}$ by the theorems 1 and 2. Thus

$$\frac{\overline{H}^{*}}{\overline{H}} = \frac{\overline{\frac{H}{\cos\varphi}}}{\overline{\frac{H}{\sin\varphi}}}$$

$$\frac{\overline{H}^{*}}{\overline{H}} = \tan\varphi.$$

Since φ is constant, $\frac{\overline{H}^{*}}{\overline{H}}$ is constant.

$(\Leftarrow)$Let $\frac{\overline{H}^{*}}{\overline{H}}$ be constant. Thus $\tan\varphi$ must be constant. So φ is constant. Since φ is constant, (α, M) is inclined (Ertem Kaya et al., 2010). Thus we take the strip (α, M) is inclined curve-surface pair $\Leftrightarrow \frac{\overline{H}^{*}}{\overline{H}} = \tan\varphi =$ constant (Ertem Kaya, 2010; Ertem Kaya et al., 2010).

Example 1

Let take the curve $\alpha = (\cos s, \sin s, s)$ and be the angle $\varphi = \frac{\pi}{2}$ between normal vector field of the surface and binormal vector field of the curve be constant. Thus we find the curvatures, harmonic curvatures of (α, M) and the image of the Möbius transformations of these. Firstly, let find the curvatures of the Möbius transformations. We can compute the curvatures $\kappa = \frac{1}{2}$ and the torsion $\tau = \frac{1}{2}$ of the curve α. Thus we take the curvatures of the strip (α, M)

$$b = -\kappa\sin\varphi = -\frac{1}{2}\sin\frac{\pi}{2} = -\frac{1}{2},$$

$$c = \kappa\cos\varphi = \frac{1}{2}\cos\frac{\pi}{2} = 0,$$

$$a = \varphi' + \tau = 0 + \frac{1}{2}.$$

Now we can find the harmonic curvature of curve as in the following

$$H = \tau/\kappa$$

$$H = 1 = const$$

We can say that the curve is an helix. Thus we have the harmonic curvatures of the strip.

In first case: If we take first curvature of a strip $k_n = -b$, then we obtain harmonic curvature of a strip is as follows;

$$\overline{H} = \frac{t_r}{k_n} = \frac{a}{-b} = \frac{1/2}{-(-1/2)} = 1.$$

In second case: If we take first curvature of a strip $k_g = c$, then we obtain harmonic curvature of a strip is as follows;

$$\overline{H}^{*} = \frac{t_r}{k_g} = \frac{a}{c} = \frac{1/2}{0} = \infty..$$

We can not calculate harmonic curvature in second case.

THE IMAGE OF THE CURVE-SURFACE PAIRS UNDER THE MOBIUS TRANSFORMATION

Theorem 5

Let a_1, b_1, c_1 be the curvatures of the strip (α, M) and (α, M) transform (M $(\alpha), M$) under Möbius transformation. So a_2, b_2, c_2 are the curvatures of (M $(\alpha), M$). We know that ıf (α, M) is a curvature curve-surface pair, then $a_1 = 0$ (Keleş, 1982). So we can say that ıf (α, M) is a curvature curve-surface pair, then we find (M $(\alpha), M$) is a curvature curve-surface pair.

Proof 5

Let the image of the curve α and the angle φ under Möbius transformation be the curve β and the angle θ. We know that the curvatures of α belong to:

$$\kappa^2 = b_1^2 + c_1^2$$

$$\tau = a_1 + \frac{b_1' c_1 - b_1 c_1'}{b_1^{\,2} + c_1^{\,2}},$$

$$\tau = a_1 - \varphi'(a_1 = 0).$$

Before the Möbius transformation we have $\alpha, \varphi, \kappa, \tau, a_1, b_1$ and c_1, after Möbius transformation let take $\beta, \theta, \kappa^*, \tau^*, a_2, b_2$ and c_2. And the curvatures of β

belong to:

$$\kappa^{*2} = b_2^2 + c_2^2$$
$$\tau^* = a_2 + \frac{b_2' c_2 - b_2 c_2'}{b_2^{\,2} + c_2^{\,2}},$$
$$\tau^* = a_2 - \theta'.$$

We should proof a_2 is equal to zero. Every Möbius transformation M of the Form (2) is a composition of finitely many similarities and inversions (Ozgür, 2010). Such as we can write,

$$M_{(\alpha)} = S(\alpha) o J(\alpha)\ \alpha$$
$$\beta = \beta_1 o \beta_2.$$

Let A=(x_1, x_2) and $(\alpha_1, \alpha_2, \alpha_3)$ be a point and the coordinates of α on the curve α. So from the equation $S(z) = Az + B; A, B \in C, A \neq 0$, we have

$$S(\alpha) = S(\alpha(t))$$
$$S(Z + t_j) = (AZ + B + |A| t_j) =$$
$$= (x_1\alpha_1 - x_2\alpha_2 + b_1, x_1\alpha_2 + x_2\alpha_2 + b_2, |A|\alpha_3)$$

And

$$J(Z + t_j) = \frac{\overline{Z} + t_j}{|Z|^2 + t_j^2}$$
$$J(\alpha(t)) = \left(\frac{\alpha_1(t)}{\|\alpha_1(t)\|^2}, \frac{-\alpha_2(t)}{\|\alpha_2(t)\|^2}, \frac{\alpha_3(t)}{\|\alpha_3(t)\|^2} \right).$$

For the transformation S, we have

$\kappa^* = \frac{1}{|A|}\kappa$ and $\tau^* = \frac{1}{|A|}\tau$,

$$a_2 = \tau^* + \theta'$$
$$a_2 = \frac{1}{|A|}\tau + \theta'$$
$$a_2 = \frac{1}{|A|}(-\varphi') + \theta'$$
$$a_2 = \frac{1}{|A|}\left(\frac{b_1' c_1 - b_1 c_1'}{b_1^{\,2} + c_1^{\,2}}\right) + \theta'$$
$$a_2 = \frac{1}{|A|}\left(\frac{b_1' c_1 - b_1 c_1'}{\kappa^2}\right) + \theta'$$
$$a_2 = \frac{1}{|A|}\left(\frac{b_1' c_1 - b_1 c_1'}{(|A|\kappa^*)^2}\right) + \theta'$$
$$a_2 = \frac{1}{|A|^3}\left(\frac{b_1' c_1 - b_1 c_1'}{b_2^{\,2} + c_2^{\,2}}\right) + \theta'.$$

We know that $a_1 = 0$ from the Theorem 5. We have

$$b_2 = \frac{1}{|A|}\kappa \sin\theta$$
$$b_2 = \frac{1}{|A|}\frac{b_1}{\sin\varphi}\sin\theta$$

and

$$c_2 = \frac{1}{|A|}\frac{c_1}{\cos\varphi}\cos\theta$$
$$c_1 = \frac{1}{|A|}\frac{c_2}{\cos\theta}\cos\varphi$$
$$b_1 = |A| b_2 \frac{\sin\varphi}{\sin\theta}.$$

If we apply b_1 to a_2, after some computaions, we find the equation

$$a_2 = \frac{1}{|A|}\left(\frac{b_2' c_2 - b_2 c_2'}{b_2^{\,2} + c_2^{\,2}}\right) + \theta'$$
$$a_2 = \frac{1}{|A|}(-\theta') + \theta'.$$

Now we have two cases:

Case 1. If $|A| = 1$, then we find $a_2 = 0$. That means (M $(\alpha), M$) is a curvature curve-surface pair (strip). This proves the theorem.

Case 2. If $|A| \neq 1$, then we find $a_2 = \frac{1}{|A|}\theta'(|A| - 1)$. Thus (M $(\alpha), M$) is not a curvature curve-surface pair.

Corollary 1

If $|A| = 1$, then the characterization of curvature strip is invariant under Möbius transformation.

Corollary 2

If $|A| \neq 1$, then the characterization of curvature strip is not invariant under Möbius transformation.

Example 2

Let us consider the curve $\alpha = (\cos s, \sin s, s)$ is an helix and find the image of the α and its curvatures under Möbius transformation. We know

$$J(Z + t_j) = \frac{\overline{Z} + t_j}{|Z|^2 + t_j^2}$$

Thus we have the image of α under J as

$$J(\cos s + (\sin s)i + sj) = \frac{\cos s - i \sin s + sj}{1 + s^2},$$

Then the image of the α is $J(\alpha)$ has the form

$$\beta(s) = (\frac{\cos s}{1+s^2}, \frac{-\sin s}{1+s^2}, \frac{s}{1+s^2})$$

After some computations we find the curvatures κ^* of $\beta(s)$

$$\kappa^* = \left(\frac{(1+s^2)^3 \begin{bmatrix} (\sin s - 2\cos s + 2\sin s - s^2 \sin s)^2 \\ +(\cos s + 2s\sin s + 2\cos s - s^2\cos s)^2 + (3+s^2) \end{bmatrix}}{\begin{bmatrix} (\sin s(1+s^2) + 2s\cos s)^2 \\ +\cos(1+s^2) - 2s\sin s)^2 + (1-s^2)^2 \end{bmatrix}} \right)$$

$$\kappa^* = \left[\frac{(2s^4 + 4s^2 + 18)^{\frac{1}{2}}}{2^{\frac{3}{2}}} \right] = \frac{(s^4 + s^2 + 9)}{2}$$

κ^* can not be a constant. Similarly, the torsion of $\beta(s)$ is obtained as in the following

$$\tau^* = \frac{(s^6 - s^4 - 5s^2 - 3)}{2s^4 + 4s^2 + 18}$$

τ^* can not be a constant. Consequently $J(\alpha)$ is not a helix. We have

$S(z) = Az + B$

$\kappa^* = \frac{1}{|A|}\kappa$ and $\tau^* = \frac{1}{|A|}\tau$,

then $\kappa = const > 0$, $\tau = const \neq 0$. We see that $\kappa^* = const > 0$, $\tau^* = const \neq 0$. So $S(\alpha)$ is a helix (for more details (Ozgür et al., 2005).

Theorem 6

For the transformation J, let take $\alpha = (\alpha_1, \alpha_2, \alpha_3) \in S_o^2 \Rightarrow \|\alpha\| = 1$, α is curvature strip and $J(\alpha) = \beta \in S_o^2$ [Möbius transformations take circles to circles (Ozgür, 2010)]. We have

$a_1 = \tau + \varphi', a_1 = 0,$

$a_2 = \tau^* + \varphi'$

And

$$\tau = \frac{\det(\alpha', \alpha'', \alpha''')}{\|\alpha' \wedge \alpha''\|^2},$$

$$\tau^* = \frac{\det(\beta', \beta'', \beta''')}{\|\beta' \wedge \beta''\|^2}.$$

So we have,

$\beta = (\alpha_1, -\alpha_2, \alpha_3)$

$\beta' = (\alpha_1', -\alpha_2', \alpha_3')$

$\beta'' = (\alpha_1'', -\alpha_2'', \alpha_3'')$

$\beta''' = (\alpha_1''', -\alpha_2''', \alpha_3''')$

And

$$\frac{\det(\beta', \beta'', \beta''')}{\|\beta' \wedge \beta''\|^2} = -\frac{\det(\alpha', \alpha'', \alpha''')}{\|\alpha' \wedge \alpha''\|^2},$$

$\tau^* = -\tau$.

We find $a_2 = -2\tau = 2\varphi'$ and $\varphi' = 0 \Rightarrow a_2 = 0$. Thus β is a curvature strip. This completes the proof of the theorem.

HARMONIC CURVATURE OF THE CURVE-SURFACE PAIR UNDER MOBIUS TRANSFORMATION

Let H^* and H^{**} be the image of the harmonic curvatures of the curve-surface pair and a^*, b^* and c^* be the curvatures of the curve-surface pair under Mobius transformation. In first case, we obtain the following theorem.

Theorem 7

We obtain the harmonic curvature of the strip H^* is invariant for S transformation.

Proof 7

We have

$$H^* = \frac{a^*}{-b^*} = \frac{\theta' + \tau^*}{\kappa^* \sin\theta} = \frac{\theta' + \frac{1}{|A|}\tau}{\frac{1}{|A|}\kappa \sin\theta} = \frac{|A|\theta' + \tau}{\kappa \sin\theta}.$$

If the angle θ is constant, then $\theta' = 0$. Thus we take,

$$H^* = \frac{\tau}{\kappa}.$$

Remark 1

If the angle $\theta = k\pi (k = 0,1,2...)$, we obtain $H^{**} = \infty$. So, we can take the harmonic curvature of the curve-surface pair H^{**} is not invariant for S transformation.

Theorem 8

In second case we can calculate

$$H^{**} = \frac{a^*}{c^*} = \frac{\frac{1}{|A|}\tau + \theta'}{\frac{1}{|A|}\kappa \cos\theta}.$$

If the angle θ is constant, then $\theta' = 0$. Thus we take,

$$H^{**} = \frac{\frac{1}{|A|}\tau}{\frac{1}{|A|}\kappa \cos\theta}$$

$$H^{**} = \frac{\tau}{\kappa \cos\theta}$$

$$H^{**} = \frac{\tau}{\kappa} \sec\theta.$$

Theorem 9

If the angle $\theta = k\pi (k = 0,1,2...)$ we can take the harmonic curvature of the curve-surface pair H^{**} is invariant for S transformation.

Proof 9

If $k = 0$, then we have $\cos\theta = \cos 0 = 1$. So we observe

$$H^{**} = \frac{\tau}{\kappa},$$

If $k = 1$, then
$\cos\theta = \cos\pi = -1$. So

$$H^{**} = -\frac{\tau}{\kappa},$$

If $k = 2$, then
$\cos\theta = \cos 2\pi = 1$. So

$$H^{**} = \frac{\tau}{\kappa},$$

We can do same operations for every k. Thus we have $\cos\theta$ is constant. So H^{**} is invariant for S transformation. This completes the proof of the theorem.

Theorem 10

If the curvatures a, b, c of the strip (α, M) are not constant but harmonic curvatures a^*, b^* and c^* of the strip under Möbius transformation and the angle θ are constant, then the strip is called inclined strip $\Leftrightarrow H^{*2} + H^{**2} = cst.$

Proof 10

$(\Rightarrow)$ Let H^* and H^{**} be the harmonic curvatures of (α, M) under Mobius transformation. We should show that $H^{*2} + H^{**2}$ must be constant. We know that harmonic curvatures of the strip

$$H^* = \frac{a^*}{-b^*} = \frac{\theta' + \frac{1}{|A|}\tau}{\frac{1}{|A|}\kappa \sin\theta} \text{ and } H^{**} = \frac{a^*}{c^*} = \frac{\frac{1}{|A|}\tau + \theta'}{\frac{1}{|A|}\kappa \cos\theta}.$$

If we use these equations, we take

$$H^{*2}+H^{**2}=\left(\frac{a^*}{-b^*}\right)^2+\left(\frac{a^*}{c^*}\right)^2$$

$$H^{*2}+H^{**2}=\left(\frac{\theta'+\frac{1}{|A|}\tau}{\frac{1}{|A|}\kappa\sin\theta}\right)^2+\left(\frac{\frac{1}{|A|}\tau+\theta'}{\frac{1}{|A|}\kappa\cos\theta}\right)^2$$

Since θ' is equal to zero, we obtain

$$H^{*2}+H^{**2}=\left(\frac{\tau}{\kappa}\right)^2\frac{1}{(\sin\theta\cos\theta)^2}.$$

We know $\frac{\tau}{\kappa}$ and θ is constant. So $H^{*2}+H^{**2}$ must be constant.

$\Leftarrow$Let $H^{*2}+H^{**2}$ be constant. So we must prove (α,M) a helix strip. If we observe $H^{*2}+H^{**2}$, then we take

$$H^{*2}+H^{**2}=\left(\frac{\tau}{\kappa\sin\theta}\right)^2+\left(\frac{\tau}{\kappa\cos\theta}\right)^2$$

$$H^{*2}+H^{**2}=\frac{\tau^2}{\kappa^2\sin^2\theta}+\frac{\tau^2}{\kappa^2\cos^2\theta}$$

$$H^{*2}+H^{**2}=\frac{\tau^2\cos^2\theta+\tau^2\sin^2\theta}{\kappa^2\sin^2\theta\cos^2\theta}$$

$$H^{*2}+H^{**2}=\frac{\tau^2(\cos^2\theta+\sin^2\theta)}{\kappa^2\sin^2\theta\cos^2\theta}$$

$$H^{*2}+H^{**2}=(\frac{\tau}{\kappa})^2\frac{1}{(\sin\theta\cos\theta)^2}$$

Since

$$H^{*2}+H^{**2}$$

is constant,

$$(\frac{\tau}{\kappa})^2\frac{1}{(\sin\theta\cos\theta)^2}$$

must be constant. We know θ is constant. So

$$\frac{\tau}{\kappa}$$

must be constant. This means that the curve is helix and the strip is a helix strip.

Theorem 11

The harmonic curvatures of curve-surface pair is invariant under mobius transformation.

Proof 11

It is seen obviosly from the proof of the theorem 2 and proof of the theorem 3.

Theorem 12

Let (α,M), and H^* and H^{**} be a curve-surface pair (strip) and harmonic curvatures of (α,M) under Mobius transformation in E^3. Let the angle φ between normal vector field of the surface and binormal vector field of the curve is constant. Let θ be the image of the under Mobius transformation. The curve-surface pair (α,M) is inclined curve-surface pair under Mobius transformation $\Leftrightarrow\frac{H^*}{H^{**}}=\tan\theta=$ constant.

Proof 12

We know $H^*=\frac{\tau}{\kappa\sin\theta}=\frac{H}{\cos\theta}$, Thus we obtain

$$\frac{H^*}{H^{**}}=\frac{\frac{H}{\cos\theta}}{\frac{H}{\sin\theta}}$$

$$\frac{H^*}{H^{**}}=\tan\theta.$$

Since $\tan\theta$ is constant, $\frac{H^*}{H^{**}}$ is constant.

$(\Leftarrow)$ Let $\frac{H^*}{H^{**}}$ be constant. So $\tan\theta$ must be constant. So θ is constant. Since θ is constant, (α,M) is inclined under Mobius transformation.

Theorem 13

We obtain the harmonic curvature of the strip H^* is not invariant for J transformation.

Proof 13

If (α, M) is a helix curve-surface pair (but not curvature curve-surface pair) under möbius transformation and $J(z) = \frac{1}{z}$ then the image $J(\alpha, M)$ is not a a helix curve-surface pair. So H^* is not invariant for J transformation.

Corollary 3

Harmonic curvature of the strip H^* is not invariant for Mobius transformation.

REFERENCES

Ertem Kaya F, Yaylı Y, Hacısalihoglu HH (2010). Harmonic Curvatures of a Strip in E^3, Commun. Fac. Sci. Univ. Ank. Series A1, 59(2):1-14 ISSN 1303-5991.

Ertem Kaya F (2010). Terquem and Joachimsthal Type Theorems in [PhD] Ankara University, pp. 72-78.

Hacısalihoglu HH (1982). On The Relations Between The Higher Curvatures Of A Curve and A Strip., Communications de la faculté des Sciences De Université d.Ankara Serie A1, Tome 31.

Keleş S (1982). Joachimsthal Theorems for Manifolds [PhD] Fırat University. pp. 15-17.

Ozgür NY (2010). Ellipses and Harmonic Möbius Transformations., An. ¸St. Univ. Ovidius Constanta, 18(2):201-208.

Ozgür NY, Ozgür C, Bulut S (2005). On the Images of the Helix under the Möbius Transformations, Non Linear Funct. Anal. Appl. 10(5):743-749.

academicJournals

Vol. 8(21), pp. 1143-1148, 9 June, 2013
DOI: 10.5897/IJPS2013.3897
ISSN 1992-1950 © 2013 Academic Journals
http://www.academicjournals.org/IJPS

International Journal of Physical Sciences

Full Length Research Paper

Using social network systems as a tool for political change

Jihan K. Raoof, Halimah Badioze Zaman, Azlina Ahmad and Ammar Al-Qaraghuli

Institute of Visual Informatics, UKM-Malaysia.

Accepted 30 May, 2013

Social network sites like Facebook, Twitter and YouTube play a significant role in the political arena nowadays. They are growing engagement tools that assist in improving the political process by helping electoral candidates in communicating their political programs and thoughts to the community, as well as in rallying their campaign supporters. On the other hand, voters can also use social media sites to unconditionally communicate with the candidates. This paper shows the importance of online social networking in modern society by reviewing the literature on social networks usage in politics, and showing how this usage has grown dramatically in different aspects of political life during the past few years. The growth in the use of social network sites was clearly seen after Obama's 2008 US presidential election win, which uncovered the significance of social media in political campaigns and presented new ideas about the utilization of different web 2.0 technologies in politics. Clarifying the relationship between social networking and political life will also assist researchers to study the political behaviors of society and the motivations behind political participation.

Key words: Political elections, social network systems, political campaigns, politics, web 2.0 technologies, social networking and politics.

INTRODUCTION

Before the origination of Web 2.0 technologies, the web was used mainly to search for information and to acquire knowledge (Lewis, 2006; O'Reilly, 2006). Yet, with the internet revolution which began in the mid-2000s and the development of social networking sites (Agre, 2002), users' participation and interaction took different forms such as commenting, reviewing and ranking content, sharing photos and videos, voting and surveying, building special interest groups, making new friends, etc. (Kim et al., 2010; Lilleker and Jackson, 2012).

The term Web 2.0 describes the second generation of the World Wide Web (WWW), which focuses more on the ability of people to collaborate and share information online in contrast to the first web version, where people were mainly obtaining information (O'Reilly, 2006). One of the most popular Web 2.0 technologies are the Social Network Sites (SNSs) like Facebook, Twitter, Google+, MySpace, LinkedIn, etc. (Click and Petit, 2010).

A social network is a connection network between a set of actors (organization, users, etc.), represented as graph nodes, and the relationships that tie these actors (friendship, common interests, trading partnerships, etc.) represented as graph edges. Social networking sites such as Facebook and Twitter were launched in 2004 and 2006; they allow users to register and create profiles, upload media, contribute to message threads, and keep in touch with friends, family and colleagues. Each Facebook profile has a "wall" where other users can add their posts. Since the wall is viewable by the user's friends, wall postings are basically a public conversation

*Corresponding author. E-mail: jkraoof@gmail.com. Tel: +60-104-320-566.

centered on an individual user or group.

Candidates and parties nowadays use social network sites for political purposes by communicating directly with the voters, and thereby benefiting from the lower costs of this communication mode when compared to traditional media. Therefore, they make their campaign information easily accessible to everyone especially young people (Smith, 2011), and they can mobilize supporters, gain more votes, get some attention in the traditional media like television and newspaper, and get the attention of other politicians and political journalists (Karlsen, 2012), as well as facilitate fund raising (Carpini, 2000; Vergeer, 2012). Although television remains the leading source of campaign information and election news for many candidates and parties and even for the people (Smith, 2009), some parties utilize the web 2.0 features and SNSs instead of the traditional media because they are marginalized by mainstream media (Lilleker et al., 2011).

This paper is part of a research project by the institute of visual informatics IVI in UKM-Malaysia to demonstrate the importance of the internet and social networks in politics generally and in elections specifically, to open the doors for scholars to do further studies around this subject, and to investigate the ways SNSs help in identifying potential voters for an electoral candidate and predicting the winning candidates in political elections.

A review of various resources indicates that Obama's victories in 2008 and 2012, and his extensive use of social network sites before and during the elections had attracted the attention of researchers. This paper is organized as follows: the next section explores the use of SNSs in political elections during the past decade and how it is expected to be used in the future. The following section covers the findings and conclusions of the research.

Social network sites and their political use

There is a large volume of published studies describing the role of social network systems in politics generally and elections specifically. In recent years, much more politically relevant information has become available on social network sites. The usage rate of social media, especially Facebook, by politicians increased dramatically after 2008 (Leuschner, 2012; Williams and Gulati, 2009; Williams and Gulati, 2007; 2008). Recently, Facebook ranked first in the most visited sites in the world according to Top (2011).

The increase in politically relevant information on Facebook comes from the fact that Facebook supplies electoral candidates with an enormous opportunity to have contact with the public in a very effective and inexpensive manner, and without any limitations. In addition to that, Facebook allows the public to share their opinions, and participate and engage in the political process freely (Westling, 2007; Williams and Gulati, 2007).

From a political point of view, it is very easy to employ SNSs as a tool to communicate directly with the voters. The increase in the number of supporters and voters using Facebook to get political information has led to the increasing number of politicians using SNSs (Smith, 2009; Smith et al., 2008).

Fast, easy, cheaper and with no control, the internet is spreading information make rumors easily created and reach vase audience which can effect on the number of support the candidate gains from the internet generally and from social media specially but still the significant use of internet in the election and campaigns dramatically increased in the last 10 years according to some statistics submitted by Pew Internet and American Life Project (Garrett, 2010). Statistics in the Associated Press (Press, 2012) showed that, the number of active Facebook users has increased significantly over the past few years: At the end of 2004, Facebook had 1 million registered users only, but this went up to 12 million users by the end of 2006 and 100 million by 2008, and this number jumped to 1 billion in September 2012. Other resources show that, Twitter had a similar surge in the number of users, which increased from around one million users in 2008 (Arrington, 2008) to 500 million users in 2012 (O'Carroll, 2012). These statistics on the use of these free media resources can be considered as evidence for the increasing awareness and knowledge of people.

Politicians utilize social networks and smartphones to reach out to as many voters as possible. By observing political candidates' engagements on social network sites, especially on Twitter, Hong and Nadler found indicators that, political events affect the number of people responding positively to candidates (Hong and Nadler, 2012).

A study done by Lilleker et al. (2011) showed that political parties within Great Britain, France, Germany and Poland that stood in the 2009 European parliamentary elections followed a strategy adopting all the features of web 2.0 and the internet to give their supporters the chance to talk to each other or to talk with party leaders directly.

In countries with a restricted media environment, people try to find alternative forms of media to state their opinions and to engage with political issues. In Malaysia, the number of Facebook users is increasing rapidly. Over 50% of Malaysia's population uses Facebook; this rate constitutes 78% of the Malaysian online community (Bakers, 2012). Facebook has become the most popular website in the country since 2010, ahead of the popular search engines Google and Yahoo and the online video sharing site YouTube (Alexa, 2012; Nardi, 1996).

The increase in the usage of the social media can be considered as an indicator of the increased political awareness in Malaysia. Besides, opposition supporters are using this technology as an alternative way to engage in politics and express their opinions freely (Smeltzer and

Keddy, 2010). Using Malaysia as a case study, Smeltzer and Keddy (2010) looked into the potential of Facebook being used as a tool for political change. They examined if, how, and to what extent Facebook usage can support critical political activities inside and outside formal electoral politics in a restricted media environment. Since the start of Malaysia's revolution in IT in the mid-1990s, Smeltzer and Keddy (2010) found that, there is an increasing number of opposition parties and candidates who use SNSs, especially after Obama's victory in the US 2008 election. Many parties and candidates have leveraged on Obama's effective utilization of web 2.0 technologies in politics, especially in the elections, by employing these technologies as tools for increasing the awareness of people, especially the youth, to spread their political views and to attract voters and gain their support. SNSs have helped these politicians to break the barriers imposed on the domestic media by the governing leading parties.

Facebook as a political support tool

Social networks can impact not only the share of the votes, but also the awareness of people and provide an appropriate venue for them to participate in the political process (Mascaro and Goggins, 2010; Vitak et al., 2011), to hold rallies to demand for their rights and to let their voices reach the specialists and politicians in order for change to occur (Gil de Zúñiga, 2012).

Social media plays an expanding role in increasing people's awareness and knowledge about their rights and the necessity of their engagement in the political scene through their participation in SNSs. This has prompted some governments to reconsider polices and to introduce restrictions on the internet and social media. A good example of this was witnessed in Singapore through the changes in policies that started in 2008 and continued until the 2011 parliamentary elections, due to the wide use of social networks (Skoric et al., 2012). They found in their study of 2000 respondents from Singapore that, the ruling party's increasing control of traditional media and newspapers had led to a growing number of people using social media to express their political opinions, and that in turn led to an increasing number of political activists participating in political rallies during the election.

A study that was conducted by Robertson et al. (2009), a group of researchers in Hawaii University aimed at better understanding social networking in the context of politics, showed the linkage patterns of posters which added comments to the Facebook walls of three major candidates: Barack Obama, Hillary Clinton and John McCain in the period before the 2008 U.S. presidential election. This study showed how the posters used links to different information sources to communicate their points or thoughts to others (Robertson et al., 2009; 2010).

Social network tools, especially Facebook and blogs, play a significant role in changing society's viewpoints, which in turn helps in promoting people's revolution against non-democratic governments, an example of which was clearly seen in Pakistan in November 2007. The government controlled all the television channels and newspapers so, the youth overcame these barriers by using Facebook, blogs and mobile text messages to communicate and pass political information to others (Shaheen, 2008).

Besides that, Facebook recently played a major role in the Arab Spring. This event has attracted many researchers to find out the impact of the political messages posted on Facebook walls on the users' political trends, their political interest, and on the political arena in general (Yousif and ALsamydai, 2012).

To show how the people in Arab countries (Egypt, Libya, Tunisia, and Syria) employed SNSs in politics and how they used Facebook to participate in political discussion, Khashman (2011) analyzed the Facebook pages of users in the countries that witnessed a political unrest during the still-continuing Arab Spring. Focusing on Egyptian pages on Facebook, Khashman (2011) found that there were more negative pages than positive ones within Facebook about the ousted Egyptian President (Khashman, 2011).

Mobile systems like smartphones and tablets help people to access the internet easily from public places. This in turn facilitates the use of social media. These systems played a big role in the 2011 revolutions in Tunisia and Egypt, by making it easier to pass information among the protesters, and to deliver messages faster to vast audiences, especially the youth. The increasing number of Egyptian people using the internet and social media, the people's anger caused by the accumulated likelihoods of unemployment for youth, and the restrictions imposed by the government on local media, made Facebook the most appropriate space to express and discuss opinions freely. This led to calls for participation in a revolt aimed at political change which succeeded in altering the country's 40 years long regime, even though the Egyptian government tried to control the traditional media, and mobile access to the internet (Attia et al., 2011; Skoric et al., 2012; Tufekci and Wilson, 2012).

As a result of Egypt's revolution and the increasing use of Facebook and its effects, many governments, like the Chinese government, have taken precautions such as blocking access to social media sites to limit their impact on their people (Ho, 2011). During the Iranian presidential election in 2009, the government also blocked access to Facebook because the opposition candidates were using the site in their political campaigns (Bazzi, 2009).

Social network sites in recent elections

The United States was the first country to use the Internet on a large scale in the mid-1990s (Leuschner, 2012;

Vergeer, 2012). After Obama's victory in the 2008 US election, researchers paid more attention to social media tools. Numerous studies were done, examining how Obama influenced the electoral politics by using social media tools, and how these technologies secured his victory and helped in raising enough funds to win the elections.

In 2008 Obama used various web-based tools such as the Obama'08 Web site (barackobama.com), Twitter, Facebook, MySpace, E-mails, iPhone application, and the Obama-Biden transition project (change.gov) site for his campaign. Foreman listed some of the reasons behind Obama's winning of the 2008 presidential election: Obama raised more money than his competitors and utilized social media effectively. That facilitated the dissemination of information especially with the availability of smart phones among enthused youths, winning the support of the youths and leveraging on their ability to influence their families and friends to vote for Obama (Foreman, 2012).

Obama used these tools in an ingenious way that converted online participants to fans and supporters who showed their support by voting for him (Cogburn and Espinoza-Vasquez, 2011; Gil de Zúñiga, 2012; Lilleker and Jackson, 2012). He established a dramatic increase in the use of ICT in politics (Borins, 2009; Kuusk, 2012; Milliken, 2011). Again, similar patterns led to Obama's more recent victory in the 2012 presidential election.

The 2008 presidential elections witnessed several contrasts between how Obama and other candidates utilized social network sites in their campaigns. Obama's strategy led him to reach electorates and win the 2008 election, but other candidates regarded applying social network sites in their strategy as a less important issue since there were no previous facts to prove the relationship between these technologies and success in a presidential election, nor evidence that these technologies contribute in spreading information about their campaigns (O'Brien, 2012).

Despite the fact that traditional media like television and newspapers still play an important role in political campaigns, many candidates and parties show an increased interest in social media, especially after President Obama benefited from the utilizing of SNSs to mobilize and gain access to a greatest number of voters in the 2008 US presidential election (Milliken, 2011).

Milliken also examined how four of the candidates running in the 2012 presidential election: Michele Bachman, Ron Paul, Mitt Romney, and President Obama benefited from employing social media and the Internet on a large scale in their campaigns. These media provided a platform for candidates' words and messages without any kind of filtering or modification which usually happens in traditional media, although each candidate used them in different ways.

European parties used social media as they were influenced by the American success story (Karlsen, 2012). Lilleker et al. (2011) investigated how UK political parties utilized and employed the internet and Web 2.0 in their campaigns during the 2010 UK general elections. He noted that some UK parties were, to some degree, mirroring the strategy of Obama in their campaigns (Lilleker and Jackson, 2012).

Research has continued to ask whether the social networks, especially Facebook, will continue boosting user participation in politics and encourage a strong relationship between the participants, and whether the social networks will make the relationship superficial and isolated from real life. Researchers have found that Facebook is considered by politicians as a chance to attract people to use social networking as a public venue to meet others and to form groups to exchange political information, as well as to communicate with other users who share the same viewpoints. Forming such groups on Facebook helps many users who are seeking political information as noted by Gil de Zúñiga, (2012); Mascaro and Goggins, (2010).

This paper has revealed how the use of social networking sites in politics showed different trends, especially after Obama's victory in the 2008 presidential elections. Previous research showed how users, politicians and candidates used different social media networks for different purposes such as communication, dissemination of information, arrangements for engagement and requests for donations, etc. Several studies showed statistical results that demonstrated a rise in the use of these technologies by politicians and users.

Williams and Gulati (2008) found that 32% of candidates for the U.S. senate and 13% of candidates for the parliament house updated their Facebook profiles at least once for the 2006 elections, and this helped them in gaining extra votes. Furthermore, all presidential candidates in 2008 had social network profiles.

Obama's campaigns were distinguishable in that, he utilized SNSs in a very professional way, and in the 2012 elections, he tried to use each facility available even more extensively than he had in the 2008 campaign. Obama often updated his Facebook page and his web site in the 2008 election, trying to communicate and reach young voters as he believed that the young voters were important, whereas his competitor McCain only updated his Facebook page three times over the election period, and these three updates were made nearer to the election date (Payne, 2009). This lowly administration of social media left a gap between McCain and his followers and giving Obama great opportunity in attracting voters and boosting their attendance(Choy, 2012) (Figure 1).

Subsequent to the 2008 elections, Obama used social media tools extensively again in the 2012 presidential election, gaining more online supporters than his competitor, as illustrated in Figure 2.

Obama's competitor, Mitt Romney, paid more attention to social media and consequently gained a bigger share

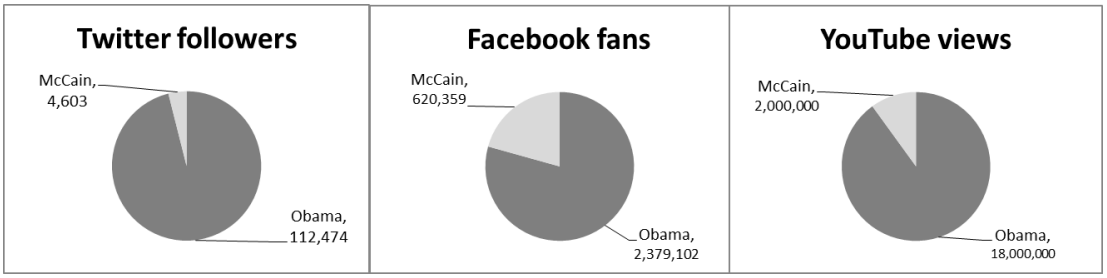

Figure 1. How each candidate used social media in the 2008 US presidential election (Metzgar and Maruggi, 2009).

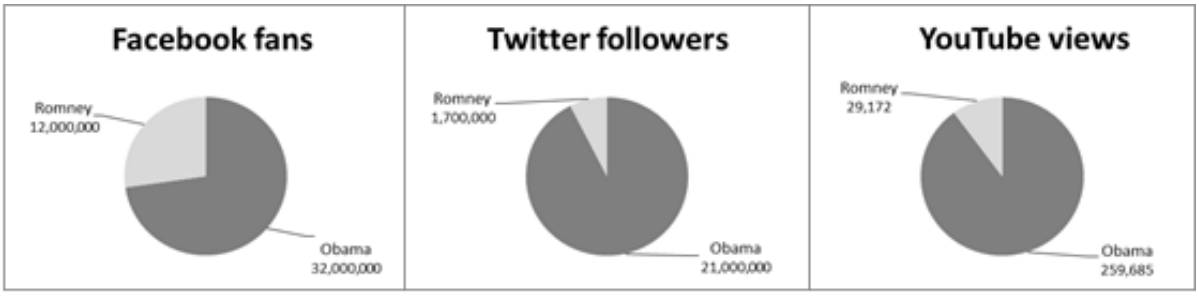

Figure 2. How each competitor in the 2012 presidential election used social media (Burrus, 2012).

of the supporters than Obama's former competitor, John McCain; however, Romney's campaign did not utilize social media as a core and base strategy during the elections as Obama did (Burrus, 2012), and this still left a relatively big gap between Obama and his competitor.

A study conducted in Norway provided statistical evidence that, the younger candidates in the 2009 Norwegian election campaign used Facebook for their campaigns more than the older ones. Over 80% of the candidates aged 25 years and below used Facebook as a part of their campaigns, and 73% of the candidates between 26 to 35 years old used it for the same purpose. There was a lower usage rate of Facebook by candidates between 36 to 50 years old, whilst only a quarter of the candidates aged 51 and above used the site.

In contrast, there were differences in the usage of Twitter, with candidates between 36 to 50 years old using Twitter more extensively than candidates below 35 years old (Karlsen, 2012), and this indicates that micro blogging is more attractive to older people while the content-rich Facebook attracts younger people.

Conclusion

This paper concludes that, social media is used as a continuously expanding communication channel between candidates and voters. The research has discussed the effectiveness of Facebook as a social network site in political elections to rally candidates' supporters, as well as to make political information available to users of social network systems.

Traditional media like television and newspapers is still significant and important in political campaigns for fast circulation of political information through the internet; this in turn makes rumors easily spreadable. Notwithstanding this, the research predicts that, the number of politicians, especially election candidates employing SNSs in their campaigns will rise after Obama's successful re-election as the US president in 2012 since his campaign focused significantly on employing web 2.0 features effectively to influence potential voters and gain their support.

This paper will give a better insight to politicians, journalists, political analysts, and electoral candidates about how others used SNSs as well as how far they may benefit from these technologies. This will, in turn, make them use SNSs as another source of information for further analysis and understanding of the political process.

This review illuminate the need for further study on the possibility of politicians and specialists' using web 2.0 technologies to predict potential voters for electoral candidates. Consequently, this may lead to predicting the winning candidate in a political election.

REFERENCES

Agre PE (2002). Real-time politics: The Internet and the political process. Inform. Soc. 18(5):311-331.

Alexa (2012). Top Sites in Malaysia Retrieved 13 Nov 2012, from http://www.alexa.com/topsites/countries/MY
Arrington M (2008). End Of Speculation: The Real Twitter Usage Numbers Retrieved 23 January 2013, from http://techcrunch.com/2008/04/29.
Attia AM, Aziz N, Friedman B, Elhusseiny MF (2011). Commentary: The impact of social networking tools on political change in Egypt's. Elect. Com. Res. Appl. 10(4):369-374.
Bakers S (2012). Malaysia Facebook Statistics. URL: http://www.socialbakers.com/facebook-statistics/malaysia Retrieved 18-Nov, 2012.
Bazzi M (2009). Iran elections: latest news.
Borins S (2009). From online candidate to online president. Int. J. Public Admin. 32(9):753-758, 32(9):753-758.
Burrus D (2012). Did Social Media Play a Role in Obama's Victory?
Carpini MXD (2000). Gen. com: Youth, civic engagement, and the new information environment. Pol. Commun. *17*(4):341-349.
Choy M (2012). US Presidential Election 2012 Prediction using Census Corrected Twitter Model. *arXiv* preprint arXiv:1211.093*8*.
Click A, Petit J (2010). Social networking and Web 2.0 in information literacy. Int. Inform. Lib. Rev. 42(2):137-142.
Cogburn DL, Espinoza-Vasquez FK (2011). From networked nominee to networked nation: Examining the impact of Web 2.0 and social media on political participation and civic engagement in the 2008 Obama campaign. J. Pol. Market. 10(1-2):189-213.
Foreman SD (2012). Top 10 reasons why barack obama won the us presidency in 2008 and what it means in the 2012 election. Fla. Political Chronicle 20(1549-1323).
Garrett RK (2010). Rumors and the Internet in the 2008 US Presidential election. Commun. Res. 37(2):255-274.
Gil de Zúñiga H (2012). Social media use for news and individuals' social capital, civic engagement and political participation. J. Computer-Mediated Commun. 17(3):319-336.
Ho S (2011). China Blocks Some Internet Reports on Egypt Protests. Vooice of America News.
Hong S, Nadler D (2012). Which candidates do the public discuss online in an election campaign?: The use of social media by 2012 presidential candidates and its impact on candidate salience. Government Information Quarterly.
Karlsen R (2012). A Platform for Individualized Campaigning? Social Media and Parliamentary Candidates in the 2009 Norwegian Election Campaign. Policy Internet 3(4):1-25.
Khashman N (2011). The Facebook Revolution: An Exploratory Analysis of Public Pages during the Arab Political Unrest.
Kim HN, Jung JG, El Saddik A (2010). Associative face co-occurrence networks for recommending friends in social networks.
Kuusk L (2012). Social media we can believe in: How social media helped Barack Obama to become the president.
Leuschner K (2012). The Use of the Internet and Social Media in US Presidential Campaigns: 1992-2012 more.
Lewis D (2006). What is web 2.0? Crossroads 13(1):3-3.
Lilleker DG, Jackson NA (2012). Towards a more participatory style of election campaigning: The impact of web 2.0 on the UK 2010 general election. Policy Internet 2(3):69-98.
Lilleker DG, Koc-Michalska K, Schweitzer EJ, Jacunski M, Jackson N, Vedel T (2011). Informing, engaging, mobilizing or interacting: Searching for a European model of web campaigning. Eur. J. Commun. 26(3):195-213.
Mascaro CM, Goggins SP (2010). Collaborative Information Seeking in an Online Political Group Environment.
Metzgar E, Maruggi A (2009). Social media and the 2008 US presidential election. J. New Commun. Res. 4(1):141-165.
Milliken K (2011). Media use in the 2012 presidential campaign. Ball State University.
Nardi BA (1996). Studying context: A comparison of activity theory, situated action models, and distributed cognition. Context and consciousness: Activity theory and human-computer interaction. pp. 69-102.
O'Brien (2012). Social media in 2012 elections will make 2008 look like digital dark ages Retrieved 23 January 2013, from http://www.siliconvalley.com.
O'Carroll L (2012). twitter-users-pass-200-million Retrieved 23 January 2013 from http://www.guardian.co.uk/technology.
O'Reilly T (2006). Web 2.0 compact definition: Trying again.
Payne A (2009). The New Campaign: Social Networking Sites in the 2008 Presidential Election.
Press TA (2012). Number of active users at Facebook over the years Oct 23, 2012. Retrieved Jan 22, 2013, from http://bigstory.ap.org/article/number-active-users-facebook-over-years-3.
Robertson SP, Vatrapu RK, Medina R (2009). The social life of social networks: Facebook linkage patterns in the 2008 US presidential election.
Robertson SP, Vatrapu RK, Medina R (2010). Online video "friends" social networking: Overlapping online public spheres in the 2008 US presidential election. J. Inform. Technol. Polit. 7(2-3):182-201.
Shaheen MA (2008). Use of social networks and information seeking behavior of students during political crises in Pakistan: A case study. Int. Inform. Lib. Rev. 40(3):142-147.
Skoric MM, Pan J, Poor ND (2012). Social Media and Citizen Engagement in a City-State: A Study of Singapore. Paper presented at the Sixth International AAAI Conference on Weblogs and Social Media.
Smeltzer S, Keddy D (2010). Won't You Be My (Political) Friend? The Changing Face (book) of Socio-Political Contestation in Malaysia. Can. J. Dev. Stud./Revue canadienne d'études du développement. 30(3-4):421-440.
Smith A (2009). The Internet's role in campaign 2008. Pew Internet & American Life Project, 15.
Smith AW, Rainie H, Internet P, Project AL (2008). The internet and the 2008 election: Pew Internet and American Life Project.
Smith KN (2011). Social Media and Political Campaigns. [Thesis Projects].
Top A (2011). 500 Global Sites, 2010 Retrieved 15 Nov, 2012, from URL: http://www.alexa.com/topsites.
Tufekci Z, Wilson C (2012). Social media and the decision to participate in political protest: Observations from tahrir square. J. Commun. pp. 363–379.
Vergeer M (2012). Politics, elections and online campaigning: Past, present... and a peek into the future. New Media and Society.
Vitak J, Zube P. Smock A, Carr CT, Ellison N, Lampe C (2011). It's complicated: Facebook users' political participation in the 2008 election. Cyber Psychol. Behav. Soc. Netw. 14(3):107-114.
Westling M (2007). Expanding the public sphere: The impact of Facebook on political communication. Dissertations and Theses.
Williams C, Gulati G (2009). Social networks in political campaigns: Facebook and Congressional elections 2006, 2008.
Williams CB, Gulati GJ (2007). Social networks in political campaigns: Facebook and the 2006 midterm elections.
Williams CB, Gulati GJ (2008). The political impact of Facebook: Evidence from the 2006 midterm elections and 2008 nomination contest. New York 1(1):272-291.
Yousif RO, ALsamydai MJ (2012). The Impact of the Political Promotion via Facebook on Individuals' Political Orientations. Int. J. Bus. Manage. 7(10):85.

academicJournals

Vol. 8(21), pp. 1149-1160, 9 June, 2013
DOI: 10.5897/IJPS12.554
ISSN 1992-1950 © 2013 Academic Journals
http://www.academicjournals.org/IJPS

International Journal of Physical Sciences

Full Length Research Paper

Detection and wavelet analysis of acoustic emission signal from partial discharge captured by multimode optical fiber and piezoelectric sensors in insulation oil

M. M. Yaacob[1], M. A. Alsaedi[1]*, R. Abdul Rahman[2], N. Bidin[3], Wajaht Maqbool[1], Nasir A. Al-geelani[1] and R. Hosseinian[3]

[1]Faculty of Electrical Engineering, Universiti Teknologi Malaysia, 81310 UTM Skudai, Johor, Malaysia.
[2]The Institute of Advanced Photonic Sciences, Faculty of Science, Universiti Teknologi Malaysia, 81310 Skudai, Johor, Malaysia.
[3]Department of Physics, Faculty of Science, Universiti Teknologi Malaysia, 81310 Skudai, Johor, Malaysia.

Accepted 13 May, 2013

High-voltage transformer is the most critical and expensive component in a power system network in order to ensure the stability of the system. Partial discharge (PD) detection is a technique widely used for high voltage equipment insulation condition monitoring and assessment. In this paper, the characteristics of two acoustic sensors multimode fiber optical (FO) and piezoelectric (PZT) sensor have been successfully explored and monitor the condition of high voltage equipment insulation. Both the sensors were placed in an oil tank in which optical breakdown was produced by neodymium-doped yttrium aluminum garnet (Nd:YAG) laser (1064 nm) device. The optical signal of light source was linked by a photodetector which was also connected with multimode fiber (MMF) by means of a fiber optical adapter. The data obtained by both sensors were then analyzed in time and frequency domain.

Key words: Fiber optical sensor, piezoelectric sensor, acoustic emission, optical breakdown, partial discharge, wavelet analysis.

INTRODUCTION

The strong electric field has some hidden mysteries that appear as electrochemical and plasma-chemical reactions around the high voltage appliances like cables and transformers. One of the mysterious phenomenon is small electrical sparks that are present in an insulation medium which deteriorates the material as a result insulation becomes weak to sustain that high voltage and causes electrical breakdown. In case of cables, the entrapped gas condition in void spaces of the medium is the root cause of this phenomenon which changes the electro-physical nature of the medium. In case of power transformers, high non-uniform electric field is present near the vicinity of devices which produce degradation and aging effect for insulators. This micro discharge activity near the high voltage devices is called partial discharge (PD) phenomenon which generates acoustic emission (AE) that can be measured and used for the diagnostic and monitoring study of power transformer before complete failure. In usual cases when electric field exceeds the limit of local ionization threshold of dielectric insulation, the PD phenomenon occurs (Boffi et al., 2006). Generally, insulation of high voltage power

*Corresponding author. E-mail: maliksaady@yahoo.com. Tel: +61-07-5535695. Fax: +61-07-5578150.

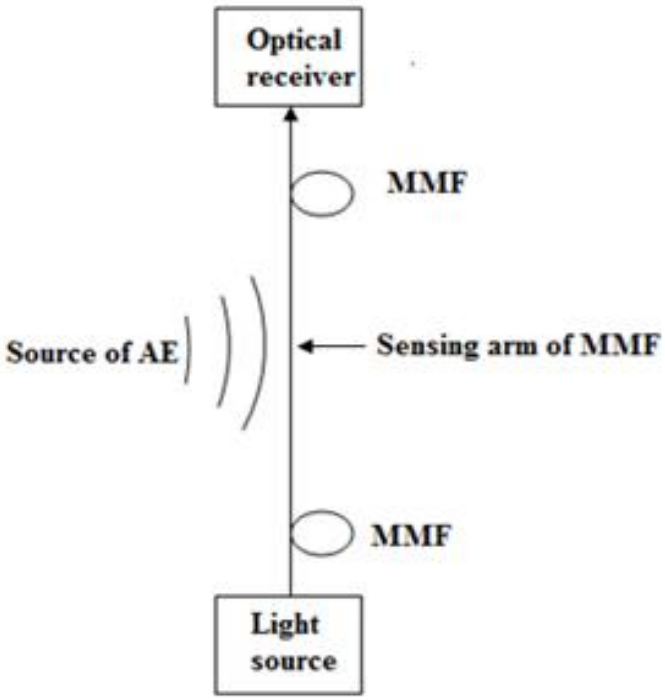

Figure 1. Diagram illustration of proposed multimode FO acting as AE sensor.

equipments remain in a degradation process during working and detection of partial discharge phenomena can predict its severe effect (Lamela-Rivera et al., 2003). It is important to save these costly equipments before failure by choosing a reliable diagnostic sensor to enhance the network reliability (Firoozi and Karami, 2011).

The PD produced AE phenomenon has gotten attention which emit electromagnetic emission as radio waves, light and heat waves. The energy produced by AE is in the audible and ultrasonic ranges and it can be used to detect the intensity and location of PD signal. In some previous studies, the frequency of PD in oil has been found in wideband range (10 to 500 kHz) (Frazao et al., 2010) which was detected by brand a broad band frequency piezoelectric (PZT) ultrasound sensor (model No. SDT1-028K). The fiber optical (FO) sensor has applications in many fields, and also can translate numerous measurands such as pressure, strain, temperature and AE into modulated light. AE are pressure variation in elastic medium (Posada-Roman et al., 2012) also known as stress wave emission. The conventional AE monitoring system was used as PZT sensor. The disadvantage of PZT sensor is low heat resistance due to the curie temperature of PZT, heavy monitoring system for multi-channel monitoring (Cho et al., 2006). Nowadays, AE is picked up by FO sensor due to some advantages such as small size, light weight, large wavelength, immunity to electromagnetic interference noise, low power consumption, high sensitivity and low cost. These advantages make FO sensor a good candidate for acoustic detection as compared with conventional acoustic sensor.

FO sensor can be classified as intrinsic or extrinsic. In intrinsic FO sensor, the optical signal does not leave the fiber optical while extrinsic FO sensor carries light to and from an external optical device. Recently, optical fiber has been used as single-mode intrinsic FO sensor based on interferometer measurement of AE inside insulation oil (Zhiqiang et al., 2000; Macià et al., 2003). The main advantage of single-mode FO sensor is that it has high sensitivity when using long fiber in sensing arm, its drawback is that the frequency response is not much high. In this work, AE induced by optical breakdown and PD using multimode intrinsic FO sensor and PZT sensor and assessment of the condition of high voltage equipment insulation in insulation oil were monitored. The data of both sensors were analyzed for comparative study which have been discussed in the results.

Principle of sensing

The simple optical AE detecting system consists of multimode optical fiber MMF linking light source and photo detector was adopted from the literature (Papy et al., 2003; Rippert et al., 2002). The complete strategy of AE detection is shown in Figure 1. This manuscript

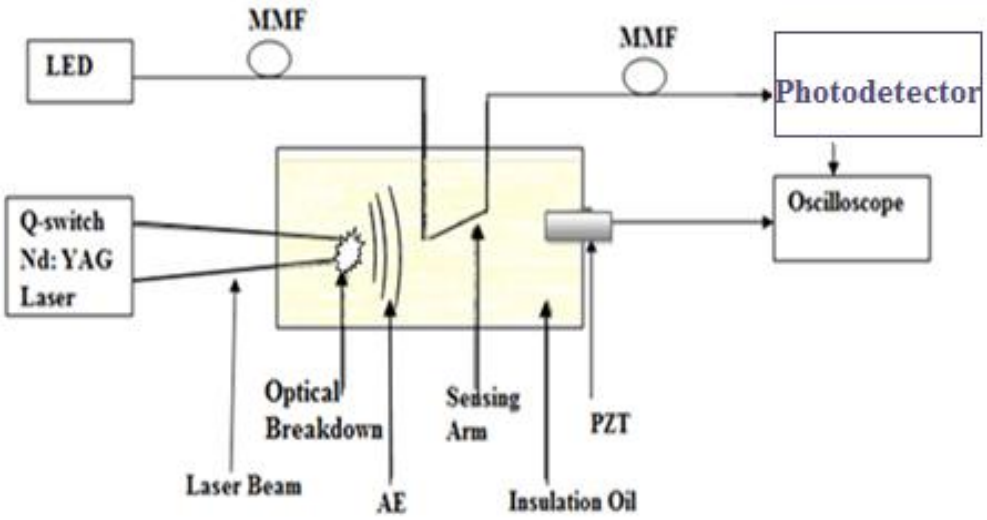

Figure 2. Experimental setup of FO and PZT sensors dipped in an oil tank.

describes a scheme for capturing partial discharge by multimode optical fiber in insulation oil. In the scheme, acoustic emission (AE) is induced by a neodymium-doped yttrium aluminum garnet; Nd:Y3Al5O12 (Nd:YAG) laser optical breakdown. The strong power density of laser plume approximately 6 × 1010 Wcm^{-2} at the focal point is responsible to ionize the medium in plasma formation which is associated with a shock wave phenomenon. This shock wave propagation generates acoustic sound in the interacting medium and it disturbs the multimode mode fiber (MMF). In this experiment, two sensors consisting of multimode optical fiber and PZT sensor were used to capture AE induced by optical breakdown produced by Nd:YAG laser (1064 nm) in oil tank. The optical detection system consists of a light source 850 nm, optical receiver as photo detector (PD1) and MMF in which photo detector converts optical signal to electrical signal while MMF produces a link between light source and optical receiver unit.

The multimode mode fiber (MMF) is disturbed by AE and this induces the change in the refractive index of the MMF which causes polarization and phase shift of the laser beam. Phase modulation of the laser beam from MMF has to be converted into amplitude modulation, and only then the photo detector can read the effect of disturbances applied to the MMF. Therefore, it appears that the photo detector in the scheme might detect amplitude modulation of the laser beam due to some other effects. The change in refractive index is read according to the equation given (Bucaro and Hichman, 1979):

$$\text{Бn} = n2pe\ P/2E \quad (1)$$

Where Бn is change in refractive index, pe is effective photoelastic constant, P is applied pressure and E is Young's Modulus.

The change in refractive will produce a phase change given by relationship:

$$\text{БФ} = 2\pi\ \text{Бn}\ l/\lambda \quad (2)$$

Where l is interaction length, λ is optical wavelength, БФ is phase change and Бn is change in refractive index.

METHODOLOGY

Simulation of PD conditions

The schematic illustration of the experimental setup is described in Figure 2 in which light source consisting of a LED type OV-LS (850 nm) with output power 0.01 mW. The light is sent through MMF and the optical signal of light source is received by a photodetector (PD1) which is also connected with MMF by means of a fiber coupling adapter. The MMF is a graded index fiber with core diameter (50 µm) and its cladding diameter with acrylate coating layer is 125 µm. The acrylate material has narrow band pass sensitivity to an ultrasound of AE which can give good results in oil insulation. Both sensors FO and PZT sensors were dipped in an oil tank (20 × 15 × 10 cm) for the detection of AE in insulation oil. The distance of FO was 3 cm from the AE source (optical breakdown of laser) while the distance of PZT sensor was 4 cm. The AE was induced by optical breakdown of Nd:YAG laser having 600 V is the Xe lamp voltage and 55 mJ average energy of one pulse. The outputs of optical signal of light for both sensors were recorded by a digital oscilloscope (TDS 3052C Digital phosphor Oscilloscope (500 MHz) which is shown in Figure 3.

PD detection under insulation oil by two sensors FO and PZT

The schematic diagram of complete experimental setup to generate PD and its AE is described in Figure 9. The tank was filled with insulation oil so that the steel electrodes remain completely immersed in the middle of the tank. Two sensors, multimode optical fiber and PZT were mounted on the top with the same distance 8 cm from PD source. The optical fiber used is a multimode graded

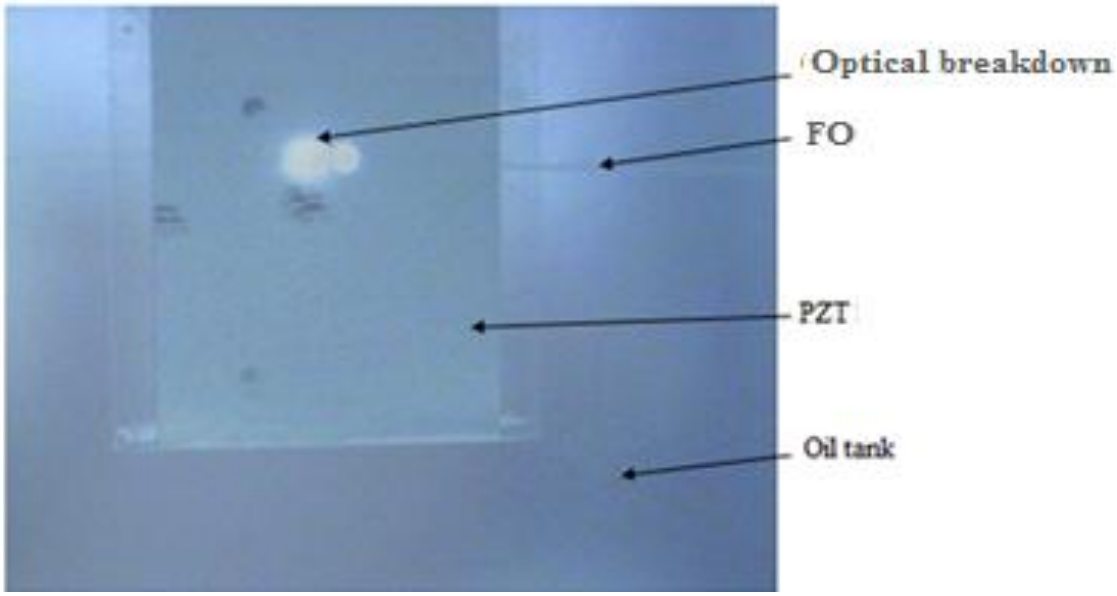

Figure 3. Image of optical breakdown along with FO and PZT sensor in an oil tank.

index fiber having core diameter of 50 µm. The cladding diameter of multimode fiber is 125 µm with coating layer plus soft coating such as acrylate based elastomers. Length of FO sensor inside oil tank was 6 cm. The electrodes having 5 mm gaps were connected to 2.5 kV high voltage source to produce PD under insulation oil. The acoustic emission produced by PD was then sensed by two sensors. The partial discharge generated an electromagnetic emission between two electrodes which created an interference in the light passing through the OF connected to the oscilloscope.

RESULTS AND DISCUSSION

Simulation of PD conditions

The graph of acoustic signals was detected by two acoustic sensors, FO and PZT sensors shown in Figure 4. The output of acoustic signals of both sensors in time domain analysis indicates that, the acoustic signal comprises of sinusoidal pulses with gradual decrease in intensity. Two acoustic signals have the same time period (1 µs) with voltage (5 mV) with frequency 180 kHz of AE generated by optical breakdown of laser, which is considered a perfect value for detection of AE (Lundgaard, 1992a; Lundgaard, 1992b; Kawada et al., 1984; Howells and Norton, 1981; Eleftherion, 1999). An analysis of detected acoustic signals depicted in Figure 4 dictates that both sensors are eligible to provide interesting information of acoustic signal induced by optical breakdown of Nd: YAG laser in oil. A typical shape of acoustic signal of both sensors is shown in Figure 5 which gives information of peak values of signals. The peak value of FO sensor has a high 0.015 V, while PZT sensor has a low peak signal of 0.002 V. It was also observed that acoustic signal of PZT sensor has a multi reflection due to degeneration of received signal while FO sensor has detected a clear acoustic signal.

In frequency domain analysis, Figures 6 to 8 shows the fast fourier transform (FFT) analysis of stored data of time domain signals of photodetector which was performed for both sensors. Figure 6 shows FFT of amplitude spectrum of both sensors (a) spectrum of FO sensor (b) spectrum of PZT sensor. Figure 6(a) shows acoustic wave of FO sensor with range (10 to 450 kHz); it can observe the frequency response of FO sensor consisting of a series of peaks which have maximum amplitude (0.1 mV/Hz) at frequency 180 kHz while PZT sensor has one peak which has maximum amplitude (0.4 mV/Hz) at frequency 180 kHz. Figure 7 shows the histogram of amplitude with the distance of FO sensor. It was observed that FO sensor has higher amplitude at distance (3 cm) between AE source and FO sensor.

Figure 8(a and b) show FFT spectrum of both sensors in oil. Figure 8(a) shows frequency response of FO sensor, which shows that the level of signal at 180 kHz was -20 dB with noise floor -55 dB which shows FO sensor has a resolution of 35 dB above noise floor. Figure 8(b) shows FFT spectrum of PZT, which has the signal level at 180 kHz was -35 db with noise level -50 dB, which has resolution 15 dB above noise floor. It is clear that the FO sensor has better resolution than PZT sensor.

PD detection under insulation oil by two sensors FO and PZT

The data of AE signal output of both sensors were

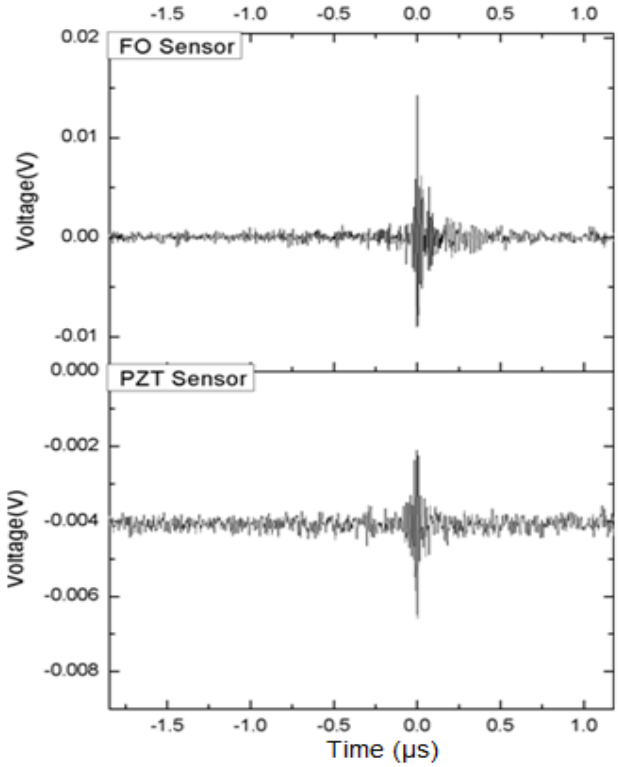

Figure 4. The graph of acoustic signal detected by FO and PZT sensors.

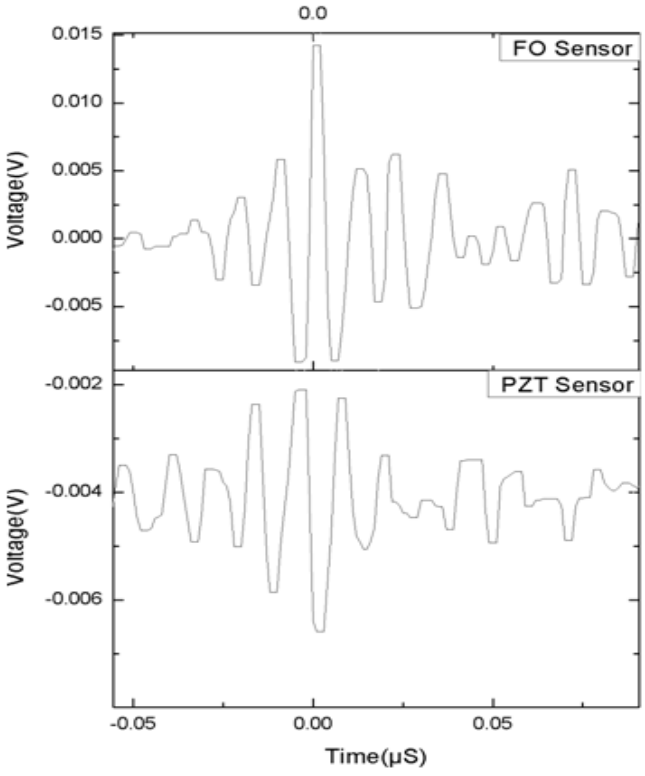

Figure 5. Typical shape of acoustic signal of FO and PZT sensors.

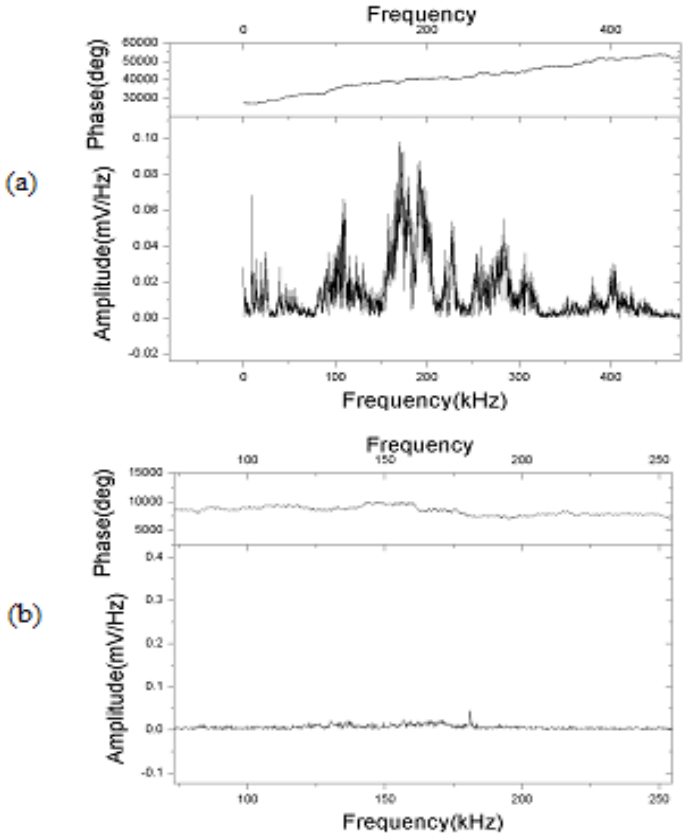

Figure 6. FFT spectrum of acoustic signal at frequency 180 kHz in oil (a) amplitude of FO sensor (b) amplitude of PZT sensor.

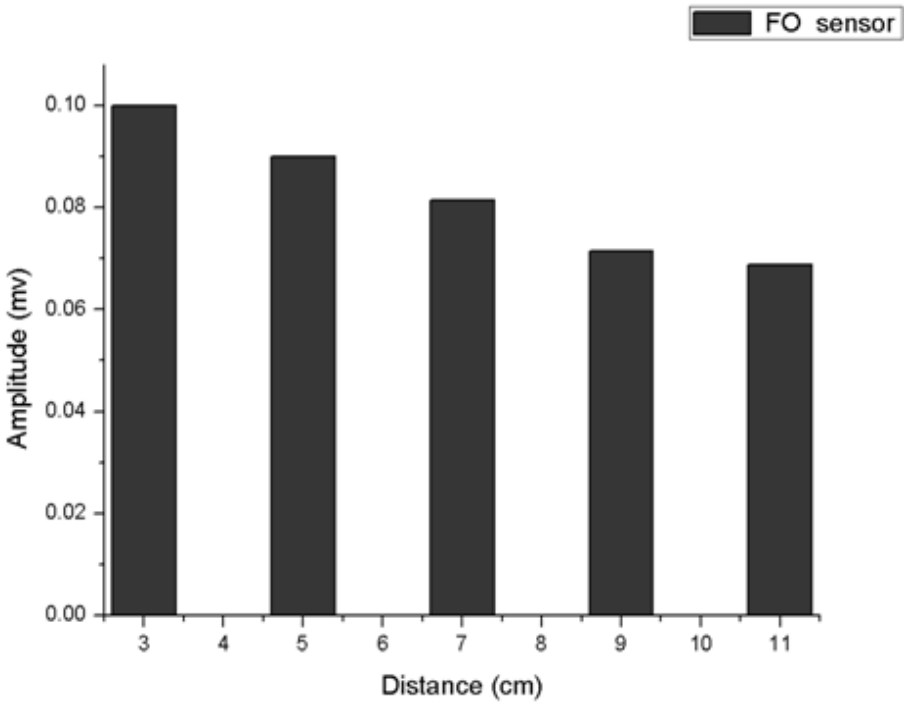

Figure 7. Histogram of amplitude with distance for FO sensor.

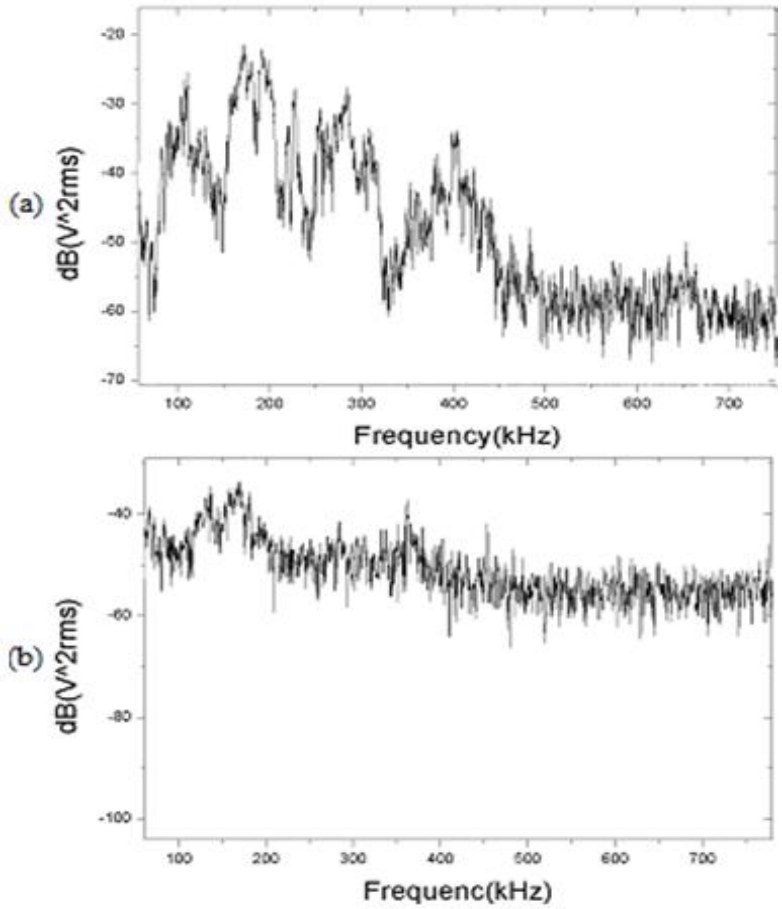

Figure 8. (a) Frequency response of FO. (b) Frequency response of PZT sensors in oil.

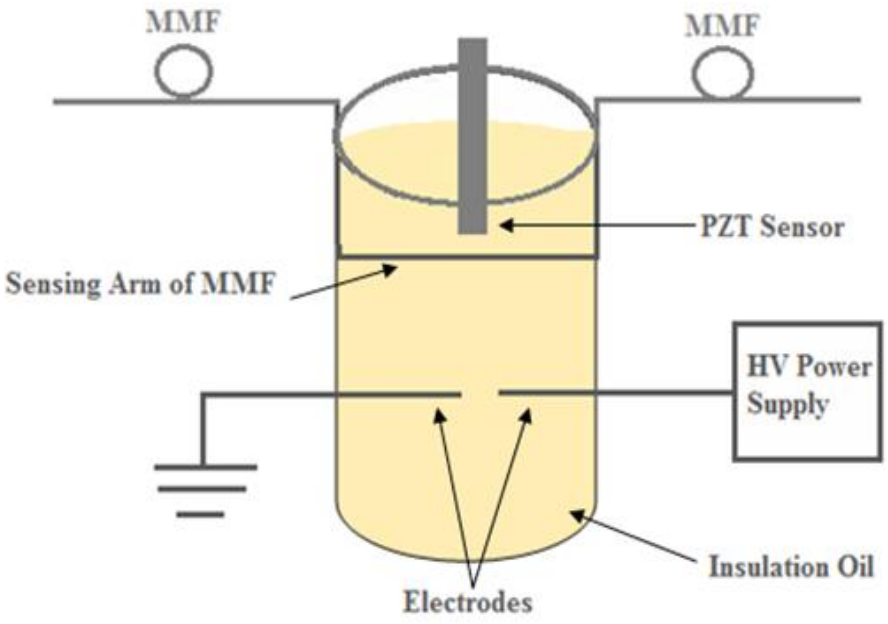

Figure 9. High voltage produced PD and AE signal insulation oil.

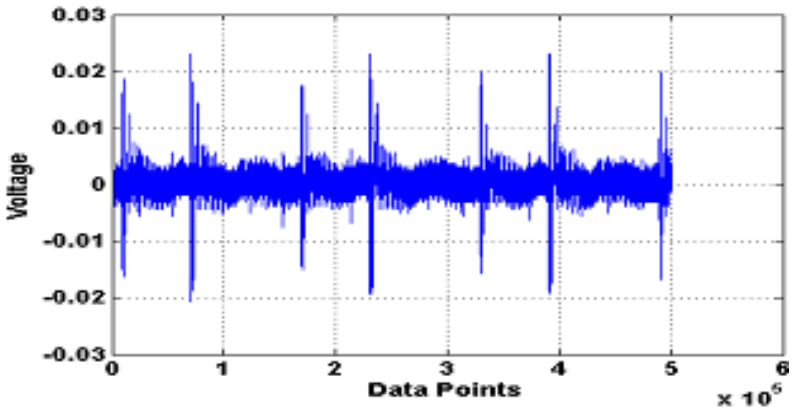

(a)

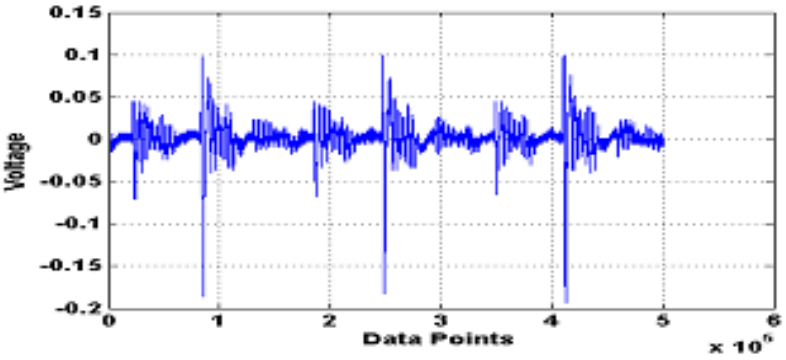

(b)

Figure 10. (a) The captured partial discharge signal from the piezoelectric sensor. (b) The captured partial discharge signal from the fibre optical sensor.

recorded by four channels digital Lecory oscilloscope. The typical spectra of acoustic signals detected by both sensors PZT and FOS are shown in Figure 10. These results show that acoustic signal generated by PD comprises sinusoidal pulses which have gradual decreasing trends in their intensity. Although, the shapes and peaks of the signal output of both sensors follow the same oscillatory pattern; it was also observed that PZT sensor has a noisy signal due to multi reflections which cause degeneration of the received signals. In case of PZT, it is difficult to determine exactly how long a PD will last while FOS gives a clear picture of acoustic wave.

WAVELET TRANSFORM ANALYSIS OF PD SIGNAL

The acoustic signals have some non-linear characteristics due to the PD and that make somewhat difficult to deal with because of nonlinear and the random like behavior of the system. The problem of non-linearity of the acoustic signal is overcome by using wavelet transform (WT) which is a strong tool for feature picking-up. It is equivalent to filters. Details (dn or hn) are produced by high pass filters and approximations (an or ln) are produced by low-pass filters. Due to the multidimensional characters which the wavelets possess, they are able to adjust their scale to the nature of the signal features (James, 1999). It can zoom in or zoom out the required details just like a microscope. Furthermore, wavelets can decompose a signal to give dilations and translations parameters, so the information in the signal is presented by these parameters in the form of frequencies. The Matlab wavelet toolbox is used to verify the algorithm where discrete wavelet transforms (DWT) is used to analyze the signals. The coefficients are generated and the features from the signal are extracted. Wavelet is a good tool to analyze the non-linear signals as it represents the features both in time and frequency domains (Ming and Birlasekaran, 2002; Gulski and Kreuger, 1992; Ma et al., 1992). The WT analyses the

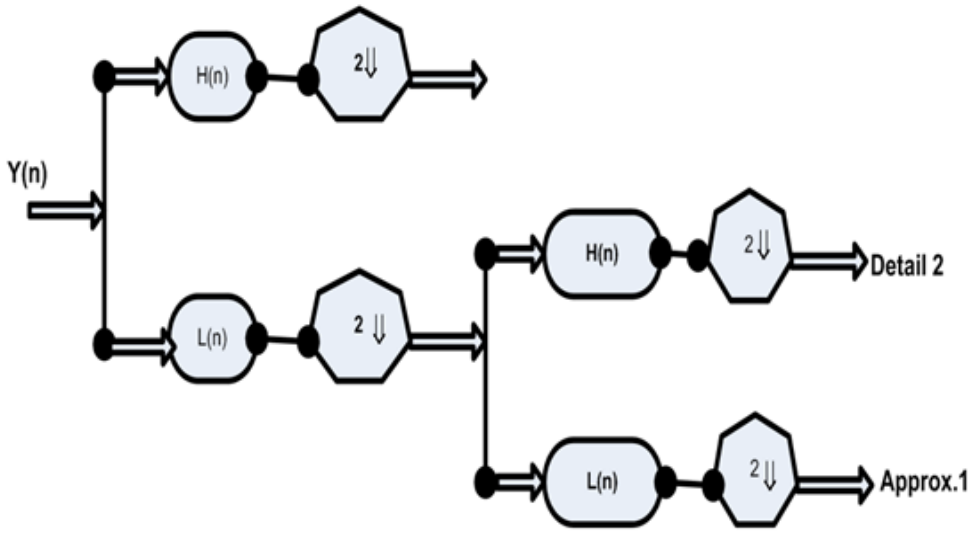

Figure 11. The filtering process in the DWT.

non-periodic partial discharge signal and adopts the principle of linking of frequency scales. Generally, the DWT is used for this mission (Suresh, 2005; Ma et al., 2005).

One of the capabilities of DWT is that, it produces details to show high frequency information and approximations to show low frequency information. The most suitable mother wavelet for detecting PD acoustic signals is the Daubichies (Db) wavelets transform, which is capable of detecting short duration, fast decaying, high frequency and low amplitude signals. The decomposition process in the WT consists of many numbers of filters from (Db2 to Db44), so the most promising number depends upon how they minimize the aliasing. Basically, in the first stage, the captured signal is divided into two of the frequency bandwidth, which is then passed to high pass and low pass filters (Lalitha anf Satish, 2000). After that, the output signal from the low pass filter is further subdivided into two of the frequency bandwidth and sent to the following stage (Geethanjali et al., 2005). This procedure continues until the predetermined number of levels is reached. The output of the final stage represents the same captured signal but at different frequency bands (Pihler et al., 1997; Mao and Aggarawal, 2000), which was realized in Figure 11. The suitable selection of mother wavelet depends on this application. Among the various de-noising techniques, from the point of view of the de-noising effect and the computing time, the DWT method is the most suitable. Finally, the Daubechies wavelet is most appropriate for treating PD (Zhou et al., 2006; Coifman et al., 1992).

In this study, the adaptability of the Daubechies wavelets of orders 2 has been evaluated, and results have shown its superiority. It is befitting to select a suitable number of breakup levels based on the nature of the signal. Based on acoustic signal features, it is seen that four levels of decomposition is the best choice, because it described the PD acoustic signal in a more mindful and symptomatic way. This decision is mainly due to the low frequency band (approximation), which is the most valuable part of the acoustic signal (Daubechies, 1992; Al-geelani, 2012). The detected signal due to the partial discharge using a piezoelectric sensor is shown in Figure 10(a) where the high spikes in addition to the background noise mixed-up with the PD signal can be seen. Thus, the Daubechies 2 wavelet transform has been used, at level 4 of decomposition for the wavelet analysis applied to the signals obtained in this analysis. Selection of mother wavelet is a core question often asked, but a generalized answer seems to be still elusive even to signal processing experts. Also, no direct answers are available in the literature. As per this fact, the present work was based on a trial-and error and guided by hints published in literature on similar types of work. Being well aware of this issue, the authors have examined many wavelets and found Daubechies' wavelet to be the most suitable. Thus, the wavelet technique has successfully de-noised the captured piezoelectric PD signal as can be seen in Figure 12(a) without compromising the unique feature of the signal which can be realized by the peaks and the values. This is the strength of wavelet analysis.

Figure10(b) shows the captured partial discharge signal using a fibre optical sensor, this signal is more accurate than the one detected using the piezoelectric sensor, since the amplitude is higher and very sharp in terms of peaks and valleys. The process of de-noising is shown in Figure 12(b) where the original signal or the captured partial discharge signal using the optical fibre and the de-noise signal are approximately the same, overlapping in a

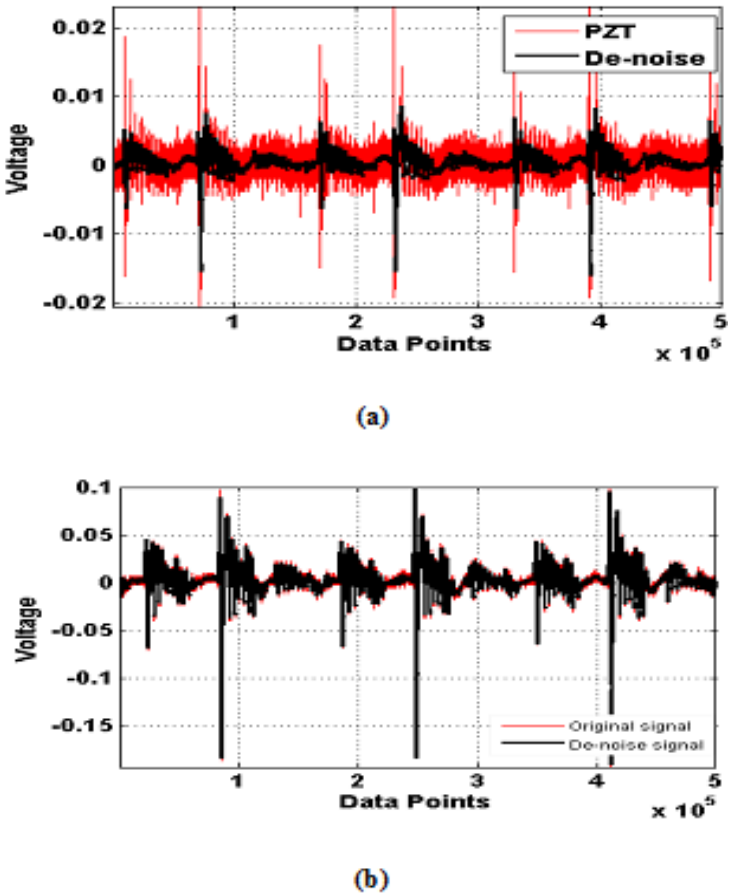

Figure 12. (a)The captured and the de-noise signal from the piezoelectric sensor. (b) The captured the de-noise partial discharge signal from the fibre optical sensor.

very good manner. This means that the signal detected by optical fibre cable is a noise free signal. Figure 13 shows that there is some similarity between the original and approximation (a1, a2, a3 and a4) signals more than details signals (d1, d2, d3 and d4). For the aforementioned reason, the approximation (a4) is a very good representation of the original signal. The levels of detail d1, d2, d3 and d4 contain useful higher frequency information. These subseries exhibit some regularities, similar shapes and compare mean values. Irregularities in those levels of detail are due to signal random variations and measurement errors. For the aforementioned reason, the approximation (a4) is a very good representation of the original signal. The most essential information can be found at this level. The accuracy of the approximation can be explained by the fact that there remains only a low-frequency signal corrupted by noises which was removed.

Figure 14 shows that As can be seen from the levels of approximations (a1, a2, a3 and a4) that no much difference occurred between the different levels; this is because the fiber optical sensor has detected the partial discharge signal with a very low level of noise. The details (d1, d2, d3 and d4) show the high frequency content where the level d4 is the best representation for the signal.

Conclusion

A comparative study of FO and PZT sensors for AE has successfully been done. The data of both sensors were analyzed in time and frequency domain. The time domain analysis showed that the acoustic signal of FO sensor has big peak signal (0.015 V), while peak signal of PZT was (0.002 V). The FO sensor could capture acoustic signal with less noise. The FFT analysis of time domain signal of store data of both sensors showed FO sensor within the range (10 to 450 kHz), it can be observed that the frequency response of FO sensor consisted of a series of peaks which have maximum amplitude (0.1 mV/Hz) at frequency 180 kHz whereas, PZT sensor has one peak which has maximum amplitude of 0.4 mV/Hz at frequency 180 kHz. This means that the amplitude of FO

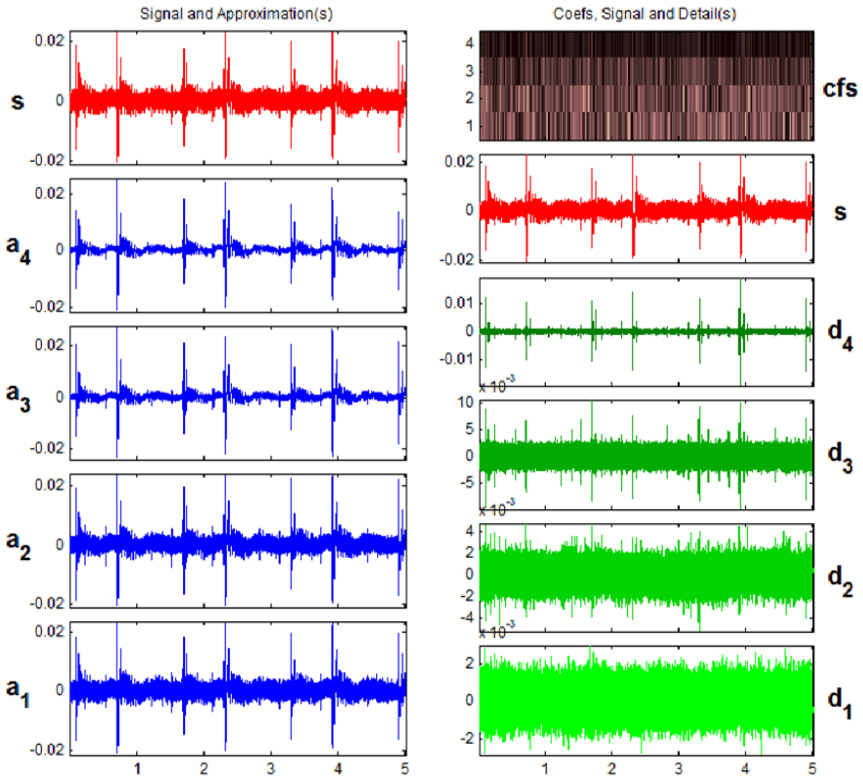

Figure 13. The 4 decomposition levels of DWT of the PZT PD signal.

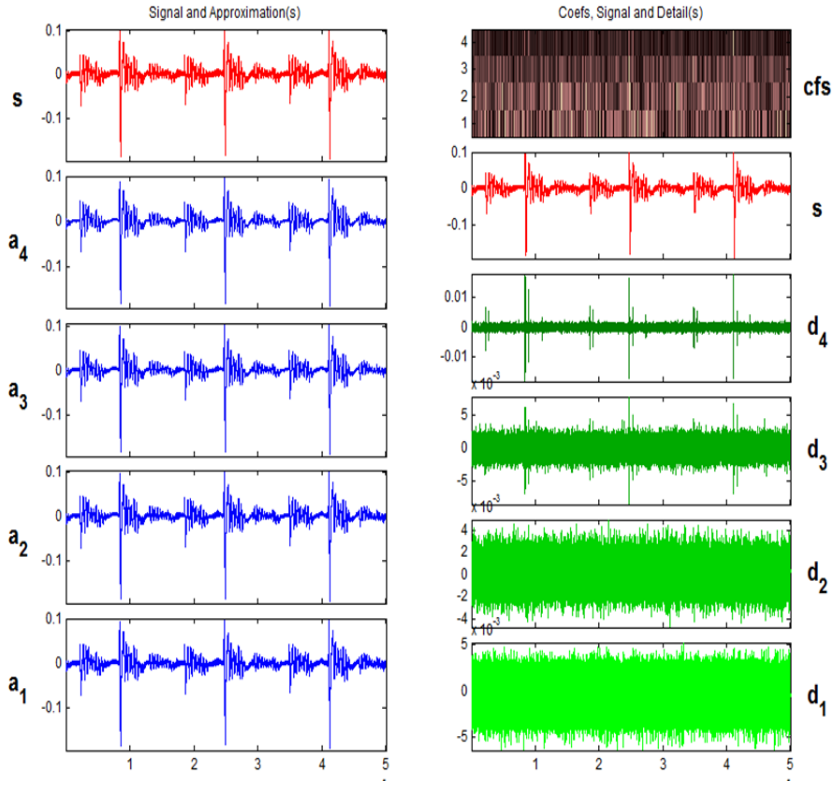

Figure 14. The 4 decomposition levels of DWT of the optical PD signal.

sensor is much higher than the PZT sensor. Also, FFT analysis showed a frequency response of FO and PZT sensors, which shows that FO sensor has signal level -20 dB at 180 kHz with noise floor -55 dB, while PZT sensor has signal level -35 dB at 180 kHz with noise floor -50 dB. It is clear that the resolution of FO sensor was very high (35 dB) above noise floor as compared with resolution of PZT sensor (15 dB) above noise floor. These experimental results are interesting and suggest that both sensors have peculiar characteristics for the detection of AE and can be used for any PD detection requirements. Wavelet analysis of PD signals shows that the signal detected by optical fibre cable is a noise free signal.

ACKNOWLEDGEMENTS

The authors would like to thank the administration of FKE (IVAT) and Advanced Photonic Science Institute, Universiti Teknologi Malaysia for encouragement and generous support.

REFERENCES

Boffi P, Bratovich R, Persia F, Martinelli M (2006). 1550nm All- Fiber Interferometer for Partial Discharge Detection in –Insulation power transformer. Paper presented at OSA international conference on optical fiber sensor, Cancún, Mexico, 23 October, pp. 1-3.

Bucaro JA, Hichman TR (1979). Measurement of sensitivity of optical fibers for acoustic detection. Appl. Opt. 18:938.

Cho H, Narus, T, Matsuo T, Takemoto M (2006). development of novel optical fiber AE sensor with multi-sensing function. Eng. Mater. 321(323):71-76.

Coifman PR, Wichkerhauser MV (1992). Entropy-based algorithms for best basis selection. IEEE Trans. Inf. Theory 38:719-746.

Daubechies I (1992). Ten Lectures on Wavelets, Society for Industrial and Applied Mathematics, Philadelphia. pp. 1-366.

Eleftherion PM (1999). Partial discharge XXI: Acoustic emission-based PD source location in T 1999 analysis of acoustic emission caused by the partial discharge in the insulation oil. Proceedings of partial discharge liquids, jaban. IEEE Electr. Insul. Mag. 11:22-26.

Firoozi H, Karami S (2011). Experimental Attempts and Field Experiences to Fault Diagnosis of Power Transformers using FRA Technique. Inter. Rev. Electr. Eng. (IREE) 5:2221-2228.

Frazao O, Farias RG, Araujo FM, Santos JL, Miranda V (2010). Manderel-based fiber-optic sensors for acoustic detection of partial discharge-proof of concept. IEEE Trans. Power App. Syst. 25:2526-2534.

Geethanjali M, Mary, Slochanal SR, Bhavani R (2005). A Novel Approach for Power Transformer Protection based upon combined Wavelet Transform and Neural Networks (WNN), Proceedings of International Power Engineering Conference, Department of Electrical Electronics Engineering. Thiagarajar Coll. Eng. Madurai pp. 1-1576.

Gulski E, Kreuger FH (1992). Computer-aided recognition of discharge sources. IEEE T. Power App. Syst. 27:82-92.

Howells E, Norton ET (1981). Location of partial discharge sites in on-linetransformers. IEEE T. Power App. Syst. 100(1):57.

James (1999). A Primer on wavelets and their Scientific Applications. 2nd ed, Walker University of Wisconsin Eau Claire.

Kawada H, Honda M, Inoue T, Amemiya T (1984). Partial discharge automatic monitor for oil- lled power transformer. IEEE T. Power App. Syst. 103(3):422-28.

Lalitha EM, Satish L (2000), Wavelet Analysis for Classification of Multi-Source PD Patterns, IEEE T. Dielectr. Electr. Insul. 7:40-47.

Lamela-Rivera H. Macia-Sanahuja C, Garcia-Souto J (2003). A Detection and wavelet analysis of partial discharge using an optical fiber interferometric sensor for high-power transformers. J. Opt. A Pure Appl. 5:66-72.

Lundgaard LE (1992a). Partial discharge—part XIII: acoustic partial discharge detection—fundamental considerations. IEEE Electr. Insul. Mag. 8(4):25–31.

Lundgaard LE (1992b). Partial discharge—part XIV: acoustic partial discharge detection practical application. IEEE Electr. Insul. Mag. 8(5):34.

Ma X, Zhou C, Kemp IJ (1992). Interpretation of Wavelet Analysis and its Application in Partial Discharge Detection. IEEE Trans. Dielectr. Electr. Insul. 9: 446-457.

Macià C, Lamela Rivera H, Garcia-souto JA (2003). Detection and wavelet analysis of partial discharges using an optical fibre interferometric sensor for high-power transformers. J. Opt. A. 5:66-72.

Mao PL, Aggarawal RK (2000). A wavelet transform based decision making logic method for discrimination between internal faults and inrush currents in power transformers. Int. J. Electr. Power Energ. Syst. 22:389-395.

Ming Y, Birlasekaran S (2002). Characterization of Partial Discharge Signals Using Wavelet and Statistical Techniques. Proceedings of International Symposium on Electrical Insulation, Sch. Electr. Electron. Eng. Nanyang Technol. Univ. pp. 9-13.

Al-geelani NA (2012). Characterization of acoustic signals due to surface discharges on H.V. glass insulators using wavelet radial basis function neural networks. Appl. Soft Comput. 12:1239-1246.

Papy JM, Van Huffel S, Rippert L, Wevers M (2003). On-line detection method for transient waves applied to continuous health monitoring of carbon fiber reinforced polymer composites with embedded optical fibers. Paper presented at SPIE's 10th Annual International Symposium on Smart Structures and Materials: Modeling, signal processing and control (SSM2003), vol. 5049 (ed. Ralph C. Smith, SPIE, Bellingham, WA) San Diego, California, USA, 2-6 March, pp. 718-731.

Pihler J, Grcar B, Dolinar D (1997). Improved operation of power transformer protection using ANN, IEEE T. Power Deliv. 12:1128-1136.

Posada-Roman J, Jose A, Souto G, Rubio-Serrano J (2012). Fiber optical sensor for acoustic detection of partial discharge in oil-paper insulated electrical system. Sensory 12(4):4793-4802.

Rippert L, Papy JM, Wevers M, Van Huffel S (2002). Fibre optic sensor for continuous health monitoring in CFRP composite materials. Paper presented at SPIE International Symposium on Smart Structures and Materials 2002: Modeling, Signal Processing and Control (SPIE SSM2002), San Diego, California, Mar. pp. 312-323.

Suresh D (2005). Feature Extraction for Multi Source Partial Discharge Pattern Recognition. Proceedings of the IEEE Indicon Conference, Anna University, Chennai. pp. 309-312.

Zhiqiang Z, Macalpine M, Demokan MS (2000). The directionality of an optical fiber high-frequencyacoustic sensor for partial discharge detection and location. J. Lightwave Technol. 18:795-806.

Zhou X, Zhou C, Stewart BG (2006). Comparisons of Discrete Wavelet Transform, Wavelet Packet Transform and Stationary Wavelet Transform in De-noising PD Measurement Data, Proceedings of the International Symposium on Electrical Insulation, School of Engineering, Science Design, Glasgow Caledonian Univ. pp. 237-240.

academicJournals

Vol. 8(21), pp. 1161-1165, 9 June, 2013
DOI: 10.5897/IJPS2013.3938
ISSN 1992-1950 © 2013 Academic Journals
http://www.academicjournals.org/IJPS

International Journal of Physical Sciences

Full Length Research Paper

Effect of fiber size on elastic constants of hybrid elliptical fiber reinforced lamina

V. Srinivasa Sai[1], V. Bala Krishna Murthy[2]*, M. R. S. Satyanarayana[3] and G. Sambasiva Rao[2]

[1]Department of Mechanical Engineering, DVR and Dr. HS MIC College of Technology, Kanchakacharla, A.P. India.
[2]Department of Mechanical Engineering V. R. Siddhartha Engineering College, Vijayawada, A.P. India.
[3]Department of Mechanical Engineering, GITAM University, Visakhapatnam, A. P. India

Accepted 3 June, 2013

Micromechanical analysis of an fiber reinforced polymer (FRP) lamina consisting of unequal sizes of unidirectional continuous elliptical fibers of two different materials arranged in hexagonal pattern is the present subject. The objective is to observe the change in Young's modulii and Poisson's ratios due to change in volume fractions and ellipse aspect ratio 'a' of individual fibers in a Representative Volume Element (RVE) without altering the total reinforcement share. A three-dimensional finite element model is developed and solved. Two different fiber materials (T-300 and S-Glass) are embedded in hexagonal pattern in a polymer matrix. The problem is simulated in ANSYS software. The converged results are validated using rule of mixtures which works exactly for longitudinal Young's modulus. It is observed that the longitudinal Young's modulus increases with increase in volume fraction of T-300 fiber and does not change due to 'a'. The transverse modulii decrease with increase in size of T-300 fiber and affected by variation of 'a'. Increasing in 'a' increases E_2 and decreases E_3.

Key words: Hybrid, fiber reinforced polymer (FRP), finite element method (FEM), micromechanics, elliptical fiber.

INTRODUCTION

The mechanical properties of an fiber reinforced polymer (FRP) composite depend upon fiber material, its size, shape and arrangement in matrix. Authors of this present work intend to obtain a wide range of mechanical properties of a unidirectional continuous fiber reinforced composite lamina by selecting two different fibers of elliptical cross-section arranged in hexagonal pattern with a provision to change ellipse aspect ratio and size of individual fibers. The brief review of literature relevant to the present topic is presented in the following paragraphs.

Noteworthy works of earlier researchers Eshelby (1957), Hashin (1962), Hill (1963, 1965), Hashin and Shtrikman (1963a) and Hashin and Rosen (1964). Hashin and Shtrikman (1963b) used variational principles to obtain upper and lower bounds for the effective elastic modulii as well as the effective electrical and thermal conductivities of multiphase composites with quasi-isotropic global characteristics. Later on, Milton (1981, 1982) obtained higher-order bounds for the elastic, electromagnetic, and transport properties of two-component macroscopically homogenous and isotropic composites given the properties of the individual constituents. More recently, Drugan and Willis (1996) and Drugan (2003), employed the Hashin–Shtrikman variational principles to analyze two-phase composites with random microstructure. A numerical implementation of this work was carried out by Segurado and Llorca

*Corresponding author. E-mail: vbkmpublications@yahoo.com.

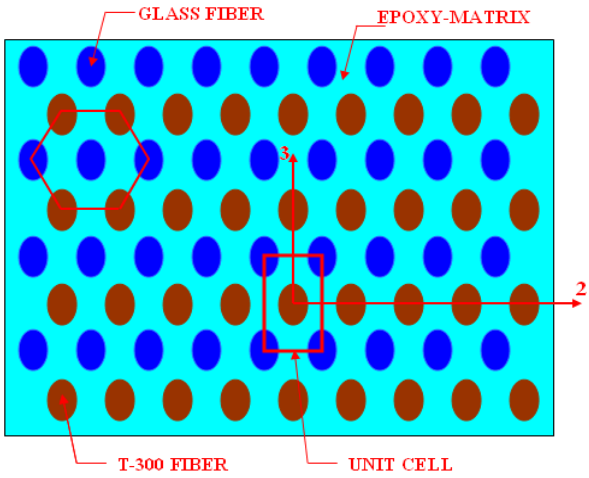

Figure 1. Hybrid composite lamina.

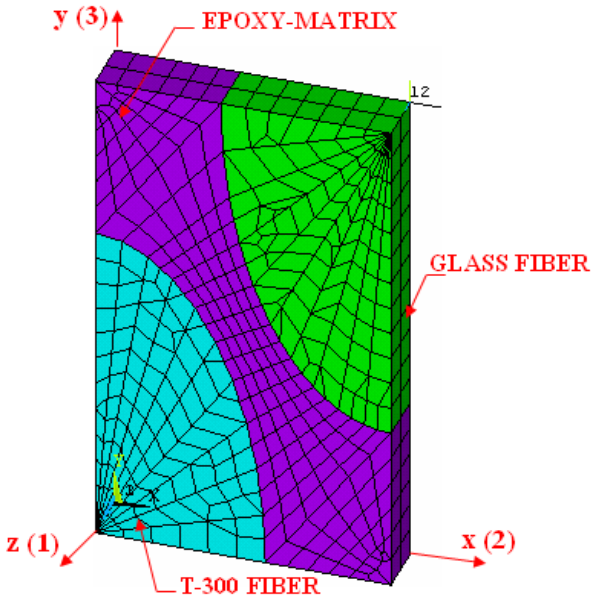

Figure 2. FE mesh on one-eighth portion of the unit cell (one quarter in cross section and half in length direction).

(2002). Other significant early results can be found in the work of Budiansky (1965) and Russel (1973). Mori and Tanaka (1973) in their micromechanical approach obtained closed-form expressions for the elastic properties of two-phase composites. Ying and Kin (2002) proposed a simple life prediction model for the hybrid composite.

Most recently Srinivasa Sai et al. (2010, 2011, 2012, 2013a and b) performed micromechanical analysis of hybrid elliptical fiber reinforced composite for the prediction of elastic properties and fiber-matrix interface stresses. The effects of fiber volume fraction and ellipse aspect ratio on the behaviour of hybrid lamina were studied. The present research work is the extension of Srinivasa Sai et al. (2013b) to study the effect of individual fiber volume fractions on Young's modulii and Poisson's ratios of hybrid composite for a constant total fiber percentage of 50.

METHODOLOGY

Hexagonal array of unit cells

Hexagonal arrangement of elliptical fibers of two different materials in alternative rows in a matrix is shown in Figure 1. It is assumed that the fiber and matrix materials are linearly elastic. A unit cell is adopted for the analysis. The fiber volume fraction V_f is calculated as the cross-sectional area of the fibers relative to the total cross sectional area of the unit cell since third dimension is same for all constituents for the unidirectional continuous fiber reinforced composite. A material coordinate system 1-2-3 is assigned as shown in Figure 1 for the analysis of the problem. 1) is the longitudinal direction of the fiber, 2) the in-plane transverse direction and 3) through-thickness or out-of-plane transverse direction.

Finite element model

One-eighth portion of the unit cell (that is, one quarter in the cross section and one-half in the longitudinal direction of the fiber) is modeled by taking the advantage of symmetry in geometry, material and loading (Figure 2). The element named SOLID 95 in ANSYS software is used for finite element generation. This is a quadratic brick element having 20 nodes with 3- degrees of freedom (linear displacement components) at each node. This element uses three-dimensional elasticity theory while preparing element matrices. The dimensions of FE model are taken as 50, 86.6 and 10 units in x- y- and z- directions respectively. The dimensions of ellipse are obtained according to the fiber volume fraction and the ellipse aspect ratio ('a'= axis length in 3-direction by axis length in 2-direction).

Boundary conditions and loading

Three perpendicular planes on negative side of coordinate axes are constrained to restrict displacement in normal directions. The opposite faces are constrained to have uniform normal displacement. A uni-axial external load is applied once at a time with respect to the assigned material coordinates in order to use simple Hooke's law to determine Young's modulii. Corresponding Poisson's ratios are also calculated.

Materials

One of the fibers that is, T-300 is orthotropic and other S-Glass fiber and matrix materials are isotropic. The mechanical properties of the constituent materials used in the present analysis are given in Table 1.

RESULTS

The finite element software ANSYS is successfully executed for the analysis. The elastic properties are

Table 1. Mechanical properties of the constituent materials.

Property	T-300 fiber	S-Glass fiber	HM polymer matrix
E_1 (GPa)	220.60	85.50	5.17
E_2 (GPa)	13.79	85.50	5.17
E_3 (GPa)	13.79	85.50	5.17
v_{12}	0.20	0.20	0.35
v_{23}	0.25	0.20	0.35
v_{13}	0.20	0.20	0.35
G_{12} (GPa)	8.96	35.62	1.91
G_{23} (GPa)	4.83	35.62	1.91
G_{13} (GPa)	8.96	35.62	1.91

Table 2. Validation of E_1 (MPa).

$V_{f1} + V_{f2}$	ROM	FEM	% Variation
5+45	52090	52129	0.076
10+40	58845	58884	0.067
15+35	65600	65640	0.061
20+30	72355	72396	0.056
25+25	79110	79150	0.051
35+15	85865	85905	0.046
40+10	92620	92660	0.043
45+5	99375	99413	0.039

evaluated using the normal strains in 1, 2 and 3 directions calculated from the normal deformations of the unit cell obtained from finite element analysis. The displacements in x, y and z directions, U_x, U_y and U_z respectively of the finite element model are obtained from the finite element solutions. The corresponding normal strains are determined from the displacements. The longitudinal Young's moduli and Poisson's ratios due to the longitudinal load are determined from the following expressions.

$$E_1=\sigma_1/\varepsilon_1 \quad v_{12}= - \varepsilon_2/ \varepsilon_1 \quad v_{13}= - \varepsilon_3/ \varepsilon_1$$

where 1(z), 2(x) and 3(y) are longitudinal, in-plane transverse and out-of-plane transverse directions respectively of the composite lamina. Remaining properties are obtained in similar fashion for in-plane and out-of-plane transverse loads. The results are obtained for hybrid lamina with varying volume fractions of individual fibers for a total fiber volume fraction of 50%.

Validation

The converged finite element results are validated for the longitudinal Young's modulus using rule of mixtures (ROM) which is an exact theoretical approach for unidirectional continuous fiber composites. The results are presented in Table 2 for various arrangements of fibers for 'a'=0.5. V_{f1} and V_{f2} are the volume fractions of T-300 and S-Glass fibers respectively. A very close agreement is observed between the FE and analytical results.

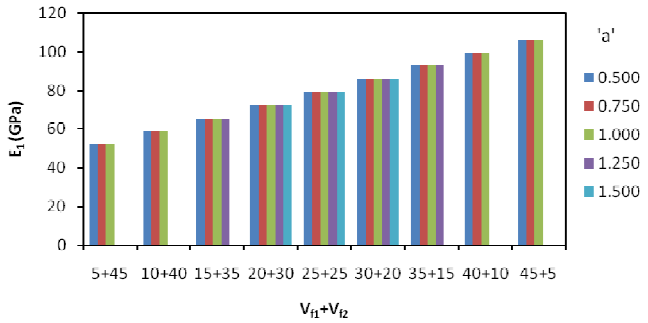

Figure 3. Variation of E_1 with respect to varying fiber volume fractions for different 'a'.

Analysis

It can be observed that E_1 linearly increases with respect to change in individual fiber volume fractions but not affected by 'a' (Figure 3). Which is expected since rule of mixtures does not take shape of fiber into account. v_{12} decreases and v_{13} increases with 'a' at larger rate for lower volume fractions of T-300 fiber and at smaller rate for smaller volume fractions of S-Glass fiber as shown in Figures 4 and 5. At 'a'=0.5 there is no considerable variation in these Poisson's ratios with respect to change in V_f of fibers. However, v_{12} increases up to certain extent followed by a slight drop for other values of 'a', whereas v_{13} variation is opposite to that of v_{12}.

Figures 6 and 7 show the variation of E_2 and E_3 respectively. E_2 and E_3 decease with increasing in size of T-300 fiber and decrease of S-Glass fiber. This is obvious since stiffness of glass fiber is greater than transverse stiffness of T-300 fiber. E_2 increases and E_3 decreases with 'a' at larger rate for small volume of T-300 fiber. Increase in 'a' increases reinforcement effect in 2-direction and decreases in 3- direction due to increase in projected area of ellipse normal to 2-direction. Figures 8 and 9 show the variation of Poisson's ratios v_{21} and v_{31}. These properties decrease with volume fraction changes. With respect to 'a', v_{21} increases at smaller volume fractions of T-300 fiber. At other places and for all values of 'a' these piosson's ratios are not changing

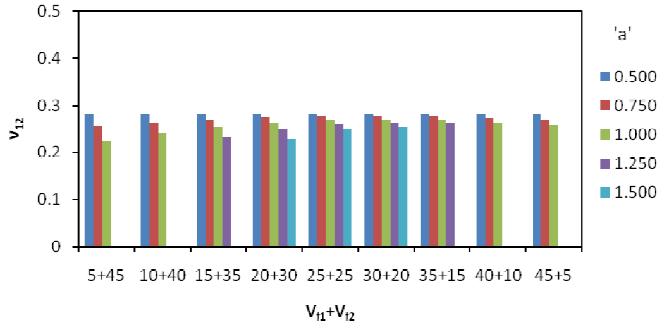

Figure 4. Variation of v_{12} with respect to varying fiber volume fractions for different 'a'.

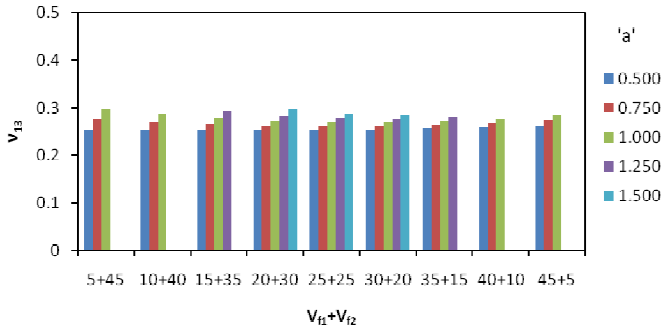

Figure 5. Variation of v_{13} with respect to varying fiber volume fractions for different 'a'.

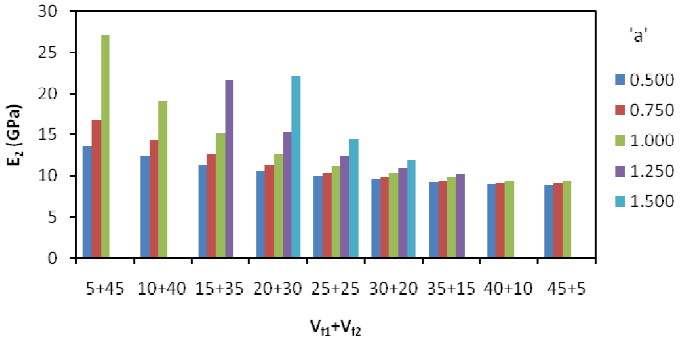

Figure 6. Variation of E_2 with respect to varying fiber volume fractions for different 'a'.

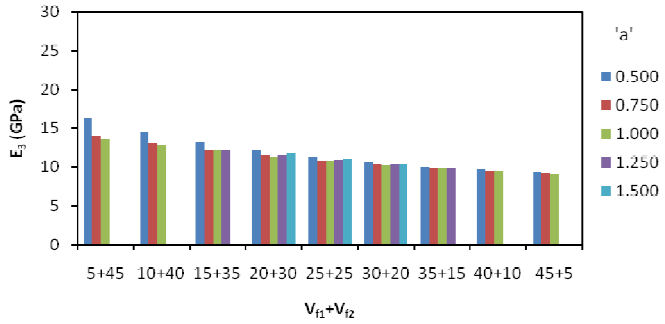

Figure 7. Variation of E_3 with respect to varying fiber volume fractions for different 'a'.

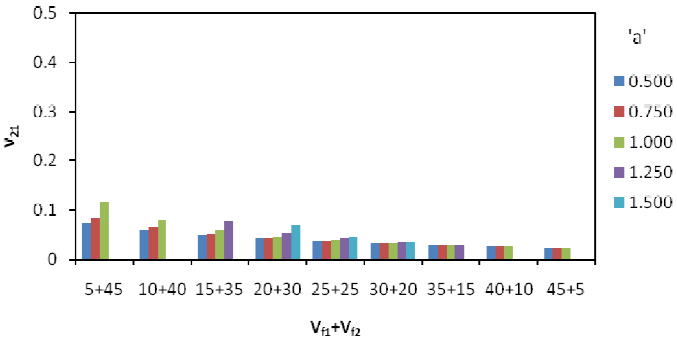

Figure 8. Variation of v_{21} with respect to varying fiber volume fractions for different 'a'.

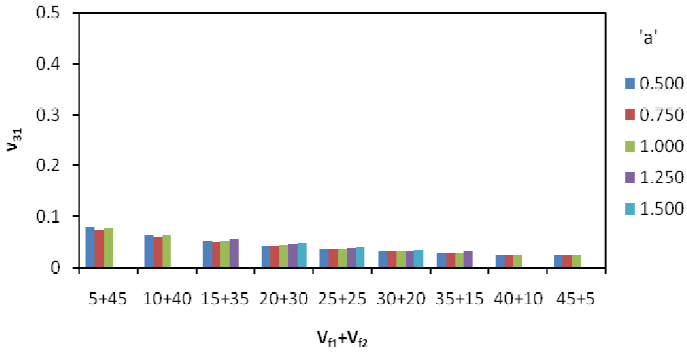

Figure 9. Variation of v_{31} with respect to varying fiber volume fractions for different 'a'.

considerably. Figures 10 and 11 show the variation of Poisson's ratios v_{23} and v_{32}. These properties increases up to certain extent and decreases with respect to fiber volume fraction changes. v_{23} increases with 'a' at lower volumes of T-300 fiber followed by negligible changes, whereas v_{32} decreases with 'a'. The reasons for the variation of Poisson's ratios are similar to that explained for variation of Young's modulii since the strains are taken from the same load cases.

Conclusions

Young's modulii and Poisson's ratios are predicted for an elliptical hybrid fiber reinforced composite lamina using three-dimensional finite element analysis. The effect of change in volume fractions of individual fibers and fiber cross-sectional aspect ratio on these elastic properties is studied. It is observed that this study gives a scope to

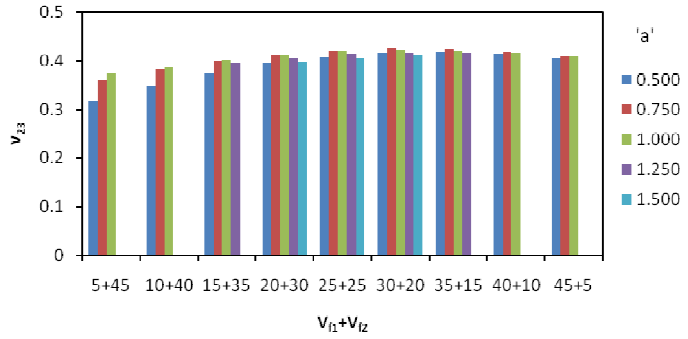

Figure 10. Variation of v_{23} with respect to varying fiber volume fractions for different 'a'.

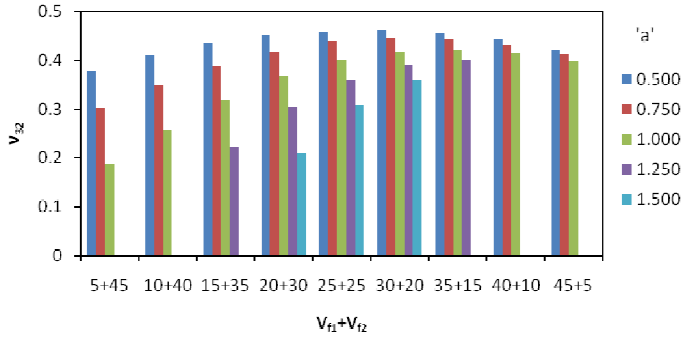

Figure 11. Variation of v_{32} with respect to varying fiber volume fractions for different 'a'.

obtain a wide range of elastic properties for selection of material as per design requirements.

REFERENCES

ANSYS Reference Manuals, 2008.

Budiansky B (1965). On the elastic modulii of some heterogeneous materials, J. Mech. Phys. Solids 13:223–227.

Drugan WJ, Willis JR (1996). A micromechanics-based non local constitutive equation and estimates of representative volume element size for elastic composites. J. Mech. Phys. Solids, 44(4):497–524.

Drugan WJ (2003). Two exact micromechanics-based non local constitutive equations for random linear elastic composite materials, J. Mech. Phys. Solids, 51(9):1745–1772.

Eshelby JD (1957). The determination of the elastic field of an ellipsoidal inclusion, and elated problems. Proc. Roy. Soc. A241:376–396.

Hashin Z (1962). The elastic moduli of heterogeneous materials, J. Appl. Mech, 29:143.

Hill R (1963). Elastic properties of reinforced solids, J. Mech. Phys. Solids, 11:357–372.

Hill R (1965). A self-consistent mechanics of composite materials, J. Mech. Phys. Solids, 13:213–222.

Hashin Z, Shtrikman S (1963a). A variational approach to the theory of elastic behavior of multiphase materials, J. Mech. Phys. Solids, 11:127–140.

Hashin Z, Shtrikman S (1963b). Conductivity of polycrystals, Phys. Rev. Lett.130(1):129–133.

Hashin Z, Rosen BW (1964). The elastic moduli of fiber-reinforced materials, J. Appl. Mech. 31:223–232.

Milton GW (1981). Bounds on the electromagnetic, elastic, and other properties of two- component composites, Phys. Rev. Lett. 46:542–545.

Milton GW (1982). Bounds on the elastic and transport properties of two-component composites, J. Mech. Phys. Solids, 30:177–191.

Mori T, Tanaka K (1973). Average stress in matrix and average energy of materials with misfitting inclusions, Acta Metall. Mater. 21:571–574.

Russel WB (1973). On the effective moduli of composite materials: effect of fiber length and geometry at dilute concentrations, Zei ang Math. und Physik, 24:581–600.

Segurado J, Lorca LJ (2002). A numerical approximation to the elastic properties of sphere-reinforced composites, J. Mech. Phys. Solids, 50(10):2107–2121.

Srinivasa Sai V, Bala Krishna Murthy V, Satyanarayana MRS, Sambasiva Rao G, Phani Prasanthi P (2010). Prediction of Micromechanical Behaviour of Hybrid Elliptical Fiber Einforced Lamina For Longitudinal Load, Int. J. Appl. Eng. Res. 5(2):293–304.

Srinivasa Sai V, Bala Krishna Murthy V, Satyanarayana MRS, Sambasiva Rao G (2011). Prediction of Micromechanical Properties of Hybrid Elliptical Fiber Reinforced Lamina, Int. Conf. Futuristic Trends Mater. Energy Syst. (FTME -2011) organized by Mechanical Engineering Department of V. R. Siddhartha Engineering College, Vijayawada, India, pp. 77-81.

Srinivasa Sai V, Bala Krishna Murthy V, Satyanarayana MRS, Sambasiva Rao G (2012). Prediction of Interfacial Stresses in a Hybrid Elliptical Fiber Reinforced Lamina Subjected to Out-of-Plane Transverse Load, Int. J. Eng. Res. Ind. Applications, 5(IV):71-81.

Srinivasa Sai V, Bala Krishna Murthy V, Satyanarayana MRS, Sambasiva Rao G (2013a). Prediction of Micromechanical Behaviour of Hybrid Elliptical Fiber Reinforced Lamina for In-Plane Transverse Load, Int. J. Math. Sci. Eng. Applications, 7(I):91-100.

Srinivasa Sai V, Bala Krishna Murthy V, Satyanarayana MRS, Sambasiva Rao G (2013b). Mechanical Properties of Hybrid Elliptical Fiber Reinforced Lamina with equal Fiber Volume Fractions, Int. J. Current Eng. Technol. 3(1):102-107.

Ying S, Kin L (2002). Environmental fatigue behavior and life prediction of unidirectional glass–carbon/epoxy hybrid composites, Int. J. Fatigue, 24:847–859.

academicJournals

Vol. 8(21), pp. 1166-1173, 9 June, 2013
DOI: 10.5897/IJPS2013.3921
ISSN 1992-1950 © 2013 Academic Journals
http://www.academicjournals.org/IJPS

International Journal of Physical Sciences

Full Length Research Paper

Impact of dust on the photovoltaic (PV) modules characteristics after an exposition year in Sahelian environment: The case of Senegal

Ababacar Ndiaye[1]*, Cheikh M. F. Kébé[1], Pape A. Ndiaye[1], Abdérafi Charki[2], Abdessamad Kobi[2] and Vincent Sambou[1]

[1]Centre International de Formation et de Recherche en Energie Solaire (CIFRES), Ecole Supérieure Polytechnique-UCAD, BP 5085 Dakar-Fann, Sénégal.
[2]Université d'Angers-ISTIA-LASQUO, 62 Avenue Notre Dame du Lac 49000 Angers, France.

Accepted 13 May, 2013

The objective of this paper is to find the effect of dust on the performance of photovoltaic modules. To this end, the International Center for Research and Training in solar energy at Dakar University and the Lasquo-ISTIA Laboratory of Angers University have put in place a research project in order to investigate the impact of Sahelian climatic conditions on the photovoltaic (PV) modules characteristics. Accordingly, monocrystalline silicon (mc-Si) PV module and a silicon polycrystalline (pc-Si) PV module are installed at Dakar University and monitored during one operation year without cleaning. We evaluate the variation depending on the dust of electrical characteristics such as I-V and P-V curves, open-circuit voltage (V_{oc}), short-circuit current (I_{sc}), maximum ouput current (I_{max}), maximum output voltage (V_{max}), maximum power output (P_{max}) and fill factor (FF). This work has highlighted the impact of dust on the Current-Voltage (I-V) and Power-Voltage (P-V) characteristics of PV modules (mc-Si and pc-Si) with the advent of the mismatch effect. P_{max}, I_{max}, I_{sc} and FF are the most affected performance characteristics by the dust deposits on the PV modules surface. The maximum power output (P_{max}) loss can be from 18 to 78% respectively for the polycrystalline module (pc-Si) and monocrystalline module (mc-si). I_{max} loss can vary from 23 to 80% for respectively pc-Si and mc-Si modules. However, the maximum voltage output (V_{max}) and the open-circuit voltage (V_{oc}) are not affected by dust accumulation for both technologies studied. The fill factor (FF) may decrease from 2% for the pc-Si module to 17% for the mc-Si module.

Key words: Photovoltaic module, photovoltaic (PV) module performance parameters, dust effect.

INTRODUCTION

Using the locally available renewable energy sources, especially solar irradiation which is of high availability all over the globe, offers a strategic solution for power supply problems. It is important to implement the photovoltaic system technology suitable for the relevant locations in order to take into consideration the local environment aspects and optimize the energy yield. However, one of the constraints of photovoltaic (PV) systems in the Sahelian areas is related to the dust deposition on the photovoltaic modules surface. The accumulation of dust particles on the surface of PV module greatly affects its performance especially in the

*Corresponding author. E-mail: ababacar.ndiay@gmail.com. Tel: +221 77 654 63 93. Fax: +221 33 823 55 74.

desert areas. But desert countries are of course best suited to photovoltaic power generation due to abundant availability of sunlight throughout the year. Nowadays the idea for setting up vast solar arrays in Sahelian countries and exporting the power to other countries are being discussed. In a bigger PV solar plants, more work force and machines will be needed to keep making the rounds and cleaning the panels, especially after a sand storm. The dust accumulation on the PV panel surface depends on different parameters like PV panel inclination, kind of installation (stand alone or on tracker), humidity etc. Many research results discuss about performance of panel with dust concentration on the surface. Hottel and Woertz were amongst the pioneers investigating the impact of dust on solar systems (Hottel and Woertz, 1942). They recorded a maximum degradation in collector performance of 4.7%, with an average loss in incident solar radiation being less than 1%. In a study (Salim et al., 1988) into dust accumulation on a solar-village PV system near Riyadh indicated a 32% reduction in performance after eight months. In Wakim (1981) is indicated a reduction in PV power by 17% due to sand accumulation on panels in Kuwait city after six days. Furthermore the study also indicated that the influence of dust on PV performance would be higher in spring and summer than in autumn and winter. In a different study on the effects of dust on solar PV panel in Palo Alto, California (Katz, 2011), it was reported that the dust on solar PV panels caused a 2% of current reduction relative to that for clean panels. In Shaharin (2011), the reduction in the peak power generated by the dust on the PV panel can be up to 18%. The power loss due to soiling is therefore a function of the type of dust, the length of time since the last rainfall and the cleaning schedule (Kymakis et al., 2009). In general, the standard industry assumption of soiling losses ranges from 1 to 4% on an annual basis (Detrick et al., 2005). In areas of frequent rainfall, it was demonstrated that the rain could clean the PV modules to an extent of restoring the performance to within 1% of full power (Hammond et al., 1997). Accordingly, in a more recent soiling analysis performed in Crete, with climatic conditions almost identical to Cyprus, the annual soiling loss was 5.86%, with the winter losses being 4 to 5 and 6 to 7% in the summer (Kymakis et al., 2009; Sharma and Bowden, 2012). A soiling investigation was carried out also for the systems installed in Egypt and specifically by comparing the energy produced by a clean module, a module that has been exposed to dust for a period of one year and a module that has been exposed to dust but cleaned every two months. The energy production results showed that the ‘one year dusty module’ produced 35% lower energy while the ‘two month dusty module’ produced 25% lower energy compared to the clean module (Ibrahim et al., 2009). In Catelani et al. (2012), it claimed that the dust lead to a decrease of the transmittance of solar cell glazing and cause a significant degradation of solar conversion efficiency of PV modules.

Same technology PV panel from different manufacturers suffers in completely different pattern. For a common PV user it is important to know how frequent the panel has to be cleaned. In case if the frequent cleaning is not feasible, it is important to know the performance loss due to dust for additional estimation to compensate the loss. The study on effect of dust on the PV panel will help to select panel technology for particular type of application and location. Thus, this work was initiated to study the influence of dust deposits on the electrical performance of photovoltaic modules in the long term (Zhou et al., 2007). Current-Voltage (I-V) and Power-Voltage (P-V) curves, open-circuit voltage (V_{oc}), short-circuit current (I_{sc}), fill factor (FF) and maximum power (P_{max}). The photovoltaic test fields at Dakar University in Senegal is shown in Figure 1. On this figure is shown the dust layer accumulated on the surface of PV modules after one exposition year without cleaning on the site of Dakar in Senegal.

MATERIALS AND METHODS

Presentation of photovoltaic test field

The photovoltaic platform shown in Figure 1 is used in this study. It is installed at the Higher Polytechnic School of the Dakar University, Senegal. Senegal is located on the extreme western Africa between 12.5° and 16.5° North latitude and 12° and 17° West longitude. It presents a dry tropical climate characterized by two seasons: A dry season from November to June and a rainy season from July to October (ANAMS, 2012). Senegal has a significant solar potential with annual average radiation duration of about 3000 h and an exposure rate of 5.7 kWh/m^2/day. This radiation varies between the northern part more sunlit (5.8 kWh/m^2/day in Dakar) and the southern part richest in terms of precipitation (4.3 kWh/m^2/day in Ziguinchor) (PSA, 2011). The temperature varies from 16°C around Dakar (January) to 38°C in the South (October). The rainfall increases from North to South with an annual average of 300 mm in the extreme North and 1500 mm in the extreme South (ANAMS, 2012). The relative humidity varies between 75 and 95% (Wofrance, 2012). The platform is installed in Dakar between 17.28° West longitude and 14.43° North latitude to 31 m altitude.

Platform has been made operational since one year. It consists of one monocrystalline (A) and one polycrystalline (B) photovoltaic modules. The technical characteristics of PV modules provided by the manufacturers are given in Table 1. The modules have operated during one year without being cleaned inducing the deposition of a dust layer on the modules surface as shown in Figure 1. Thus, in this state (one year from dust) performance parameters (I-V and P-V curves, V_{oc}, I_{sc}, FF and P_{max}) are measured under the standard test conditions (AM1.5, 1000 W/m^2, 25°C). Then the same process is repeated on the same properly cleaned (without any trace of dust on their surface) under the same standard conditions of test modules as previously. These measurements are made with the test instrument of PV modules known as "IV 400".

Presentation of measurement instrument "I-V 400"

"I-V 400" carries out the field measurement of the I-V characteristic and of the main characteristic parameters both of a single module and of module strings. The instrument measures, together with I-V characteristic of the device being tested, also the values of its

Figure 1. Photovoltaic test field at Dakar University in Senegal.

Table 1. Technical characteristics of PV modules.

Module	Technology	Manufacturer	Reference	Parameter	Value
A	Monocrystalline Silicon	Bosch	SP36-145M	Maximum output power (Pmax)	145 W
				Maximum output voltage (Vmax)	17.9 V
				Maximum output current (Imax)	8.1 A
				Open circuit voltage (Voc)	22.7 V
				Short-circuit current (Isc)	8.5 A
				Fill factor (FF)	75.14%
B	Polycrystalline Silicon	Aleo	S18-230	Maximum output power (Pmax)	230 W
				Maximum output voltage (Vmax)	29.2 V
				Maximum output current (Imax)	7.88 A
				Open circuit voltage (Voc)	36.6 V
				Short-circuit current (Isc)	8.44 A
				Fill factor (FF)	74.48%

temperature and incident irradiation. The acquired data are then processed to extrapolate the I-V characteristic at standard test conditions (STC) in order to proceed with the comparison with the nominal data declared by the modules manufacturer, thus immediately determining whether or not the string or the module being tested respects the characteristics declared by the manufacturer. Output current or voltage from the module is measured with the 4-terminal method, which allows extending the measurement cables without requiring any compensation for their resistance, thus always providing accurate and precise measures. Measurement of output voltage from module is up to 1000V DC. Measurement of output current from module is up to 10A DC. Measurement of solar irradiation (W/m^2) is carries out with reference cell. Measurement of output DC and nominal power from module is performed. Numerical and graphical display of I-V curve is available. It Measures the module fill factor. Mechanical inclinometer is integrated for the detection of the incidence angle of solar irradiation. Electrical specifications of "IV 400" are given in Table 2.

We note that accuracy parameter is calculated as ±[% reading + (number of dgts) x resolution] at 23±5°C, <80%HR (Datasheet I-V 400, 2012).

Investigating parameters

The most important electrical characteristics of a PV module are the I-V and P-V curves, short-circuit current I_{sc}, open-circuit voltage V_{oc}, the fill factor FF and the maximum power output P_{max}. They are defined and modeled as follows.

The I-V and P-V curves

The I-V (current-voltage) curve of a PV string (or module) describes its energy conversion capability at the existing conditions of irradiance (light level) and temperature. Conceptually, the curve represents the combinations of current and voltage at which the string could be operated or 'loaded', if the irradiance and cell temperature could be held constant. Figure 2 shows a typical I-V curve, the power-voltage or P-V curve that is computed from it, and key points on these curves. Referring to Figure 2, the span of the I-V curve ranges from the short circuit current (I_{sc}) at zero volts, to zero current at the open circuit voltage (V_{oc}). At the 'knee' of a normal I-V curve is the maximum power point (I_{mp}, V_{mp}), the point at which the array generates maximum electrical power. In an

Table 2. Electrical specifications of "I-V 400".

Parameter	Range	Accuracy	Resolution
Voltage (Vdc)	5.0 ÷ 999.9	0.1	±(1.0%rdg+2dgt)
Current (Idc)	0.10 ÷10.00	0.01	±(1.0%rdg+2dgt)
Power maximal (Wdc)	50 ÷ 9999	1	±(1.0%rdg+6dgt)
Irradiation (mVdc)	1.0 ÷ 100.0	0.1	±(1.0%rdg+5dgt)
Temperature (°C)	-20.0 ÷100.0	0.1	±(1.0%rdg+1°C)

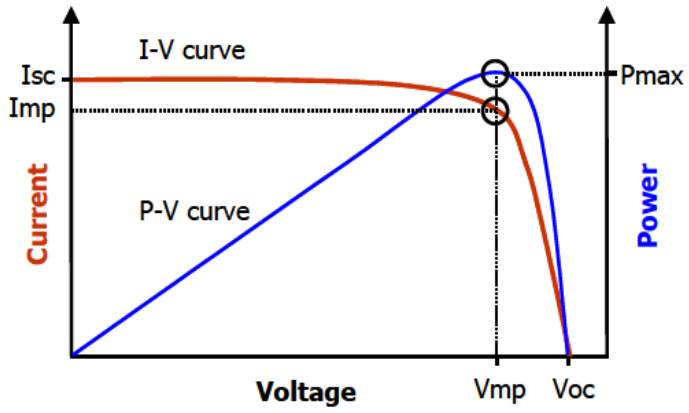

Figure 2. The I-V and P-V curves of a photovoltaic module.

operating PV system, one of the jobs of the inverter is to constantly adjust the load, seeking out the particular point on the I-V curve at which the array as a whole yields the greatest DC power. At voltages well below V_{mp}, the flow of solar-generated electrical charge to the external load is relatively independent of output voltage. Near the knee of the curve, this behavior starts to change. As the voltage increases further, an increasing percentage of the charges recombine within the solar cells rather than flowing out through the load. At V_{oc}, all of the charges recombine internally. The maximum power point, located at the knee of the curve, is the (I,V) point at which the product of current and voltage reaches its maximum value.

The short circuit current I_{sc}

At normal levels of solar irradiance, the short-circuit current can be considered equivalent to the photocurrent I_{ph}, that is, proportional to the solar irradiance G (W/m^2). But this may result in some deviation from the experimental result, so a power law having exponent a is introduced in this paper to account for the non-linear effect that the photocurrent depends on. The short-circuit current I_{sc} of the PV modules is not strongly temperature dependent. It tends to increase slightly with increase of the module temperature. For the purposes of PV module performance, modeling this variation can be considered negligible. Then, the short-circuit current I_{sc} can be simply calculated by:

$$I_{sc} = I_{sc0}\left(\frac{G}{G_0}\right)^a \quad (1)$$

Where I_{sc0} is the short-circuit current of the PV module under the standard solar irradiance G_0; while I_{sc} is the short-circuit current of the PV module under the solar irradiance G; a is the exponent responsible for all the non-linear effects that the photocurrent depends on.

The open-circuit voltage V_{oc}

The relationship of the open-circuit voltage to irradiance is known to follow a logarithmic function based on an ideal diode equation, and the effect of temperature is due to the exponential increase in the saturation current with an increase in temperature (Luis and Sylvestre, 2002). This conclusion causes some difficulties in replicating the observed behaviours of the tested PV modules. Additional terms or some amendatory parameters must be introduced to account for the shunt resistance, series resistance and the non-ideality of the diode. Based on the model given by Van Dyk et al. (2002) and then take into account the effect of temperature, the open-circuit voltage Voc at any given conditions can be expressed by:

$$V_{oc} = \frac{V_{oc0}}{1+b\,ln\frac{G_0}{G}}\left(\frac{T_0}{T}\right)^{\gamma} \quad (2)$$

Where V_{oc} and V_{oc0} are the open-circuit voltage of the PV module under the normal solar irradiance G and the standard solar irradiance G_0; b is a PV module technology specific related dimensionless coefficient (Van Dynk et al., 2002); and γ is the exponent considering all the non-linear temperature–voltage effects.

The maximum power output P_{max}

The photovoltaic module performance is highly affected by the solar irradiance and the PV module temperature. In this paper, we consider a simplified model maximum power-output of PV module to estimate its performance (Ould Bilal et al., 2012). It is given by Equation 3.

$$P_{max} = V_{oc}.I_{sc}.FF \quad (3)$$

Where I_{sc} and V_{oc} are the short-circuit current and open-circuit voltage of solar photovoltaic module (Omer, 2008), FF (dimensionless) is the fill factor. It is the ratio between the nominal and maximum power standard (Koutroulis et al., 2006).

The fill factor FF

The fill factor (FF) of a PV module or string is an important performance indicator. It represents the square-ness (or 'rectangularity') of the I-V curve, and is the ratio of two areas defined by the I-V curve, as illustrated in Figure 3. Although physically unrealizable, an ideal PV module technology would produce a perfectly rectangular I-V curve in which the maximum power point coincided with (I_{sc}, V_{oc}), for a fill factor of 1. The fill factor is important because if the I-V curves of two individual PV modules have the same values of I_{sc} and V_{oc}, the array with the higher fill factor (squarer I-V curve) will produce more power. Also, any impairment that reduces the fill factor will reduce the output power. The fill factor can be expressed by:

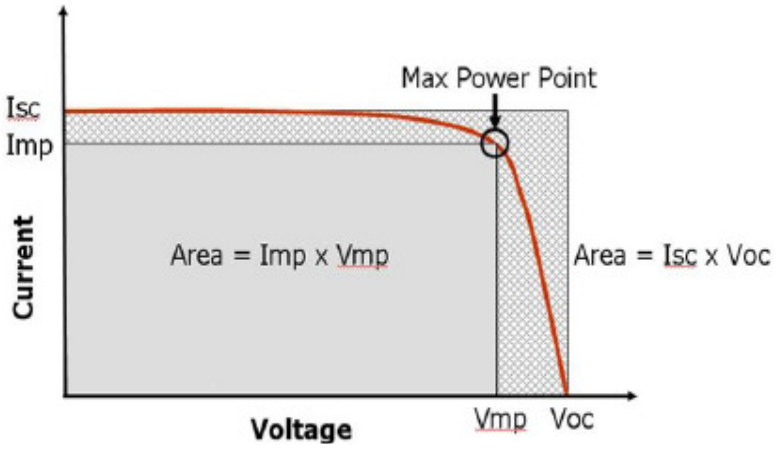

Figure 3. The fill factor, defined as the gray area divided by the cross-hatched area.

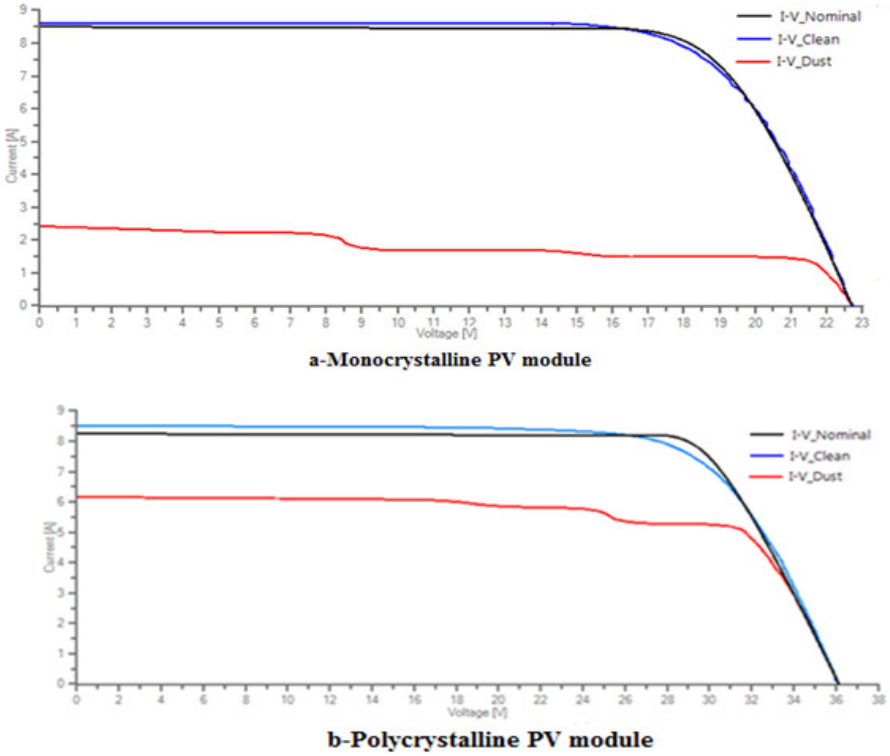

Figure 4. Comparison between the I-V characteristics of PV modules under clean and dusty conditions after one exposition year.

$$FF = \frac{Imp.Vmp}{Isc.Voc} \quad (4)$$

RESULTS AND DISCUSSION

Effect of dust on I-V and P-V characteristics

All tests are performed in the standard test conditions (STC) corresponding to AM 1.5, 25°C and 1000 W/m^2. Shown in Figures 4 and 5 are respectively the current-voltage (I-V) and power-voltage (P-V) curves for PV modules in three conditions: Nominal conditions, PV module clean and PV module dusty for monocrystalline silicon (a) polycrystalline silicon (b) technologies. The I-V and P-V characteristics corresponding to the nominal conditions and clean PV modules clearly present a normal form for both technologies. It may be noted that the curves corresponding to the I-V and P-V modules

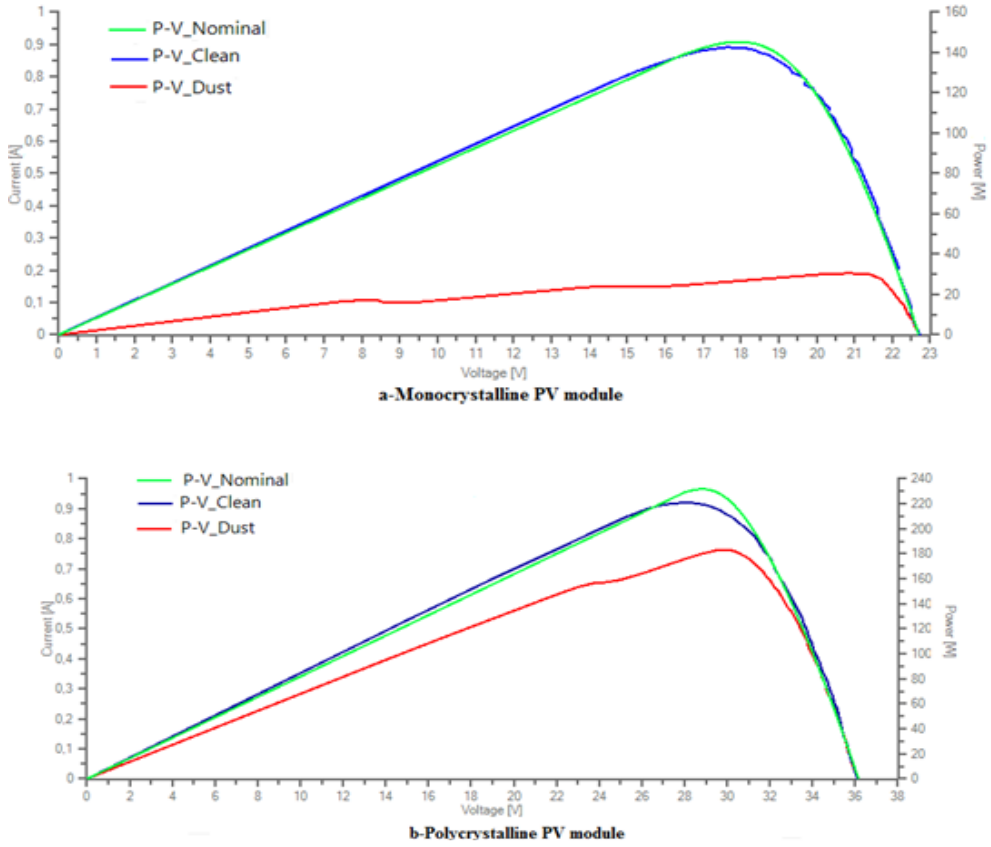

Figure 5. Comparison between the P-V characteristics of PV modules under clean and dusty conditions after one exposition year.

clean after a exposition year are almost confounded with nominal curves for the two technologies. However, a small difference is noted at the short-circuit current (I_{sc}) and maximum current (I_{max}) for the IV characteristic whereas the open-circuit voltage (V_{oc}) shows no significant variation. For the P-V characteristics, a decrease of the maximum power (P_{max}) after one exposition year was noted on the two technologies. These variations in I_{sc}, I_{max} and P_{max} on clean modules after one year of operation reveal a modules degradation probably due to other parameters such as temperature, humidity, UV. The performance of PV modules varies according to the climatic conditions and gradually deteriorates through the years (Sanchez-Friera et al., 2011; Osterwald et al., 2006; Adelstein and Sekulic, 2005; Dunlop and Halton, 2005; Cereghetti et al., 2003). On the other hand, the I-V and P-V characteristics of monocrystalline and polycrystalline PV modules after one exposition year under the natural dust without cleaning are heavily modified. The characteristics I_{sc}, V_{max} and P_{max} present very significant decreases that are evaluated subsequently. The distortion and mismatch recorded on the I-V and P-V curves are due to the dust on the surface of the modules. Indeed, dust induces generally nonuniform shading on the PV modules surface and thereby chains of PV cells are not illuminated with the same intensity. Therefore they do not have the same behavior and characteristics I-V and P-V of modules become modified. The nonuniform shading of the PV module will induce a mismatch effect observed on the I-V and P-V characteristics as shown in Figures 4 and 5 (Mohammadmehdi et al., 2013). Following is devotion to the evaluation of the impact of dust on the PV module characteristics such as: Open-circuit voltage (V_{oc}), short-circuit current (I_{sc}), maximum ouput curreent (I_{max}), maximum output voltage (V_{max}), maximum power output (P_{max}) and fill factor (FF).

Effect of dust on I_{sc}, V_{oc}, P_{max} and FF characteristics

Previously, the impact of dust on the I-V and P-V characteristics of PV modules after one exposion year under Sahelian conditions without cleaning was highlighted. Here, we evaluate the impact of dust after one exposition year on open-circuit voltage (V_{oc}), short-circuit current (I_{sc}), maximum ouput curreent (I_{max}), maximum output voltage (V_{max}), maximum power output (P_{max}) and fill factor (FF) of monocrystalline and polycrystalline PV modules. Table 3 summarizes the

Table 3. A summary of the PV module parameters variation observed after one exposition year (clean and dusty).

Modules	Parameter	Initial value	Clean module after one exposition year	Dusty module after one exposition year	Difference absolute	Difference relative (%)
Monocrystalline PV module	Pmax (W)	145	144.59	32.17	-112.42	-77.75
	Vmax (V)	17.9	17.83	20.79	2.96	16.60
	Imax (A)	8.1	8.06	1.57	-6.49	-80.52
	Voc (V)	22.7	22.7	22.7	0.00	0.00
	Isc (A)	8.5	8.47	2.09	-6.38	-75.32
	FF (%)	75.14	73.64	60.4	-0.13	-17.98
Polycrystalline PV module	Pmax (W)	230	217.37	178.19	-39.18	-18.02
	Vmax (V)	29.2	28.04	30.09	2.05	7.31
	Imax (A)	7.88	7.75	5.93	-1.82	-23.48
	Voc (V)	36.6	36.16	36.16	0.00	0.00
	Isc (A)	8.44	8.33	6.61	-1.72	-20.65
	FF (%)	74.48	72.09	70.64	-0.01	-2.01

characteristic variations (V_{oc}, I_{sc}, $I_{max,}$ $V_{max,}$ P_{max} and FF) induced by the dust deposition on the PV modules surface. All tests are performed in the standard test conditions (STC). To assess the impact of dust on the performance characteristics of PV modules we calculate the absolute and relative difference between the case where the modules were not cleaned after an exposition year under Sahelian environment and the case where they are cleaned after one operation year under the same environment. Dust deposition on the modules decreases strongly the maximum power for both technologies. The maximum power output (P_{max}) loss can be from 18 to 78%, respectively for the polycrystalline module (pc-Si) and monocrystalline module (mc-si).

Studies carried out in Egypt have shown that this decrease of P_{max} due by the dust could reach 35% after only two months without cleaning PV modules (Ibrahim et al., 2009). The test results on two PV modules technologies reported in Table 3 have also shown that short-circuit current (I_{sc}), maximum output current (I_{max}) and fill factor (FF) are affected by the dust deposits on the PV modules surface. Indeed, we find that the decrease of I_{max} relative to clean modules may vary from 23 to 80% for respectively pc-Si and mc-Si modules. The fill factor (FF) may decrease from 2% for the pc-Si module to 17% for the mc-Si module. However, the maximum voltage output (V_{max}) and the open-circuit voltage (V_{oc}) are not affected by dust accumulation for both technologies studied. All values given in Table 3 are related to the standard test conditions (AM 1.5, 25°C, 1000 W/.m^2).

Conclusion

The effect of the presence of dust on the photovoltaic module surface was studied under Sahelian environment. Two PV modules technologies (monocrystalline and polycrystalline silicon) were exposed during one year on the site of Dakar University in Senegal. Dust has an effect on the parameters performance of photovoltaic modules. The impact of dust on the I-V and P-V characteristics of PV modules after an exposition year under Sahelian conditions without cleaning was highlighted. In the study, it was also shown that the relative differences of PV module performance parameters between the case where the modules were not cleaned after an exposition year under Sahelian environment and the case where they are cleaned after one operation year under the same environment are generally very high. P_{max}, I_{max}, I_{sc} and FF are the most affected performance characteristics by the dust deposits on the PV modules surface. The maximum power output (P_{max}) loss can be from 18 to 78% respectively for the polycrystalline module (pc-Si) and monocrystalline module (mc-si). I_{max} loss can vary from 23 to 80% for respectively pc-Si and mc-Si modules. However, the maximum voltage output (V_{max}) and the open-circuit voltage (V_{oc}) are not affected by dust accumulation for both technologies studied. The fill factor (FF) may decrease from 2% for the pc-Si module to 17% for the mc-Si module. In perspective, we will work with many more PV modules from different manufacturers over a longer duration. This project also aims to measure the amounts of dust deposited on the modules of different technologies in order to investigate on the best adapted technologies to Sahelian environment. We can already say that the cleaning of PV modules exposed in a Sahelian environment must be integrated into a plan of periodic preventive maintenance.

ACKNOWLEDGMENT

The authors would like to thank the French cooperation in Senegal which allowed the purchase of equipment used

in this work through the U3E project.

REFERENCES

Adelstein J, Sekulic B (2005). Performance and Reliability of a 1-kW Amorphous Silicon Photovoltaic Roofing System, Proceedings of the 31st IEEE Photovoltaics Specialists Conference, ISBN 0-7803-8707-4, Lake Buena Vista, USA, January 2005. pp. 1627-1630.

ANAMS: National Agency for Meteorology of Senegal (2012). http://WWW.meteo-senegal.net.

Catelani M, Ciani L, Cristaldi L, Faifer M, Lazzaroni M, Rossi M (2012). Characterization of photovoltaic panels: The effects of dust. Instrumentation and Measurement Technology Conference (I2MTC), 2012 IEEE International. May 2012.

Cereghetti N, Bura E, Chianese D, Friesen G, Realini A, Rezzonico S (2003). Power and Energy Production of PV Modules Statistical Considerations of 10 Years Activity, Proceedings of the 3rd World Conference on Photovoltaic Energy Conversion, pp. 1919-1922, ISBN 4-9901816-0-3, Osaka, Japan, May 2003.

Datasheet I-V 400 (2012). www.ht-instruments.com/pdf_I-V400.

Detrick A, Kimber A, Mitchell L (2005). Performance Evaluation Standards for Photovoltaic Modules and Systems, Proceedings of the 31st IEEE Photovoltaics Specialists Conference, ISBN 0-7803-8707-4, Lake Buena Vista, USA, January 2005. pp. 1581-1586.

Dunlop ED, Halton D (2005). The Performance of Crystalline Silicon Photovoltaic Solar Modules After 22 Years of Continuous Outdoor Exposure. Progress in Photovoltaics: Research and Applications, June 2005. 14(1):53-64.

Hammond R, Srinivasan D, Harris A, Whitfield K, Wohlgemuth J (1997). Effects of Soiling on PV Module and Radiometer Performance, Proceedings of the 26th IEEE Photovoltaics Specialists Conference, pp. 1121-1124, ISBN 0-7803-3767-0, Anaheim, USA, September 1997.

Hottel MC, Woertz BB (1942). Performance of flat plate solar heat collectors. ASME Trans. 64:91-104.

Ibrahim M, Zinsser B, El-Sherif H, Hamouda E, Makrides G, Georghiou GE, Schubert M, Werner JH (2009). Advanced Photovoltaic Test Park in Egypt for Investigating the Performance of Different Module and Cell Technologies, Proceedings of the 24th Symposium Photovoltaic Solar Energy, Staffelstien, Germany, March 2009.

Katz GB (2011). Effect of Dust on Solar Panels. www.gregorybkatz.com/Home/effect-of-dust-on-solar-panels.

Koutroulis E, Kolokotsa D, Potirakis A, Kalaitzakis K (2006). Methodology for optimal sizing of stand-alone photovoltaic/wind generator systems using genetic algorithms. Solar Energy 80:1072-1088.

Kymakis E, Kalykakis S, Papazoglou TM (2009). Performance Analysis of a Grid Connected Photovoltaic Park on the Island of Crete. Energy Conver. Manage. 50(3):433-438.

Luis C, Sivestre S (2002). Modelling photovoltaic systems using PSpice. Chichester: John Wiley & Sons Ltd.

Mohammadmehdi S, Saad M, Rasoul R, Rubiyah Y, Ehsan TR (2013). Analytical Modeling of Partially Shaded Photovoltaic Systems. Energies 6:128-144; doi:10.3390/en6010128.

Omer AM (2008). On the wind energy resources of Sudan. Renew. Sustain. Energy Rev. 12:2117-2139.

Osterwald CR, Adelstein J, del Cueto JA, Kroposki B, Trudell D, Moriarty T (2006). Comparison of Degradation Rates of Individual Modules Held at Maximum Power, Proceedings of the 4th IEEE World Conference on Photovoltaic Energy Conversion, ISBN 1-4244-0017-1, Waikoloa, USA, May 2006. pp. 2085-2088.

Ould Bilal B, Sambou V, Kébé CMF, Ndiaye PA, Ndongo M (2012). Methodology to size an optimal stand-alone PV/wind/diesel/battery system minimizing the levelized cost of energy and the CO2 emissions. Energy Procedia 14:1636-1647.

PSA : Senegalese-German program (2011). DASTPVPS\SOLARIRR.INS.

Salim A, Huraib F, Eugenio N (1988). PV power-study of system options and optimization. In Proceedings of the 8th European PV Solar Energy Conference, Florence, Italy.

Sanchez-Friera P, Piliougine M, Pelaez J, Carretero J, Sidrach M (2011). Analysis of Degradation Mechanisms of Crystalline Silicon PV Modules After 12 Years of Operation in Southern Europe. Progress in Photovoltaics: Research and Applications, January 2011.

Shaharin AS, Haizatul HH, Nik Siti HNL, Mohd SIR (2011). Effects of Dust on the Performance of PV Panels. World Acad. Sci. Eng. Technol. P. 58.

Sharma V, Bowden S (2012). Peak load offset and the effect of dust storms on 10 MWp distributed grid tied photovoltaic systems installed at Arizona State University. Photovoltaic Specialists Conference (PVSC), 2012 38th IEEE, June 2012.

van Dyk EE, Meyer EL, Vorster FJ, Leitch AWR (2002). Long-term monitoring of photovoltaic devices. Renew. Energy 22:183-197.

Wakim F (1981). Introduction of PV power generation to Kuwait. Kuwait Institute for Scientific Researchers, Kuwait City, 1981.

Wofrance (2012).http://www.wofrance.fr/weather/maps/city

Zhou W, Yang H, Fang Z (2007). A novel model for photovoltaic array performance prediction. Appl. Energy 84:1187-1198.

academicJournals

Vol. 8(21), pp.1174-1178, 9 June, 2013
DOI: 10.5897/IJPS12.476
ISSN 1992-1950 © 2013 Academic Journals
http://www.academicjournals.org/IJPS

International Journal of Physical Sciences

Full Length Research Paper

Structural properties of binary semiconductors

D. S. Yadav[1] and Chakresh Kumar[2]*

[1]Department of Physics, Ch. Charan Singh P G College, Heonra, Etawah-206001 (U.P.) India.
[2]Department of Electronics and Communication Engineering Tezpur University, Napam-784001, India.

Accepted 30 May, 2013

Using the plasma oscillations theory of solids, 2 empirical relations have been proposed for the calculation of the structural properties such as bond-stretching central force constant (*α*) and bond-bending non-central force constant (*β*) for II-VI and III-V group binary semiconductors. We find that α =D $(\hbar\omega_p)^2$ and β = S $(\hbar\omega_p)^2$, where D and S are constants. The numerical values of *D* and *S* are respectively, 0.151 and 0.016 for II-VI and 0.177 and 0.031 for III-V group binary semiconductors. The structural properties of binary semiconductors exhibit a linear relationship when plotted on a log-log scale against the plasmon energy $\hbar\omega_p$ (in eV), which lies on the straight lines. We have applied the proposed empirical relations on these binary semiconductors and found a better agreement with the experimental data as compared to the values evaluated by earlier researchers.

Key words: Plasmon energy, structural properties, III-V and II-VI Semiconductors.

INTRODUCTION

In recent years (Kamran et al., 2008; Kumar et al., 2010; Hasan et al., 2009, 2010; Breidi et al., 2010), II-VI and III-V group binary tetrahedral semiconductors have been extensively studied because of their technical and scientific importance and because they have zinc-blende and wurtzite structure. Using the valence-force-field model of Keating (Keating, 1966), the elastic properties of II-VI and III-V group semiconductors with a sphalerite-structure have been analyzed by Martin (Martin, 1970) and several other workers (Phillips, 1970; Yogurtcu et al., 1981).

A considerable amount of discrepancies have been obtained between theory and experiment in determining vibrational modes on the basis of the model parameters derived from elastic constant data. Nowadays more reliable elastic constant data are available which differ partially from those obtained by Martin (Martin, 1970). In the Martin analysis, the contribution of Coulomb force to the elastic constants has been described in terms of macroscopic effective charge which is responsible for the splitting of transverse and longitudinal optical modes. Lucovsky et al. (1971) has pointed out that the Martin approach (Martin, 1970) is incorrect. The ratio of β/α = 0.3 $(1-f_i)$ measures the importance of covalent bonds in determining the stability of the tetrahedral structures. The overall trend of (β/α) tends to zero for purely ionic crystal that is, for which ionicity (f_i) is unity.

Neumann (1985, 1989) has extended the Keating model (Keating, 1966) considering localized effective charge to account for long range Coulomb force and dipole-dipole interaction in analysing the vibrational properties of binary and ternary compounds with a sphalerite-structure. Neumann (1985) has taken experimental values of bond length d (in nm) and spectroscopic bond iconicity (f_i) (Phillips, 1970) to determine the constant associated with the above theory. Reddy et al. (2003) have reported a simple correlation between lattice energy, bond stretching and bond bending force constants, ionicity and micro-hardness for $A^{II}B^{VI}$ and $A^{III}B^{V}$ semiconductors.

*Corresponding author. chakreshk@gmail.com

PACS Nos. : 52.25.-b, 72.80.Ey.

Recently, Yadav and Singh (2012) have calculated the static and dynamical properties of II-VI and III-V group binary solids with the help of plasma oscillations theory. This is based on the fact that the plasmon energy, $\hbar\omega_p = \hbar (4\pi ne^2/m)$, is related to the effective number of valence electrons (n) in a compound. In many cases empirical relations do not give highly accurate results for each specific material, but they still can be very useful.

In particular, the simplicity of empirical relation allows a broader class of researchers to calculate useful properties and often trend become more evident. Therefore, we thought it would be of interest to give an alternative explanation for bond stretching central force constant (α in N/m) and bond-bending non-central force constant (β in N/m) of II-VI and III-V group binary semiconductors.

The purpose of this work is to obtain structural properties of the II-VI and III-V group binary semiconductors using the plasma oscillations theory of solids. The theoretical concept is given. We also presented and discussed the simulation results for structural properties of binary semiconductors. Finally, the conclusion is given.

THEORETICAL CONCEPTS

The nearest-neighbour bond-stretching central forces have been characterized by the parameter *α,* and next neighbor bond-bending non-central forces by the parameter *β*. These parameters depend on inter-atomic distance obtained from lattice vibration data. The lattice vibration data have been further obtained from various types of two-body inter-atomic potential given in literature. Such potentials have the advantage of keeping the repulsive and attractive forces in the same mathematical form.

The simplest form of inter-atomic potential has been described by Neumann (1989), Harrison (1983) and Harrison and Freeman (1989) in which it has been assumed that both the repulsive and attractive parts of inter-atomic potential are described by the power law of inter-atomic distance (*d*). This form of potential for the total energy or cohesive energy per pair of atom can be written as (Neumann, 1989):

$$V_1(d) = C/d^m - D/d^n \quad (1)$$

Where *C*, *D, m* and *n* are numerical constants and *d* is the nearest neighbour distance.

These parameters have been estimated for equilibrium condition when the repulsion is half of the attraction that is m = 2n (Neumann,1989) and the following equation has been obtained:

$$\alpha = \alpha_0 d^{-x} \quad (2)$$

where α_0 and *x* are the constants. The other form of potential is based on Morse potential. In this type of potential both the repulsive and attractive terms are described by exponential functions of inter-atomic distance.

The general form of Morse potential is given by Neumann (1989):

$$V_2(d) = A \exp(-ad) - B \exp(-bd) \quad (3)$$

Where *A, B, a* and *b* are constants. The above equation has been further used to describe the two-body interaction in total energy calculation of Si (Sobotta et al., 1986). Neumann (1985, 1989) has also extended it to ternary chalcopyrites. Solving above equation (3) for equilibrium condition a = 2b, the following relation has been obtained Neumann (1989).

$$\alpha = \alpha_1 \exp(-bd) \quad (4)$$

where α_1 and *b* are the numerical constants. Presently, Reddy et al. (2003) has described the correlation between lattice energy, bond stretching force constant (*α*) and bond banding force constant (*β*) for $A^{II}B^{VI}$ and $A^{III}B^{V}$ compound semiconductors as follows:

$$\alpha = m_\alpha U - b_\alpha \quad (5)$$

$$\beta = m_\beta U - b_\beta \quad (6)$$

where m_α, m_β, b_α, and b_β are constants.

Recently, Verma (2009) has derived an empirical relations for the bond-stretching and bond-bending force constants of $A^{II}B^{VI}$ and $A^{III}B^{V}$ group binary solids in term of the product of ionic charges of cation and anion with nearest-neighbor distance *d* (in A^0) by the following expressions as:

$$\alpha = A (Z_1 Z_2)^S d^{-3} \quad (7)$$

$$\beta = V (Z_1 Z_2)^B d^{-3} \quad (8)$$

Where *A*, *S*, *V* and *B* are the numerical constants depending upon the group of materials. In a previous work (Yadav and Singh, 2012) we proposed the simple expressions for static and dynamical properties such as bulk modulus B (in GPa) and cohesive energy E_{coh} (in Kcal/mole) of II-VI and III-V group binary solids in term of the plasmon energy $\hbar\omega_p$ (in eV) by the following relations:

$$B = D (\hbar\omega_p)^S \quad (9)$$

$$E_{Coh} = D^* (\hbar\omega_p)^{S^*} \quad (10)$$

Where *D*, *S D** and *S** are numerical constants. Using this idea to get better agreement with experimental and theoretical data for the bond-stretching and bond-bending force constants of binary semiconductors, equations (7) and (8) may be extended as:

$$\alpha = D (\hbar\omega_p)^2 \quad (11)$$

$$\beta = S (\hbar\omega_p)^2 \quad (12)$$

Where D and S are numerical constants, depends upon the structure of the compounds, semiconductor and plasmon energy (ħωp) (Yadav and Singh, 2012; Kumar et al., 1996). The values of D and S turn out to be equal to 0.151 and 0.016 for II-VI group and 0.177 and 0.031 for III-V group binary solids, respectively. A detailed study of structural properties of these materials has been given elsewhere (Keating, 1966; Martin, 1970; Phillips, 1970; Yogurtcu et al., 1981; Lucovsky et al., 1971; Van-Vechten, 1969) and will not be presented here.

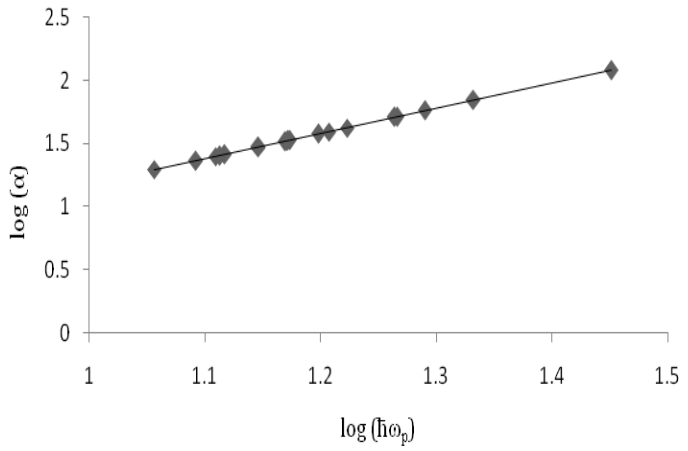

Figure 1. Plot of bond-stretching force constant versus plasmon energy of II-VI group binary semiconductors.

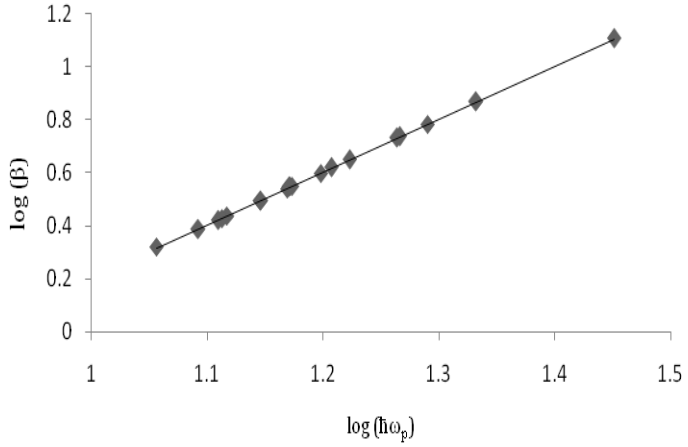

Figure 2. Plot of bond-bending force constant versus plasmon energy of II-VI group binary semiconductors.

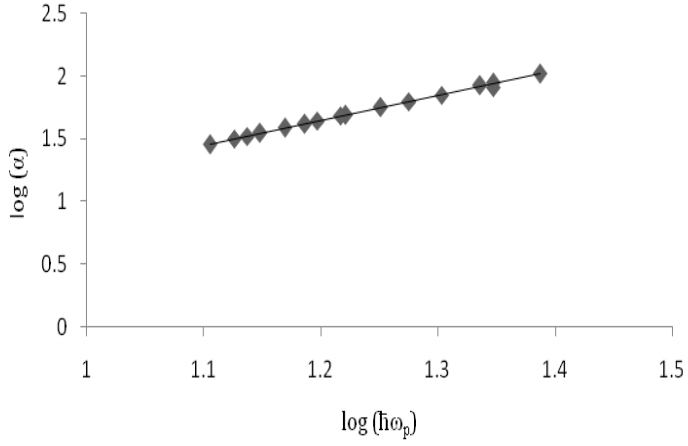

Figure 3. Plot of bond-stretching force constant versus plasmon energy of III-V group binary semiconductors.

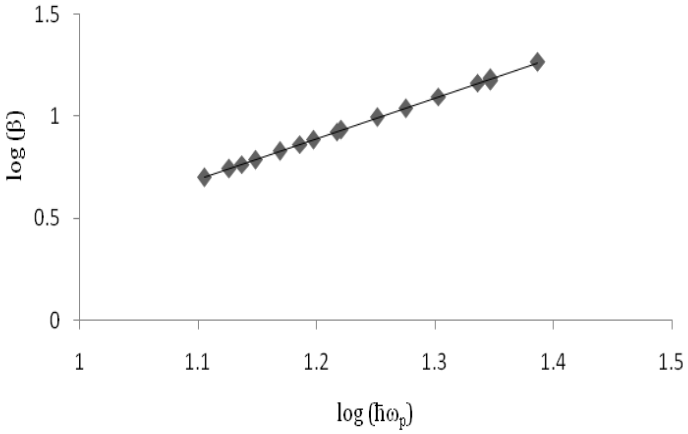

Figure 4. Plot of bond-bending force constant versus plasmon energy of III-V group binary semiconductors.

RESULTS AND DISCUSSION

The present paper reports 2 expressions between the bond stretching force constant α (in N/m) and bond-bending force constant β (in N/m) with their plasmon energy of binary semiconductors. This can be successfully employed to estimate the bond stretching and bond-bending force constant from their plasmon energies. We have plotted log-log curve for II-VI and III-V group binary semiconductors, which are presented in Figures 1 to 4, we observed that in the plot of inter-atomic force constants and $\hbar\omega_p$ of these materials, the data points lies on the straight lines.

From this Figure 1 to 4, it is quite obvious that the bond stretching force constant (α) and bond-bending force constant (β) trends in these compounds increase with increasing their plasmon energy and lies on the straight line. The proposed empirical relations (11) and (12) have been applied to calculate the structural properties of binary semiconductors. The calculated values are presented in Tables 1 and 2, respectively, along with their literature values. We note that the values of the bond stretching and bond-bending force constant calculated from our proposed empirical relations are in fairly good agreement with the values reported by earlier researchers (Neumann, 1985, 1989; Reddy, 2003; Verma, 2009).

These results shows that our current approach is quite reasonable and can give us a useful guide in calculating and predicting the inter-atomic force constants of these materials.

Conclusion

From the above results and discussion obtained by using the proposed empirical relation based on plasma oscillations theory of solids, it is quite obvious that the

Table 1. Structural properties of II-VI group binary semiconductors.

$A^{II}B^{VI}$	$\hbar\omega_p$ (eV) [16, 21]	α (in N/m)				β (in N/m)			
		Calc.	[20]	[12-14]	[15]	Calc.	[20]	[12-14]	[15]
ZnO	21.48	69.67	---	---	71.31	7.38	---	---	6.973
ZnS	16.71	42.16	42.22	44.73	48.67	4.46	4.46	4.36	4.561
ZnSe	15.78	37.60	36.34	38.61	44.18	3.98	3.84	4.65	4.083
ZnTe	14.76	32.89	29.40	32.04	39.02	3.48	3.11	4.47	3.534
ZnPo	12.36	23.07	---	---	---	2.44	---	---	---
CdO	18.46	51.45	---	---	---	5.45	---	---	---
CdS	14.88	33.43	33.81	---	39.70	3.54	3.57	---	3.606
CdSe	14.01	29.64	30.08	---	35.21	3.14	3.18	---	3.128
CdTe	13.09	25.87	24.38	29.44	30.21	2.74	2.58	2.48	2.602
CdPo	11.43	19.73	--	---	---	2.09	---	---	---
BeO	28.25	120.50	---	---	---	12.76	---	---	--
BeS	19.52	57.53	---	---	62.64	6.08	----	---	6.018
BeSe	18.39	51.06	---	---	56.96	5.41	---	---	5.445
BeTe	16.12	39.24	---	---	45.75	4.16	--	---	4.250
BePo	14.91	33.56	---	---	---	3.55	---	---	---
HgS	14.84	33.25	33.41	---	---	3.52	3.53	---	---
HgSe	13.99	29.55	29.74	37.43	---	3.13	3.14	2.37	---
HgTe	12.85	24.93	24.65	29.32	---	2.64	2.61	2.54	---
MgTe	12.97	25.40	---	---	29.83	2.69	---	---	2.555

Table 2. Structural properties of III-V group binary semiconductors.

$A^{III}B^{V}$	$\hbar\omega_p$ (eV)	α (in N/m)				β (in N/m)			
	[12, 30*]	Calc.	[15]	[20]	[12- 14]	Calc.	[15]	[20]	[12- 14]
BN	22.75	91.60	88.357	---	---	16.04	17.179	---	---
BP	21.71	83.71	75.037	87.14	---	14.61	14.447	15.60	---
BAs	20.12	70.80	67.044	74.95	---	12.54	12.855	13.42	---
BSb	17.85	56.39	---	56.61	---	9.87	---	10.14	---
AlN	22.27	87.78	81.091	97.30	---	15.37	15.705	17.42	---
AlP	16.65	49.06	49.122	48.41	---	8.59	9.219	8.67	---
AlAs	15.75	43.90	44.278	44.34	---	7.68	8.236	7.94	---
AlSb	13.72	33.31	33.137	33.81	35.74	5.83	5.975	6.05	6.63
GaN	20.46	74.10	76.248	95.76	---	14.97	14.722	17.15	---
GaP	16.50	48.18	48.395	48.41	48.57	8.44	9.071	8.67	10.40
GaAs	15.35	41.70	42.098	43.27	43.34	7.30	7.794	7.75	8.88
GaSb	13.38	31.68	31.200	34.19	34.42	5.55	5.582	6.12	7.16
InN	18.82	62.69	60.505	70.70	---	10.97	11.528	12.66	---
InP	14.76	38.56	38.950	38.83	44.29	6.75	7.155	6.95	6.26
InAs	14.07	35.04	35.075	35.79	37.18	6.14	6.369	6.41	5.47
InSb	12.73	28.68	27.567	28.68	30.44	5.02	4.845	5.14	4.73

bond stretching and bond-bending force constant reflecting the structural properties can be expressed in term of plasmon energy of these materials; this is a surprising phenomenon. The calculated values of these parameters are presented in Table 1 and 2, respectively. We come to the conclusion that plasmon energy of any compound is the input parameter for calculating the structural properties. The inter-atomic force constants of

binary semiconductors exhibit a linear relationship when plotted on a log-log scale against the plasmon energy $\hbar\omega_p$ (in eV), which lies on the straight lines.

In the present study, we find that both the inter-atomic force constants α and β directly depends upon the plasmon energy of these compounds semiconductor. Thus, this theory can be easily extended to binary semiconductors. A fairly good agreement between our calculated values of inter-atomic force constants with the values reported by earlier researchers has been found. It is also note worthy that the proposed empirical relations are simple and widely applicable.

REFERENCES

Breidi A, Hasan Haj El F, Nouet G, Drablia S, Meradji H, Pages O, Ghemid S (2010). Theoretical study **of** InAs, InSb and their alloys InAsxSb1-x. J. Alloys Compounds 49380.

Harrison WA (1983). A theory of force constant models is derived for tetrahedral semiconductors from Harrison's Phys. Rev. B 27:3592.

Harrison WA, Freeman WH (1989). Electronic Structure and the Properties of Solids (Dover, New York, 1989).

Hasan El Haj F, Annane F, Meradji H, Ghemid S (2010). First principle investigation of AlAs and AlP compounds and ordered $AlAs_{1-x}P_x$ alloys, Comput. Mater. Sci., 50: 274-278.

Hasan El Haj F, Drablia S, Meradji H, Ghemid S, Nouet G (2009). First principles investigation of barium chalcogenide ternary alloys Computational Mater. Sci. 46:376–382.

Kamran S, Chen K, Chen L (2008). Semi-empirical formulae for elastic moduli and brittleness of covalent crystals", Phys. Rev. B 77:094109.

Keating PN (1966). Effect of Invariance Requirements on the Elastic Strain Energy of Crystals with Application to the Diamond Structure, Phys. Rev. 145:637–645.

Kumar V, Prasad GM, Chetal AR, Chandra D (1996). Microhardness and bulk modulus of binary tetrahedral semiconductors, 57(4):503–506.

Kumar V, Shrivastava AK, Jha V (2010). Bulk modulus and microhardness of tetrahedral semiconductors, J. Phys. Chem. Solids, 71:1513.

Lucovsky G, Martin RM, Burstein E (1971). Localized Effective Charges in Diatomic Crystals Phys. Rev. B 4:1367–1374.

Martin RM (1970). Elastic Properties of ZnS Structure Semiconductors. Phys. Rev. B1:4005.

Neumann H (1985). Interatomic force constants and localized effective charges in sphalerite-structure compounds. Cryst. Res. Technol. 20(6):773-780.

Neumann H (1989). Interatomic force constants in AIIBIVCV2 chalcopyrite compounds. Cryst. Res. Technol. 24(6):619-624.

Phillips JC (1970). Bonds and Bands in Semiconductors ,Rev. Mod. Phys. 42:317.

Reddy RR, Nazeer Ahammed Y, Abdul Azeem P, Gopal KR, Sasikala D, Rao TVR, Behere SH (2003). Interatomic force constants, ionicity and microhardness of binary tetrahedral semiconductors. Ind. J. Phys. 77(3):237-241.

Sobotta H, Neumann H, Reide V, Kuhn G (1986). Lattice vibrations and interatomic forces in LiInS2. Cryst. Res. Technol. 21:1367-1371

Van Vechien JA (1969). Quantum dielectric theory of electronegativity in covalent systems. I. Electronic dielectric constant. Phys. Rev. 182:891-905.

Verma AS (2009). Electronic and Optical Properties of Rare-earth Chalcogenides and Pnictides, Afr. Phys. Rev. 3:0003.

Yadav DS, Singh DV (2012). Static and dynamical properties of II–VI and III–V group binary Solids,Phys.Scr. 85:015701.

Yogurtcu YK, Miller AJ, Saunders GA (1981). Pressure dependence of elastic behaviour and force constants of GaP. J. Phys. Chem. Solids 42(1):49-56.

academicJournals

Vol. 8(21), pp. 1179-1189, 9 June, 2013
DOI: 10.5897/IJPS12.517
ISSN 1992-1950 © 2013 Academic Journals
http://www.academicjournals.org/IJPS

International Journal of Physical Sciences

Full Length Research Paper

Relationship between magnetospheric interplanetary parameters and radio refractivity for quiet and disturbed days at Minna

G. A. Agbo, O. N. Okoro and J. E. Ekpe

Department of Industrial Physics, Ebonyi State University, P. M. B. 053, Abakaliki, Nigeria.

Accepted 13 May, 2013

The relationship of magnetospheric interplanetary parameters with radio refractivity is investigated from hourly measurement of solar wind energy and interplanetary parameters for quiet and disturbed days during dry and rainy season in Minna (Latitude 9° 36' 50" N and Longitude 6° 33' 24" E) North central, Nigeria for the year 2008. The solar wind energy, magnetospheric interplanetary parameters and radio waves are characterized by large-scale interactions. These introduce both random and systematic variations in radio refractivity which virtually causes variations in radio propagation. Data used for this work is made up of hourly interval record of solar wind energy and interplanetary parameters calculated from data obtained from the Center for Basic Space Science (CBSS), University of Nigeria, Nsukka. The data was obtained using Vantage PRO II Automatic Weather station, and also through http://omniweb.gsfc.nasa.gov/ for each day in all the months of the year in 2008. The result showed that variations of solar wind energy, radio refractivity and interplanetary parameters with time are almost an hourly cycle each following almost the same trend line for both quiet and disturbed days during dry and rainy season. The result of the correlation analysis of solar wind energy and radio refractivity also showed that solar wind energy has square of the correlation coefficients, $R^2 = 0.176$, $R^2 = 0.040$, $R^2 = 0.319$ and $R^2 = 0.016$ for both quiet and disturbed days during dry and rainy seasons which reviews weak correlation. Similarly, proton density (PD) and Dst Index, showed high correlation with square of the correlation coefficients, $R^2 = 0.598$ and $R^2 = 0.5949$, respectively for quiet day during dry season, and for disturbed day during dry season only PD showed high degree of correlation with square of the correlation coefficient, $R^2 = 0.543$. But during rainy season, the result indicated that there is no significant correlation existing between any of the interplanetary parameters with radio refractivity for both quiet and disturbed days.

Key words: Magnetospheric interplanetary parameters, radio refractivity.

INTRODUCTION

Magnetospheric structures and boundaries are ever changing with solar wind conditions, the interplanetary magnetic field (IMF), and substorm activity (Russell et al., 1998). In order to understand and quantify magnetospheric processes, one must understand the electromagnetic field and plasma topology which, in spite of many years of *in situ* observations, has not been mapped on a global scale (Fuselier et al., 1991).

According to some researchers, magnetospheric boundaries are in constant motion during solar wind magnetosphere coupling processes (Russell, 2000), this constant motion is responsible for the overall shape of

*Corresponding author. E-mail: bathonjoku@yahoo.com. Tel: +2348062394152.

Earth's magnetosphere, and fluctuations in its speed, density, direction, and entrained magnetic field which strongly affect Earth's local space environment. For example, the levels of ionizing radiation and radio interference can vary by factors of hundreds to thousands, and the shape and location of the magnetopause and bow shock wave upstream of it can change by several Earth radii, exposing geosynchronous satellites to the direct solar wind (Fuselier et al., 1997).

Enhanced solar wind flow velocities and densities, such as those that can occur in coronal mass ejection (CME) events, can easily distort the dayside magnetopause and push it inside its normal location at about ten Earth radii distance (Phan et al., 1994). During large solar wind disturbances, the magnetopause can be pushed inside the geosynchronous orbit (Phan et al., 1994). At such times, the magnetic field increases to as much as twice its “quiescent” value. In addition, the magnetic field outside the magnetopause will have a polarity that is predominantly opposite to that inside the magnetosphere (Phan et al., 1994). CMEs generally form a large magnetic flux rope that propagates into interplanetary space.

The large flux rope contains very low density and a strong field that is observed to slowly rotate as the rope passes an observer. The ICME flux rope is often referred to as a magnetic cloud and if the cloud is oriented properly, it will produce a long steady period of slowly varying southward IMF at the magnetopause. If the flux rope is propagating faster than the Alfven velocity through the ambient solar wind plasma, a shock front and sheath will form in front of the cloud. The sheath may also contain large southward IMF parameters for a substantial period, prior to the encounter with the magnetic cloud. Some of the most severe magnetic storms, the so-called ‘double hit storms’ develop in response to these two subsequent intervals of sustained strong southward IMF parameters at the magnetopause leading to a complex radio refractivity changes within such period. Okoro et al. (2012) showed that solar wind-magnetosphere coupling can cause serious effect on radio refractivity in atmosphere. Thus, this work investigates the relationship between such Earth-magnetospheric interplanetary parameters with radio refractivity during solar events within the atmosphere.

Theoretical analysis

The study of the solar wind interaction with the planetary bodies is one of the main topics of space weather. During a geomagnetic storm, the sun and the magnetosphere are connected, giving rise to severe changes both in interplanetary space and terrestrial environment (Baker et al., 1998). Some examples are the acceleration of charged particles, enhancement of electric currents, auroras and magnetic field variations on the earth surface. These changes can produce important damages in electric power supplier, radio communications and spacecrafts. It is assumed that sun-earth interaction depends on solar wind. In fact, in-tense geomagnetic storms seem to be related to intense IMF with a southern component for a long time (Tsurutani and Meng, 1972). Several papers about geomagnetic storms (Dungey, 1963) have pointed out that reconnection between a southern IMF and the magnetospheric magnetic field as the physical mechanism responsible for sun-earth connection. Although several aspects on this mechanism are still open questions, it is accepted that reconnection in the day-side of magnetosphere produces a transference of magnetic flux to the magnetotail (Rickett, 1990). Then energetic particles of solar wind can go into the magnetosphere, along magnetic field lines, yielding an injection of plasma in the night-side of the magnetosphere.

The radiation belts are regions of terrestrial environment where charged particles become trapped on closed geomagnetic field lines. These particles show drifts due to magnetic field gradient and curvature as well as to gyration orbit effects. As drifts depend on the sign of charge, ions travel to West and electrons to east, giving rise to a ring current (RC) which extends from 4 to 8 terrestrial radii. Variations on this current result in variations of the magnetic field on the earth surface.

The main mechanism by which the magnetized solar wind powers the magnetosphere was first proposed by Dungey (1963). In his proposal, he stated that solar wind and magnetosphere are connected by IMF southward, and becomes connected to the terrestrial magnetic field at the sub solar point in a process known as reconnection. Reconnection produces open field lines with one end connected to the earth, by combining interplanetary field lines, not connected to the earth, with closed field lines, connected to the earth on both ends. The resulting V-shaped magnetic fields attempt to straighten and accelerate plasma (whose origin is both in the solar wind and the magnetosphere).

The earth's magnetosphere is a very dynamical system, whose configuration depends on many internal and external factors. The first factor is orientation of the earth's magnetic axis with respect to the direction of the incoming solar wind flow, which varies with time because of (i) Earth's diurnal rotation and its yearly orbital motion around sun, and (ii) frequent "side gusts" of the solar wind. The second is the state of the solar wind, in particular, the orientation and strength of the IMF**,** carried to the earth's orbit from sun due to the high electrical conductivity of the solar wind plasma. Interaction between the terrestrial and interplanetary fields becomes much more effective when the IMF turns ant-parallel to the earth's field on the dayside boundary of the magnetosphere. In this case, geomagnetic and interplanetary field lines connect across the magnetospheric boundary, which greatly enhances the

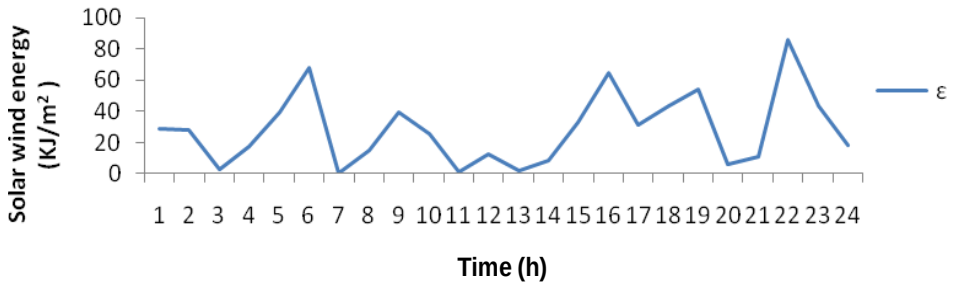

Figure 1. Variations of solar wind energy with time for quiet day during dry season.

transfer of the solar wind mass, energy, and electric field inside the magnetosphere. As a result, the magnetospheric field and plasma become involved in convection.

MATERIALS AND METHODS

The data used for this work covered the period of 1 year starting from January to December, 2008. The data are in two forms. First one is meteorological parameters which are raw recorded 5 min data of temperature, humidity and pressure. These data were provided by the Centre for Basic Space Science (CBSS), University of Nigeria Nsukka.

The second type of data is the interplanetary magnetic data obtained from OMINI website (www.ominiweb.com). This data consists of 5 min data value of solar wind velocity and IMF components of Bz(nT), Bx(nT), By(nT), PD (Ncm^{-3}), Dst Index (nT) AE Index (nT) and solar wind pressure.

From the data, hourly averages of solar wind IMF parameters for each day of the month were calculated using excel package. Solar wind energy (ε) of the magnetosphere will be calculated using:

$$\varepsilon = V_{sv}B^2 sin^4\left(\frac{\theta}{2}\right)/l_o^2 \quad (1)$$

Where V_{sv} = solar wind velocity; $|B|$ = magnitude of the IMF parameter; $\theta = \arctan(B_y/B_z)\ for B_z > 0\ and\ \theta = 180^0 - \arctan(B_y/B_z)\ for B_z \leq 0$; l_o = dayside magnetopause scale length which is equal to $7R_E$; B_z = z-component of IMF parameter; B_y = y-component of IMF parameter. Also, the hourly averages of meteorological parameters for each day of the month were calculated using excel package. From the values obtained, partial pressure of water (e) was determined from the equation as follows:

$$e = e_s.\frac{H}{100} \quad (2)$$

Where H is the relative humidity, and e_s is the saturation vapour pressure determined by Clausius-Clapeyron equation given as:

$$e_s = 6.11exp\,[17.5(T - 273.16)/(T - 35.87)] \quad (3)$$

Employing the values of meteorological parameters (temperature, pressure and relative humidity) computed, radio refractivity was calculated using;

$$N = 77.6\frac{P}{T} + 3.37\ x\ 10^5\ e/T^2 \quad (4)$$

Where P = atmospheric pressure (hPa), e = water vapour pressure (hPa), T = absolute temperature (K).

Equation 4 may be employed for the propagation of radio frequencies up to 100 GHz (Willoughby et al., 2002).

The two results (solar wind coupling and radio refractivity) were compared to actually deduce solar-wind magnetosphere coupling effect on radio refractivity at Minna in the year 2008.

RESULTS AND DISCUSSION

The graphical representation of hourly records of variations of solar wind energy (ε), radio refractivity (N), proton density (PD) and Dst index are presented in the figures for both quiet and disturbed days during dry and rainy seasons at Minna, Nigeria. Although the research was carried out in all the months of the year, the quiet and disturbed days of the months of February and August, respectively were considered. In the same manner, the relationship of solar wind energy (ε), PD and Dst index with radio refractivity (N) are the main focus of this work. This relationship is clearly demonstrated in the plots of variations and correlations of radio refractivity with magnetospheric interplanetary parameters as can be observed in Figures 1 to 32, respectively.

Figures 1 to 8 represent variations of solar wind energy and radio refractivity with time for quiet and disturbed days during dry and rainy seasons at Minna in 2008. Figures 9 to 12 represent correlation of solar wind energy with radio refractivity for quiet and disturbed days during dry and rainy seasons.

In Figure 1, 2, 3 and 4, there is a corresponding fall and rise in the peaks of variations of solar wind energy as well as radio refractivity with time almost throughout the early hours of the day, but they seem to exhibit maximum increase between 0600 to 2200 h for both quiet and disturbed days during dry and rainy seasons. This is caused by diurnal variations of solar wind energy, in which case, the IMF turns anti-parallel to the earth's field on the day side of the magnetosphere. This period is the time when there is maximum solar wind activity (solar maximum) caused by the high temperature released by

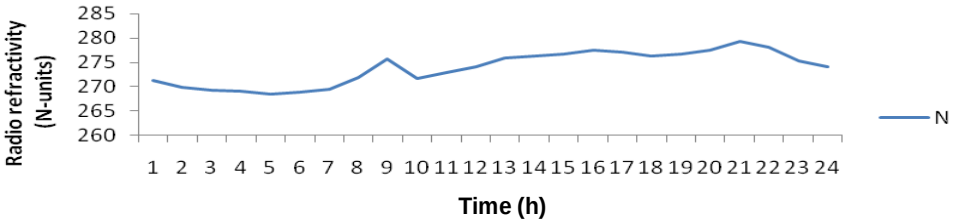

Figure 2. Variations of radio refractivity with time for quiet day during dry season**.**

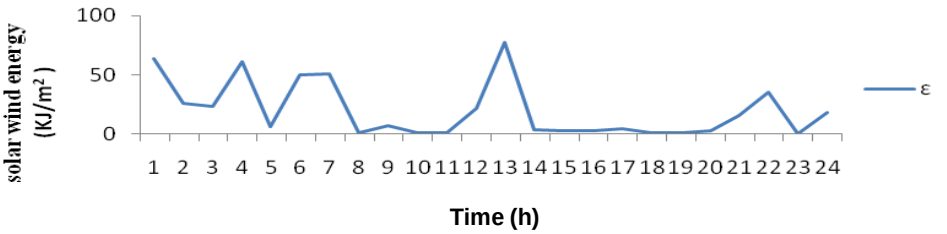

Figure 3. Variations of solar wind energy with time for disturbed day during dry season.

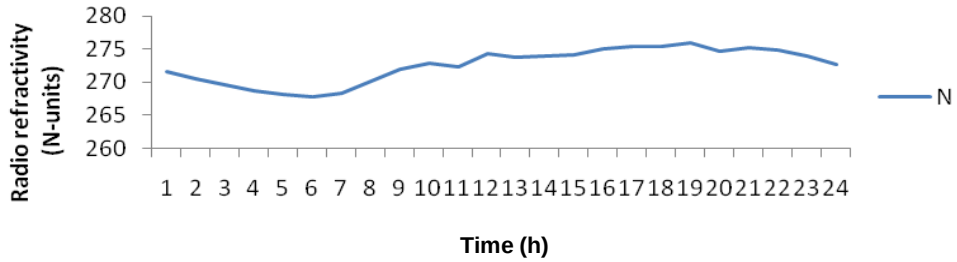

Figure 4. Variations of radio refractivity with time for disturbed day during dry season.

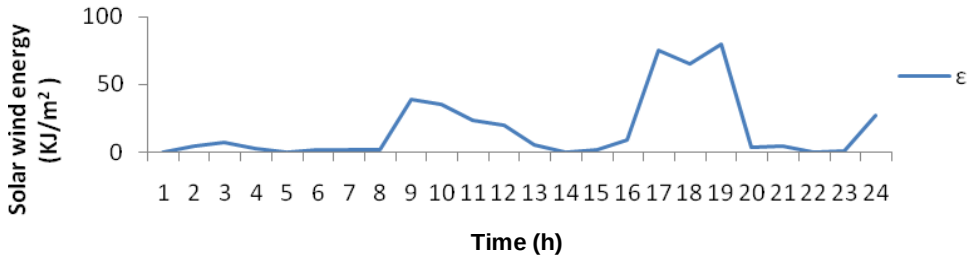

Figure 5. Variations of solar wind energy with time for quiet day during rainy season.

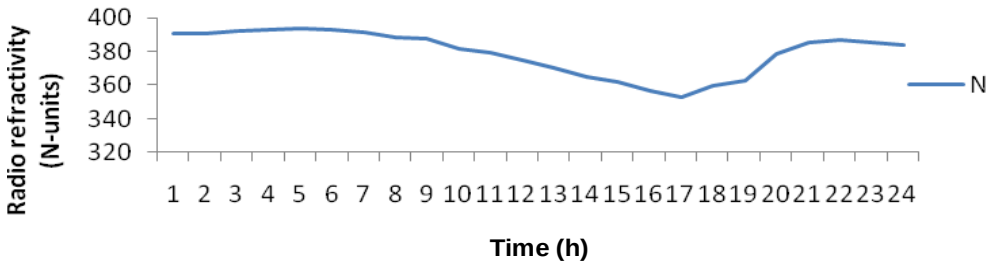

Figure 6. Variations of radio refractivity with time for quiet day during rainy season.

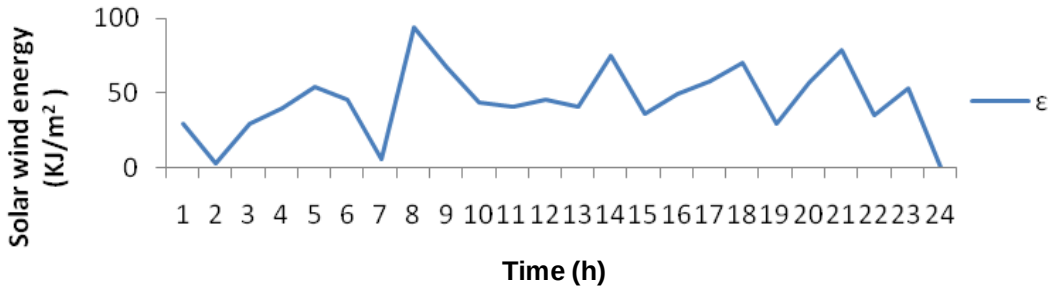

Figure 7. Variations of solar wind energy with time for disturbed day during rainy season.

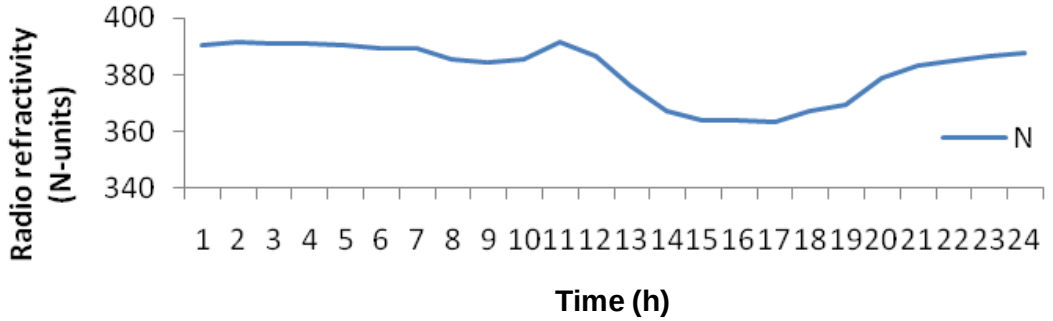

Figure 8. Variations of radio refractivity with time for disturbed day during rainy season.

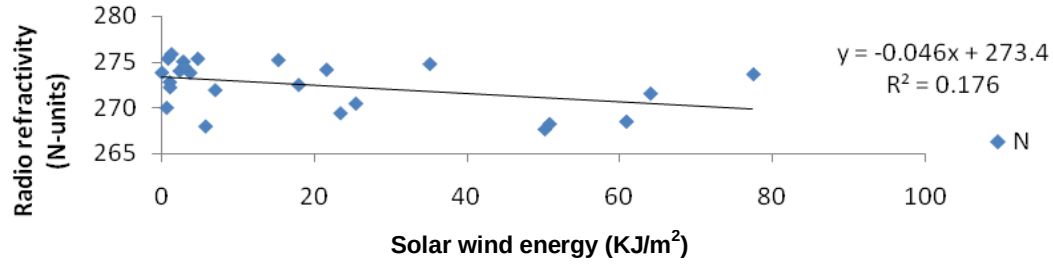

Figure 9. Correlation of solar wind energy with radio refractivity for quiet day during dry season.

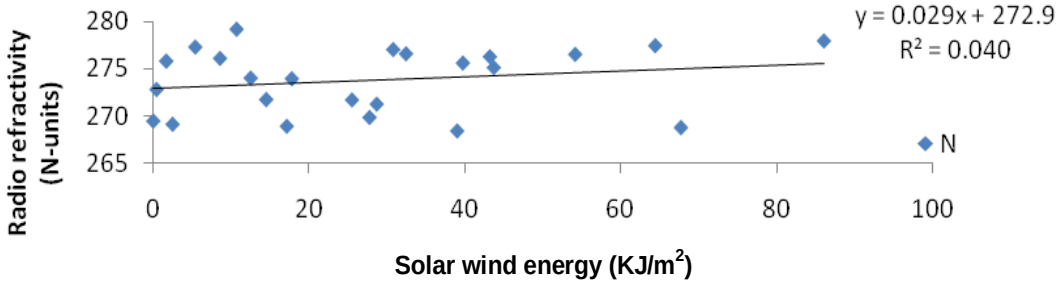

Figure 10. Correlation of solar wind energy with radio refractivity for disturbed day during dry season.

the sun during solar wind magnetosphere coupling activities. This process results in the ejection of high solar wind (stream of electrons and protons) which is the characteristics of southward continental drift observed

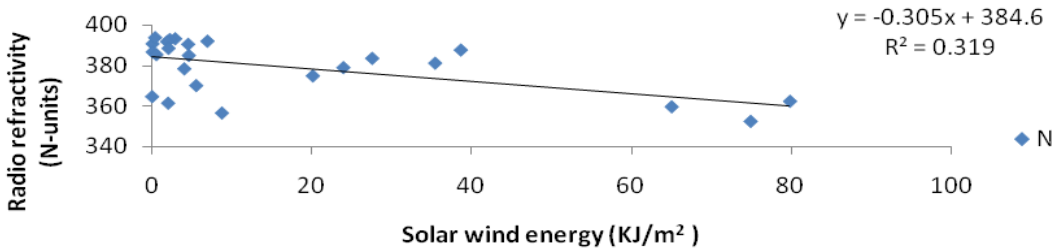

Figure 11. Correlation of solar wind energy with radio refractivity for quiet day during rainy season.

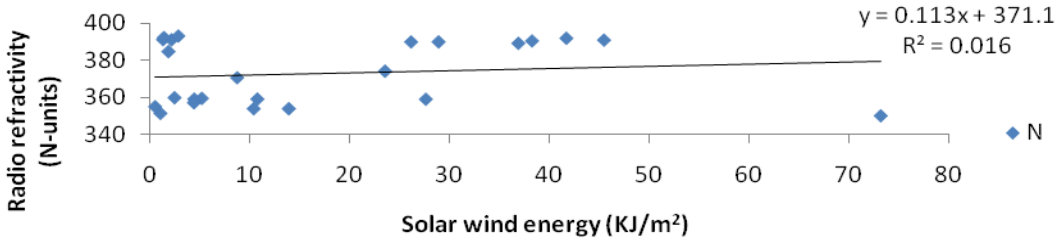

Figure 12. Correlation of solar wind energy with radio refractivity for disturbed day during rainy season.

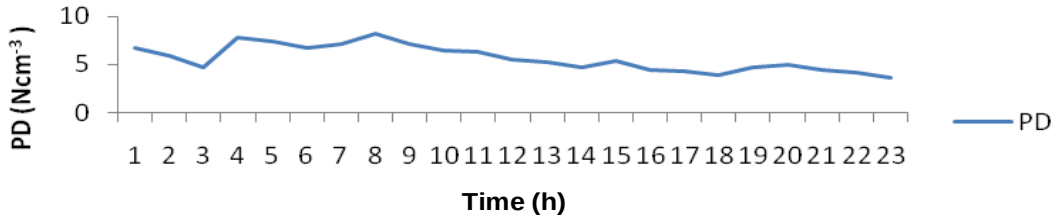

Figure 13. Variation of PD with time for quiet day during dry season.

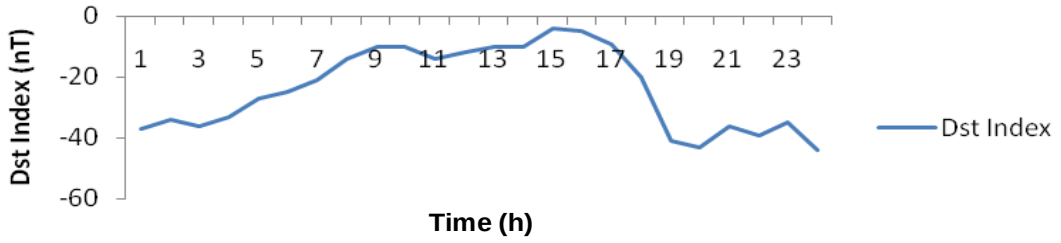

Figure 14. Variation of Dst index with time for quiet day during dry season.

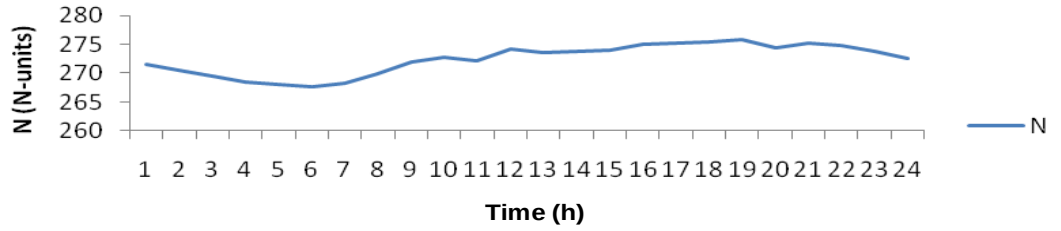

Figure 15. Variation of radio refractivity with time for quiet day during dry season.

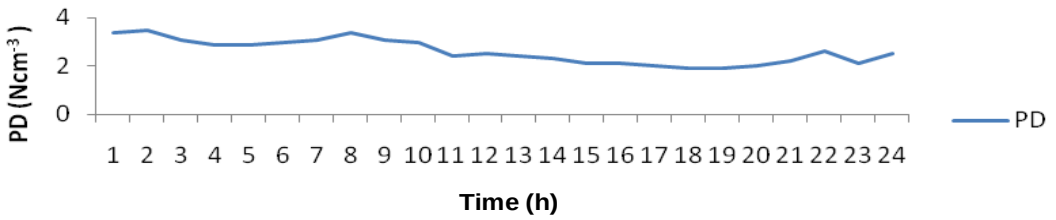

Figure 16. Variation of PD with time for disturbed day during dry season.

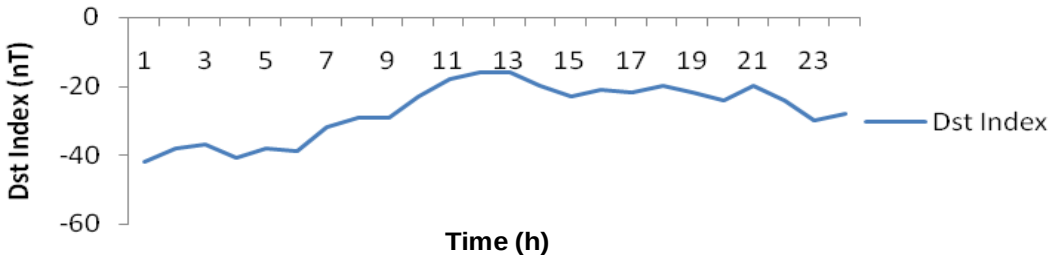

Figure 17. Variation of Dst index with time for disturbed day during dry season.

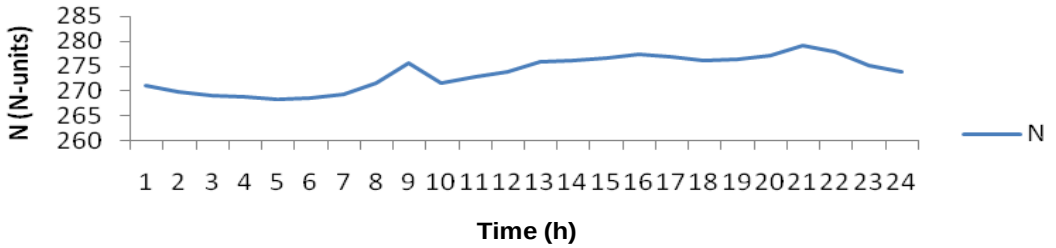

Figure 18. Variation of radio refractivity with time for disturbed day during dry season.

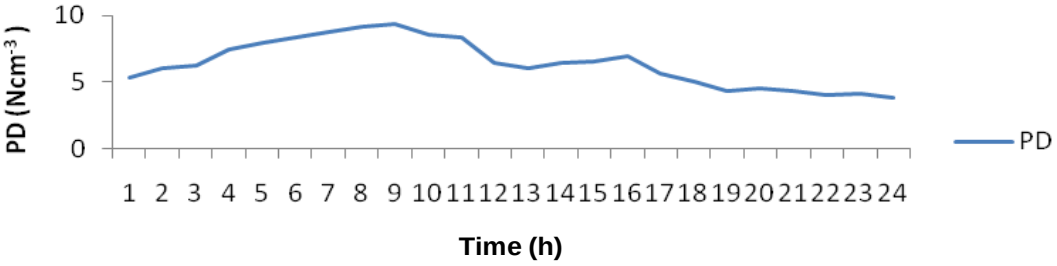

Figure 19. Variation of PD with time for quiet day during rainy season.

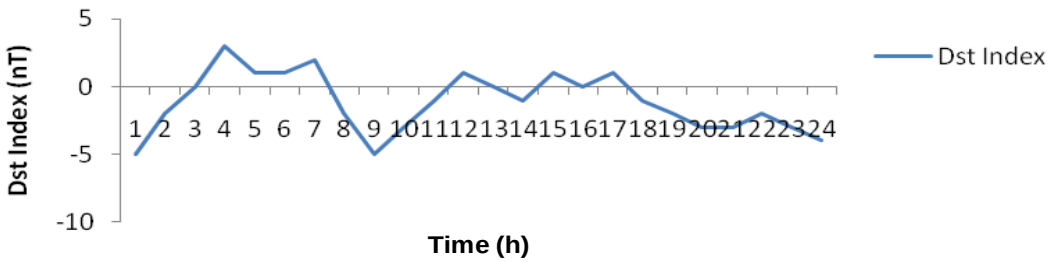

Figure 20. Variation of Dst index with time for quiet day during rainy season.

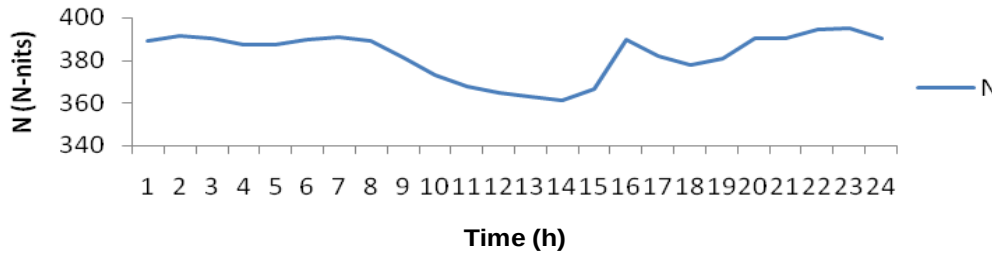

Figure 21. Variation of radio refractivity with time for quiet day during rainy season.

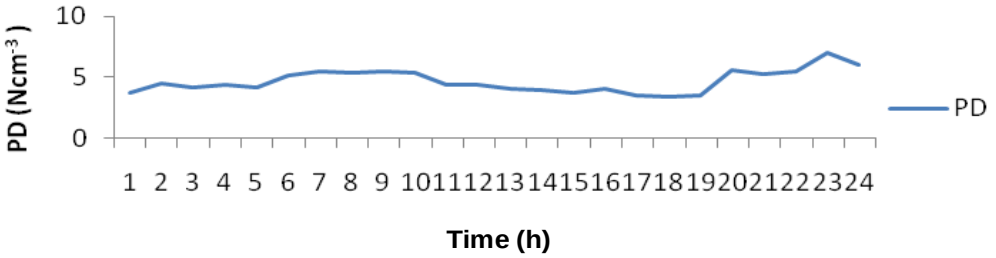

Figure 22. Variation of PD with time for disturbed day during rainy season.

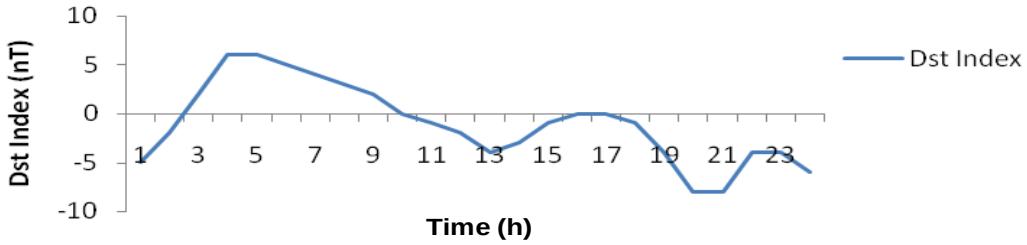

Figure 23. Variation of Dst index with time for disturbed day during rainy season.

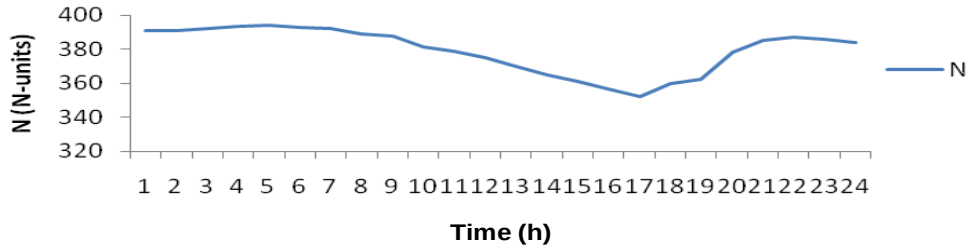

Figure 24. Variation of radio refractivity with time for disturbed day during rainy season.

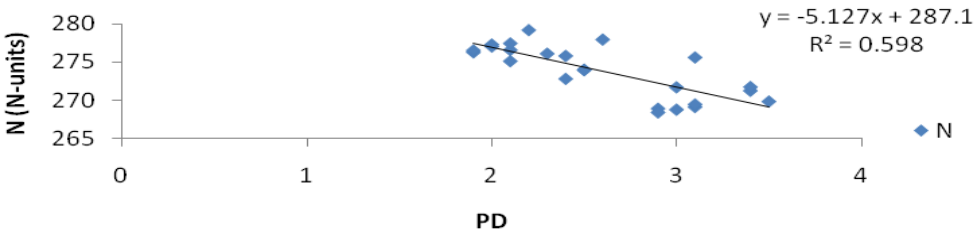

Figure 25. Correlation of PD with radio refractivity for quiet day during dry season.

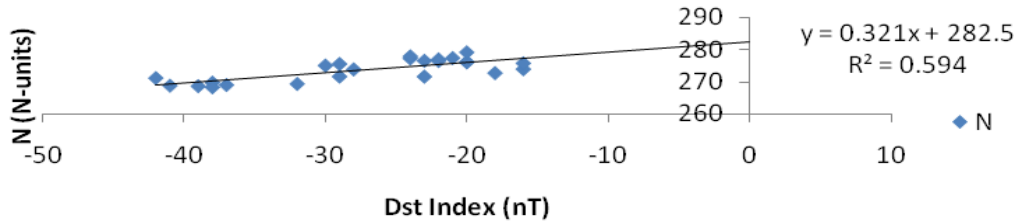

Figure 26. Correlation of Dst Index with radio refractivity for quiet day during dry season.

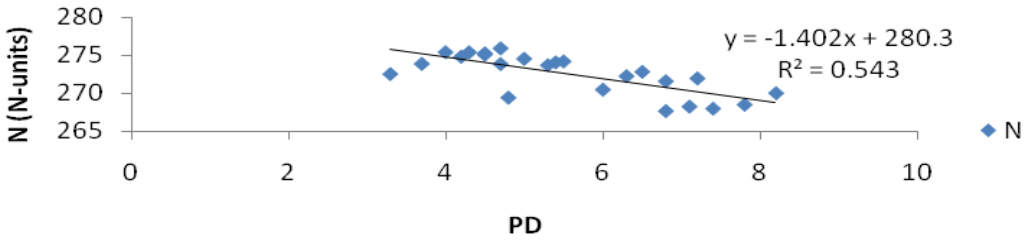

Figure 27. Correlation of PD with radio refractivity for disturbed day during dry season.

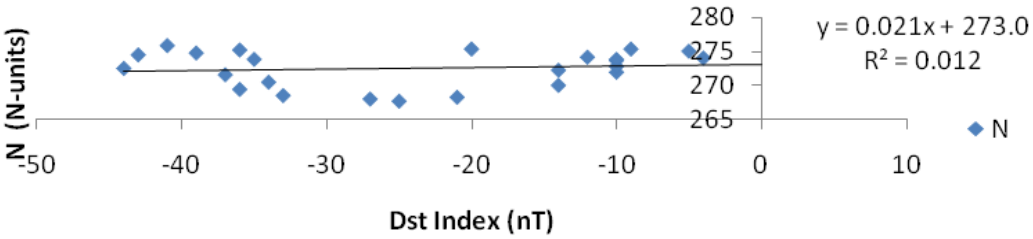

Figure 28. Correlation of Dst index with radio refractivity for disturbed day during dry season.

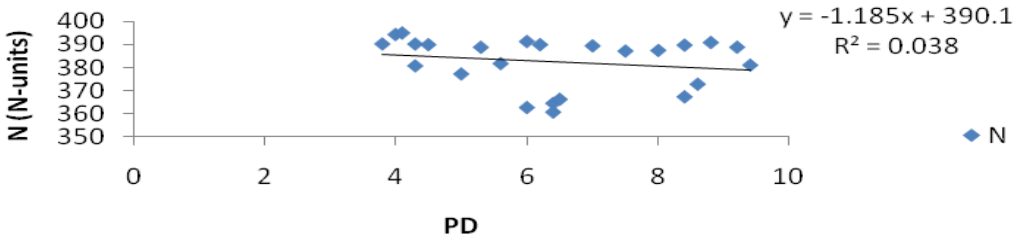

Figure 29. Correlation of PD with radio refractivity for quiet day during rainy season.

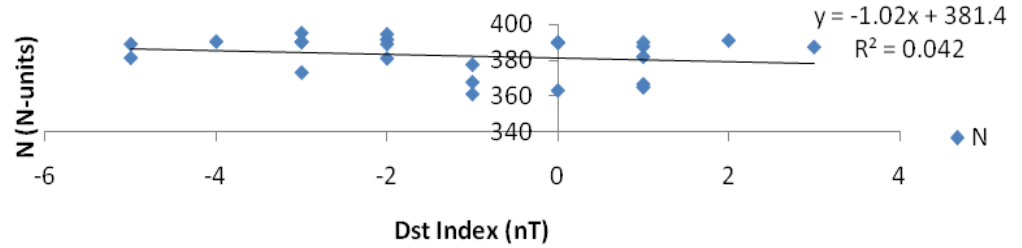

Figure 30. Correlation of PD with radio refractivity for quiet day during rainy season.

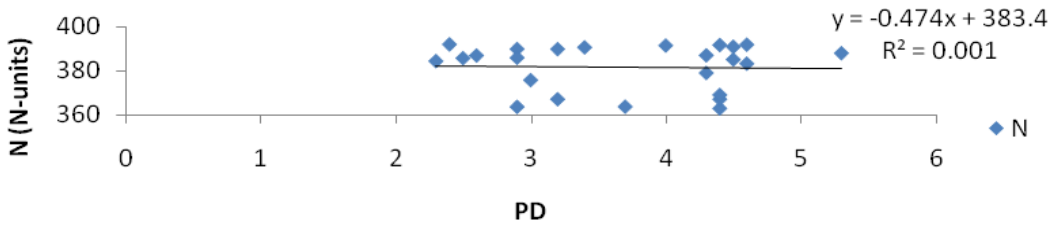

Figure 31. Correlation of PD with radio refractivity for disturbed day during rainy season.

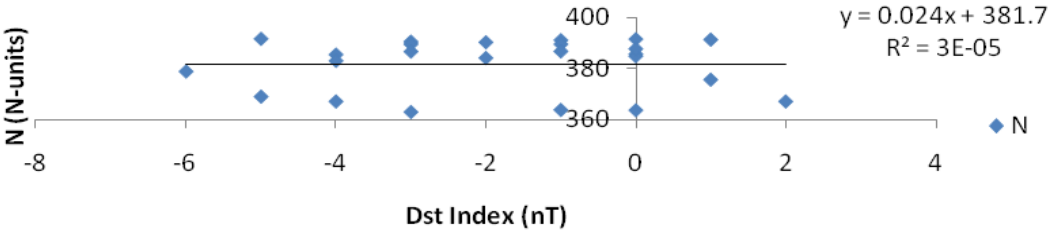

Figure 32. Correlation of Dst index with radio refractivity for disturbed day during rainy season.

during dry season having energies ranging from 10 to 100 kev. The maximum peaks observed in Figures 1 to 8 also signify the period known as “disturbed period”; which is the period when solar wind magnetic field and that of the earth magnetosphere reconnects resulting in the outflow of plasma aurora zones with a high energy into the magnetosphere. During the time of these events, the energy transported from solar wind into the magnetosphere creates geomagnetic variation and drives different types of pulsations such as changes in temperature, pressure, humidity in the atmosphere. Since radio refractivity is a function of temperature, it also changes as the solar wind changes during disturbed period.

As can be observed in Figures 5 to 8 during rainy season, there is a minimum decrease in solar wind activities (solar minimum) as indicated in the trend line of the figures, owing to the weather condition of the atmosphere during the period. This period which is noted by slow solar activity in the atmosphere is dominated by cool and moisture weather condition due to rainy season which leads to decrease in temperature during solar wind magnetosphere coupling within the period. This equally leads to decreased radio refractivity within the period as well for both quiet and disturbed days.

In Figures 9 to 12, the correlation analysis of solar wind energy with radio refractivity was done to estimate the extent at which radio refractivity depend on solar wind activities for both quiet and disturbed days during dry and rainy season. In Figures 9 and 10, the square of correlation coefficients of solar wind energy, with radio refractivity for quiet and disturbed days during dry season are, respectively 0.176 and, 0.0401. Also, in Figures 11 and 12, the square correlation coefficients of solar wind energy with radio refractivity for quiet and disturbed days during rainy season are 0.3198 and 0.0.16, respectively. These results clearly review that the there is weak correlation between solar wind energy and radio refractivity during solar wind-magnetosphere interactions with radio refractivity. This thus shows that solar wind is not the sole cause of fluctuations in radio refractivity, but the fluctuations should be attributed to other magnetospheric interplanetary parameters or local effects.

However, the slope of the trend lines shows that solar wind changes mostly with positive slope in rainy season within most of the times. This may be caused by advection processes, cooling of the earth’s surface through radiation and compression of air masses during this period of the year.

Figures 13 to 24 are the hourly variations of interplanetary parameters and radio refractivity with time for both quiet and disturbed days during dry and rainy season. From time variations in the amplitude of interplanetary parameters and radio refractivity periodicity plots, it is observed that almost all the interplanetary parameters follow the same sporadically change in amplitude of their movement as the radio refractivity for both quiet and disturbed days during dry and rainy seasons. But in some cases, while radio refractivity changes with time in positive direction, some of the interplanetary parameters change in negative direction for both quiet and disturbed days during dry and rainy season. These concurrent disparities on the nature of the trend line within different intervals in the movement of interplanetary parameters, as well as radio refractivity, show that certain significant fluctuations on interplanetary parameters are marked by the absence of similar

fluctuations on radio refractivity within that period.

The significant effect of the interplanetary parameters on radio refractivity has also been found when the square of the correlation coefficients values were considered. Figures 25 to 32 depict the correlations of interplanetary parameters with radio refractivity for both quiet and disturbed days during dry and rainy season for the year 2008. It is noticed from the figures that the square of the correlation coefficient is quite high for the cases of PD and Dst Index with their square of the correlation coefficients ($R^2 = 0.598$) and ($R^2 = 0.5949$) for quiet days during dry season (Figures 25 and 26). Similarly, for disturbed days during dry season, it was observed that only PD exhibits high correlation with square of the correlation coefficient ($R^2 = 0.543$). From these results, it can be clearly stated that the change in radio refractivity is sorely caused by the change in PD and Dst Index for both quiet and disturbed days during dry season. In contrast, during quiet and disturbed days for rainy season, it was observed that all the interplanetary parameters exhibit very weak correlation with radio refractivity (Figures 27 to 32). Therefore, the change in radio refractivity is not dependent on the change in interplanetary parameters for quiet and disturbed day during rainy season.

Conclusion

This work has clearly shown that radio refractivity has corresponding variations with solar wind energy as well as other magnetospheric interplanetary parameters with time. However, the trend lines of variation of solar wind energy with time, exhibit positive gradient within the period of the research. This may be caused by advection processes, cooling of the earth's surface through radiation and compression of air masses during this period of the year. However, from the result of the correlations, it was observed that solar wind energy exhibits weak correlation with radio refractivity, while magnetospheric parameters exhibit strong correlation with radio refractivity within all the periods of investigation. Having these facts in mind, one can say that, the random and systematic fluctuations, observed during radio wave propagation, emanating from the deviation of radio refractive index of the radio wave in the atmosphere, is due to the influence of magnetospheric parameters interaction with radio wave.

ACKNOWLEDGEMENT

We are grateful to the Centre for Basic Space Science (CBSS), University of Nigeria, Nsukka and OMINIWEB.com for the availability of the hourly means of the megnetospheric interplanetary parameters and parameters.

REFERENCES

Baker DN, Pulkkinen TI, Angelopoulos V, Baumjohann, W, McPherron RL (1996). Neutral line model of substorms: pastand present views, J. Geophys. Res. 101:12975-13010.

Dungey JW (1963). The structure of the exosphere or adventures in velocity space, in Geophysics; The Earth's Environment, Gordon and Breach, New York. pp. 505-550.

Fuselier SA, Klumpar DM, Shelley EG (1991). Ion reflection and transmission during reconnection at the Earth's subsolar magnetopause.

Fuselier SA, Shelley EG, Peterson WK, Lennartsson OW, Collin HL, Drake JF, Ghielmetti AG, Balsiger H, Burch JL, Johnstone A, Rosenbauer H, Steinberg JT (1997). Bifurcated cusp ion signatures: evidence for re-reconnection. Geophys. Res. Lett. 24:1471-4.

Okoro ON, Agbo GA, Ekpe JE, Obiekezie TN (2012). Solar Wind-Magnetosphere Coupling Effect on Radio Refractivity in 2008 for Minna. J. Nat. Sci. Res. 2:76.

Phan TD, Paschmann G, Baumjohann W, Sckopke N, Luhr H (1994). The Magnetosheath region adjacent to the dayside magnetopause: AMPTE/IRM observations. J. Geophys. Res. 99:121.

Rickett BJ (1990). Radio propagation through the turbulent interstellar plasma, Ann. Rev. Astron. Astrophys. 28:561-605.

Russell CT (2000). The solar wind interaction with the Earth's magnetosphere: A tutorial. IEEE Trans. Plasma Sci. 28:1818.

Russell CT, Gang L, Luhmann JG (1998). Lessons from the Ring Current Injection during the September 24-25, 1998 Storm. Geophys. Res. Lett. submitted 2000.

Tsurutani BT, Meng CI (1972). "Interplanetary magnetic field variations and substorm activity." J. Geophys. Res. 77:2964.

Willoughby AA, Aro TO, Owolabi IE (2002). Seasonal Variations of radio refractivity gradients in Nigeria. J. Atmos. Solar-Terrestrial Phys. 64:417-425.

UPCOMING CONFERENCES

ICNMB 2013 : International Conference on Nuclear Medicine and Biology Switzerland, Zurich, July 30-31, 2013

International Conference on Mathematical Modeling in Physical Sciences Prague, Czech Republic, September 1-5, 2013

Conferences and Advert

July 2013
ICNMB 2013 : International Conference on Nuclear Medicine and Biology
Switzerland, Zurich, July 30-31, 2013

September 2013
International Conference on Mathematical Modeling in Physical Sciences
Prague, Czech Republic, September 1-5, 2013

International Journal of Physical Sciences

Related Journals Published by Academic Journals

- *African Journal of Pure and Applied Chemistry*
- *Journal of Internet and Information Systems*
- *Journal of Geology and Mining Research*
- *Journal of Oceanography and Marine Science*
- *Journal of Environmental Chemistry and Ecotoxicology*
- *Journal of Petroleum Technology and Alternative Fuels*

academicJournals